# First-principles investigation of molecules' adsorption on complex surfaces of perovskites : the case of organic/inorganic perovskites for photovoltaic applications

Arpit Mishra

Arpit Mishra. First-principles investigation of molecules' adsorption on complex surfaces of perovskites : the case of organic/inorganic perovskites for photovoltaic applications. Physics [physics]. Université de Lorraine, 2021. English. NNT : 2021LORR0255 . tel-03667933

HAL Id: tel-03667933
https://hal.univ-lorraine.fr/tel-03667933

Submitted on 20 Oct 2022

École doctorale C2MP

# THÈSE

pour l'obtention du grade de
**Docteur de l'Université de Lorraine**
présentée par

**Arpit MISHRA**

---

# First-principles investigation of molecules' adsorption on complex surfaces of perovskites: the case of organic/inorganic perovskites for photovoltaic applications

---

Défendue le 28 octobre 2021 à Metz

**Composition du jury**

| | | |
|---|---|---|
| Hong XU | *Prof., Université de Lorraine* | Présidente |
| Benoit COASNE | *DR CNRS, LIPhy, Grenoble* | Rapporteur |
| Mikaël KEPENEKIAN | *CR CNRS (HDR), ISCR, Rennes* | Rapporteur |
| Noel JAKSE | *Prof., Université Grenoble Alpes* | Examinateur |
| Paulina PLOCHOCKA-MAUDE | *CR CNRS (HDR), LNCMI, Toulouse* | Examinateur |
| Roberta POLONI | *CR CNRS, Laboratoire SIMaP, Grenoble* | Examinateur |
| Andrei POSTNIKOV | *Prof., Université de Lorraine* | Directeur de thèse |
| Philippe BARANEK | *Dr., EDF R&D* | Encadrant |

Thèse préparée sous l'encadrement de Philippe BARANEK
(EDF R&D) au Laboratoire de Chimie et de Physique – Approche
Multi-échelles des Milieux Complexes (LCP–A2MC) et à
l'Institut du Photovoltaïque d'Île de France (IPVF)

*In loving memory of my mother,*
*Neelam Mishra*

# Contents

# List of Figures

# List of Tables

# Introduction

With the growing world population, our reliance on non-renewable energy sources increases. The consequences of growing dependence on non-renewable energies are resulting in excessive greenhouse gas (GHG) emissions [Fischer, 1999] leading to global warming and would eventually be resulting in climate change. To curb the GHG emission, we have to rely more on renewable sources of energy such as wind, solar, water for power generation.

Among renewable sources of energy, the importance of which is generally understood, solar energy singles out as being universally available. Among the ways to grasp this energy for practical use, photovoltaics (PV) stands out as the most widely used renewable energy source. Photovoltaics involves the photovoltaic effect, which is the generation of voltage and current in a semiconducting material exposed to sunlight. The effect has been known since 1839, being discovered by Edmond Becquerel. The first solar cell consisting of a layer of selenium, which dated back to 1884, achieved the efficiency of about 1% [Guarnieri, 2015]. The quest for a more efficient conversion of solar energy into electricity by affordable means brings new materials and device designs into the game.

In order to be considered as promising for practical applications in photovoltaics, the material must first of all be a semiconductor with a suitable bandgap (near the optimum of 1.4 eV) for the absorption of a maximum number of photons from the radiation of the sun [Zekry and Shaker, 2018], high absorption coefficient to have the optimum thickness of the material (200 and 500$\mu$m) [Mayerhöfer and Popp, 2019], the high collection efficiency of the photo-generated electron-hole pairs which requires a high lifetime of the mobile carriers in the material [Dittrich et al., 2016], high mobility of the charge carrier to reduce the Ohmic losses [Ebenhoch et al., 2015].

A typical PV process includes the following steps: when the sunlight falls on the material, electron-hole pairs are generated, which are further separated by a potential profile that is created in the cell by doping. Following the electric field which establishes across the p-n junction, the electrons move towards the n-doped end and the holes towards the p-doped end. In order to maximise the area of the junction in which the adsorption of a photon may happen, the junction is typically fabricated in the form of two superposed layers. The outcome of the effect is either the tension induced between layers or, should they be connected into a circuit, the photocurrent that flows.

From the commercial point of view, the material should fulfil such conditions as low cost, high efficiency and high durability (resistance to the outer atmosphere). The efficiency of a PV cell is given as the amount of electrical power coming out of the cell as compared to the energy from the sunlight shining on it. The average efficiency for commercialisation of solar panels is around 15–20% [NRE]. All three factors (cost, efficiency and durability) have to be fulfilled at the same time to bring the solar cell into commercial use.

Figure 1, issued and periodically updated by the National Renewable Energy Laboratory (NREL), shows the progress in the efficiency of different families of materials on a time scale. These materials are semiconductors; their properties can be altered, according to specific needs, e.g. by chemical doping.

For a long time, in the twentieth century, the most promising class among the materials for PV was represented by inorganic crystalline semiconductors, such as silicon or gallium arsenide. However, a problem with these materials is that their use for PV demands the crystal structure to be almost perfect, that generally comes at a high cost. Several efforts have been made to optimise polycrystalline semiconductor materials such as cadmium telluride (CdTe), copper indium gallium selenide (CIGS) which can be deposited on the substrate to form a thin film large area devices. In the late 1970s and early 1980s, apart from silicon technology, thin-film technology also started to gain popularity.

From the Figure 1, one can notice that in the early 2000s, various types of organic cells started showing promising results. Further on, in the early 2010s, “perovskites” came into the picture. Organic halide perovskites from the perovskite family emerge as promising materials for PV applications. Some of their optoelectronic properties are specified below:

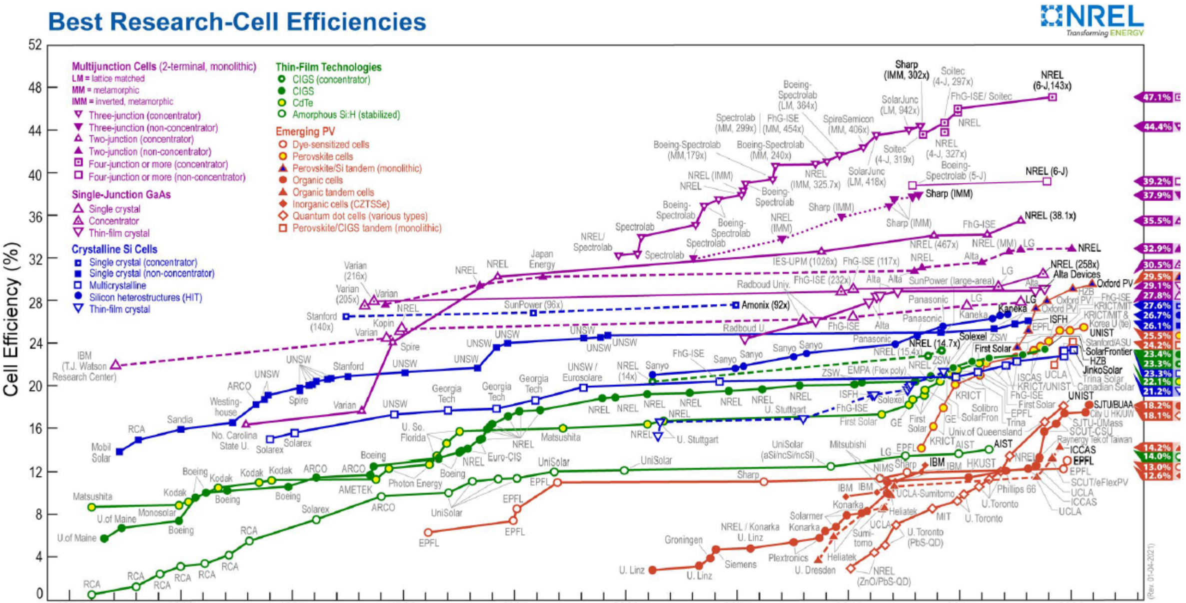

FIGURE 1: Conversion efficiencies for cells of different materials and different technologies used in PV domain, from 1976 to present. Figure adapted from [NRE].

- optimum band-gap of around 1.7 eV [Tanaka et al., 2003].
- good sunlight absorption (from 300–850 nm) [Du et al., 2016].
- appropriate carrier transport properties due to shallow level defects [Du, 2014].
- defect tolerance [Brandt et al., 2015].
- long carrier lifetime (up to 100nm optical absorption depth) [Stranks et al., 2013].

From the commercial perspective, these organic/inorganic halide perovskites can be manufactured at low cost via solution-based methods with simple processing, not demanding any expensive types of equipment and can be easily up-scaled for commercialisation. It is peculiar that, as can be seen in Figure 1, the efficiency of organic halide perovskites were around 2.5% in 2009 [Kojima et al., 2009] and by 2020, it rose to 25.2%. Also, they are seen as a promising candidate for tandem (details of tandem solar cells can be found in Corkish [2004]) applications. In recent years, monolithic perovskite/silicon tandem solar cells have reached a certified efficiency of 29.1% [Liu et al., 2020]. This tremendous increase in efficiency seemed encouraging and promising for further research.

Despite the great advantages of perovskites, they have a major drawback: their insufficient long-term stability. When exposed to light illumination [Li et al., 2017], air [Leijtens et al., 2017], moisture [Yang et al., 2015a], perovskite solar cells considerably degrade in their power conversion efficiency. This stability issue is the major roadblock in commercialising perovskite solar cells. In attempts to better understand the issue of degradation, a number of experimental [Han et al., 2015; Christians et al., 2015] and theoretical works has been done [Jong et al., 2018; Juarez-Perez et al., 2016; Li et al., 2021, 2020]. Yet, inorganic halide perovskite ($CsPbX_3$, X=I, Br, Cl), the emerging materials for PV applications, lack systematic theoretical research in understanding the degradation of their properties under anticipated practical conditions of use. Theoretical simulations of the effect of water and air on the degradation of PV properties of $CsPbX_3$ type perovskites have very few studies till date [Li et al., 2021].

In the case of organic halide perovskite, widely popular methylammonium lead halide (MAPI), the effect of water and air on the bulk has been studied by Caddeo et al. [2017] and Leguy et al. [2015]. These organic halide perovskites lack the theoretical studies of surfaces and the effects of air and water on their surfaces.

In this work, the studies of surface properties of organic and inorganic halide perovskites are carried out with the help of theoretical simulations are done within the framework of the DFT (Density functional theory).

The manuscript is organised as follows. After the brief outline of perovskites, Chapter 1 focuses on their structure and their stability issues. Chapter 2 introduces various theoretical approaches and approximations used in this work. In Chapter 3, the bulk properties and surface properties highlight the issues of phase transitions. Chapter 4 focuses on the adsorption of molecules such as CO, $CO_2$, $O_2$ and $H_2O$ on the perfect surfaces of $CsPbX_3$ (X=I, Br, Cl) and surfaces characterised by the presence of point defects, typically vacancies. The role of adsorption on electronic properties is investigated. The final Chapter 5 deals with the adsorption of $H_2O$ and $O_2$ on the surfaces of MAPI. The adsorption of molecules in the dissociated state on perovskite surfaces and their impact on the electronic structure are also covered in this chapter. The general conclusion summarises the work.

# Chapter 1

# Organic/Inorganic halide perovskites for photovoltaic applications

Halide perovskite-type materials have the generic formula $ABX_3$, where X stands for halogen anion such as $Cl^-$, $Br^-$, $I^-$. Moreover, (A, B) cations would satisfy the valence matching the anions. For halide perovskites, A can be a monovalent organic ammonium (MA) or formamidinium (FA) cation such as $MA^+ = CH_3NH_3{}^+$, $FA^+ = CH(NH_2)_2{}^+$ or it can be inorganic metal cation such as $Cs^+$, $Rb^+$. The average ionic radius of A cation must be around 1.65 to 2.50 Å [Akhtar et al., 2018]. B atom is a divalent metal cation such as $Pb^{2+}$, $Sn^{2+}$. B ion is octahedrally coordinated by X anions forming the basic $PbX_6$ octahedral perovskite units. The organic/inorganic cation (A) lies within the centre of the cage made of joined $BX_6$ units. The organic cation is free to rotate within the cage depending on the temperature [Carignano et al., 2016].

A prototype perovskite-type structure belongs to a cubic space group $Pm\bar{3}m$. However, it often undergoes distortions from cubic into lower-symmetry phases. To understand when the perovskite will be in cubic-/tetragonal-/orthorhombic-/hexagonal-phase, the notion of Goldschmidt tolerance factor ($t$) might be useful [Goldschmidt, 1926]. The latter is expressed as:

$$t = \frac{(r_A + r_X)}{\sqrt{2}(r_B + r_X)} \tag{1.1}$$

where $r_A, r_B$ and $r_X$ are the radii of atoms A, B and X respectively. At $t = 1$, the sizes of ions are perfectly matched to be assembled into the ideal cubic structure. The tolerance factor hints for which one of the two competing instabilities, B off-center displacement

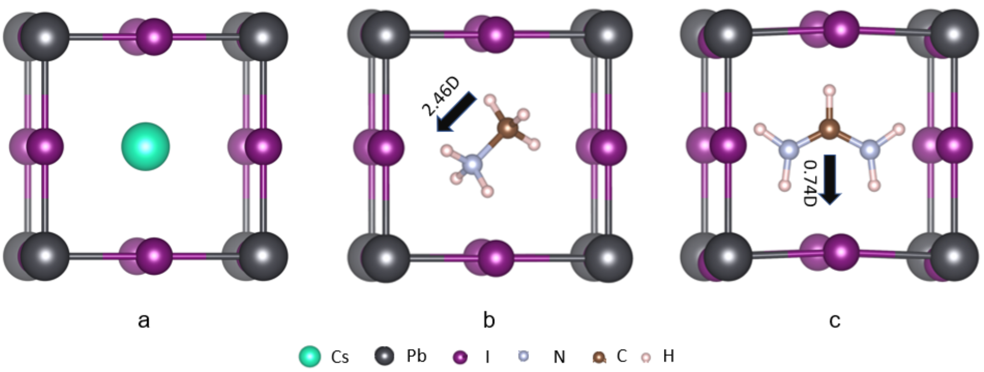

FIGURE 1.1: View at an angle to [100] of cubic phase of $APbX_3$ perovskites with Cs (a), MA (b) and FA (c) cations shown with their nearest (I) and next nearest (Pb) neighbors. The arrow indicates the direction of dipole moment of MA and FA cations.

or $BX_6$ coupled octahedra tilting, will eventually take over. When $t > 1$ then B-off center displacement is more probable. For the halide perovskite, the tolerance factor ranges from 0.7 to 0.9 [Goldschmidt, 1926] this implies that an antiferrodistortive-type instability, namely a tilting of octahedra, will be more probable, with a tendency to go into the orthorhombic structure.

In Figure 1.1, a fragment of the $APbI_3$ perovskite structure is shown around the A cation, which is Cs (a), MA (b) and FA (c), with its nearest (I) and next-nearest (Pb) neighbours.

As already mentioned above, the perovskites are notorious for phase transitions. Types of such transitions which usually come into discussion are *displacive* or *order-disorder*. The *displacive* type of phase transition, common in halide perovskites, can be described as simultaneous (symmetry-lowering) displacement of atoms in the unit cell, which typically reveals the eigenvector of a particular soft mode of vibration. The identification of such soft modes, corresponding to particular phonons at the centre of the Brillouin zone ($\Gamma$; $\mathbf{q}$=0) or other value of the wave vector $\mathbf{q}$, helps to anticipate or predict such phase transitions in a calculation. Such analysis of soft modes for halide perovskites is discussed in Chapter 3. The different phases and phase transition temperatures for halide perovskite focused in this work are discussed below:

- For $CsPbI_3$, the sequence of crystallographic phases starts from the high temperature cubic phase ($Pm\bar{3}m$, stable above 533 K) → the orthorhombic ($Pnma$) →

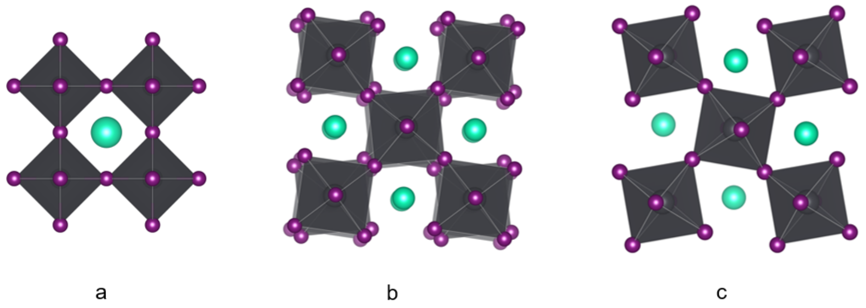

FIGURE 1.2: Different phases of $CsPbI_3$ perovskite a) cubic phase ($Pm\bar{3}m$); b)tetragonal phase ($P4/mbm$); c) orthorhombic phase ($Pnma$).

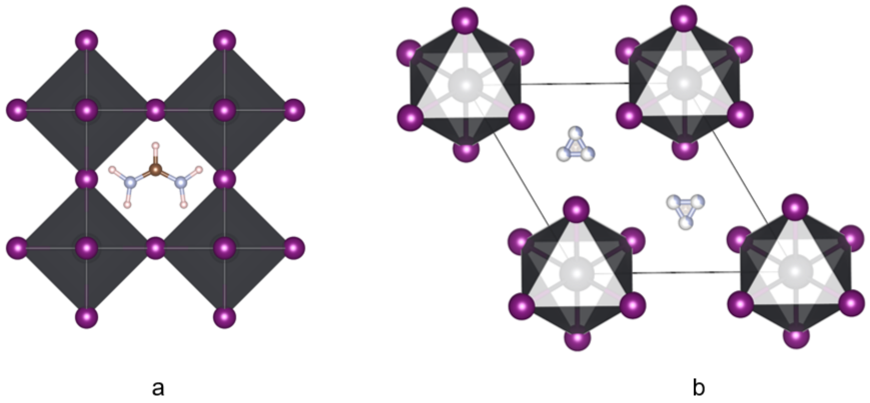

FIGURE 1.3: Different phases of FAPI in a) cubic phase ($Pm\bar{3}m$); b) hexagonal phase ($P6_3mc$)

the disordered orthorhombic ($Amm2$) ones [Eperon et al., 2015; Stoumpos et al., 2013a] as the temperature decreases. The resulting transformation is shown in Figure 1.2 from a → c. For $CsPbCl_3$ and $CsPbBr_3$, the sequence starts also from the high-temperature cubic perovskite structure ($Pm\bar{3}m$, stable above 320 K and 403 K, for X = Cl and Br respectively) → the tetragonal ($P4/mbm$) → the orthorhombic ($Pnma$) ones [Stoumpos et al., 2013b] as the temperature decreases.

- Similarly, MAPI exists in cubic phase ($Pm\bar{3}m$) at high temperatures ($> 327.4$ K), whereas on lowering the temperature to $160 - 330$ K, it transforms into body centered tetragonal phase ($I4/mcm$) and upon further cooling ($< 160$ K), into orthorhombic phase ($P4/mbm$) [Whitfield et al., 2016].
- FAPI exists at high temperatures (above 440 K) in cubic phase ($Pm\bar{3}m$) and, on going down to the room temperature, transforms into hexagonal phase ($P6_3mc$)

below 438 K [Ma et al., 2017]. The corresponding transformation is shown in Figure 1.3.

## 1.1 Architecture of perovskite solar cells

A typical architecture of a perovskite solar cell would involve a transparent conducting oxide electrode (TCO); a fluorine-doped tin oxide (FTO) is usually used as such; a hole transport layer (HTL) which ought to be p-type doped, usually Spiro-OMeTAD, alias 2, 2′, 7, 7′ - tetrakis (N, N-di-p-methoxyphenylamine) 9, 9′ - spirobifluorine for the extraction of holes; an electron transport layer (ETL) which ought to be n-doped, usually $TiO_2$, for extraction of electrons; metal contacts which are electrodes (usually made of gold), and perovskite itself (see Figure 1.4). The perovskite can be doped to be of p-type or n-type. Further, TCO is deposited over the glass substrate. The device configuration can play a crucial role in the solar cell's performance. Perovskite solar cells, in general, can have two types of configuration: p-i-n (inverted) or n-i-p (regular), depending on which charge transport layer (hole/electron) is in the outer part of the cell, exposed to the incident light. The two configurations can have a mesoporous layer that can be either HTL or ETL (see Figure 1.4, left panel).

Like other materials, organic/inorganic perovskites corrode upon exposure to atmosphere. One of the major concerns limiting the use of perovskites for PV applications is their insufficient long-term stability see – e.g., Han et al. [2015]; Christians

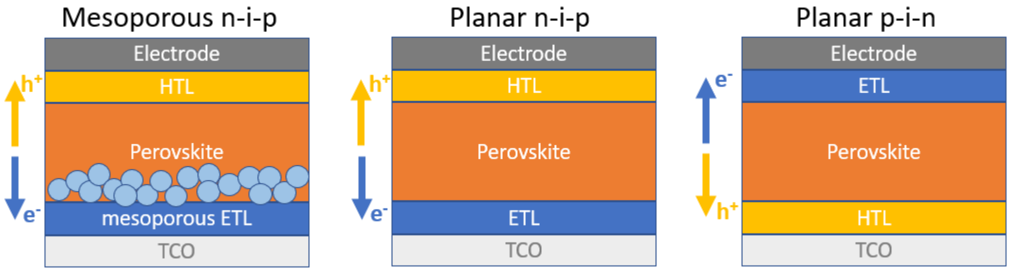

FIGURE 1.4: Schematic figure of different possible configurations of perovskite solar cell. The left panel depicts mesoporous n-i-p configuration, in which a mesoporus ETL is used; the circles indicate a part of the mesoporous ETL layer within the perovskite layer. See text for details.

et al. [2015]; Leijtens et al. [2013]. Perovskites tend to degrade in their performance when exposed to air and moisture. Not only perovskites as such but also the solar cell devices on their base give rise to problems concerning stability. Various HTL or ETL used can sometimes deteriorate the performance of the perovskite solar cells.

## 1.2 Stability of perovskite solar cells

Some of the issues related to structure stability, thermal stability, stability in the presence of light, air and moisture within perovskite material and the device are discussed below.

### 1.2.1 Structural stability

As was discussed before, perovskites exhibit different crystalline phases, out of which the cubic one is that the best suited for PV applications. However, this phase is not stable at all the operating temperatures and ambient conditions. It can quickly transform into tetragonal/orthorhombic/hexagonal, depending on the type of perovskite, when exposed to ambient conditions or low temperature. It is a challenging task to maintain the cubic phase at different operating temperatures and ambient conditions. Various techniques are discussed in the coming paragraphs dealing with methods to maintain structural stability.

Different processing techniques are adopted to crystallise MAPI in the cubic phase, such as the vacuum deposition technique [Palazon et al.]. As discussed before, the size of the cation can influence the phase stability; the MA ion in MAPI is not of an ideal size to fit into the cubic structure; as a result, the latter tends to transform into lower- symmetry phases. Yang et al. [2015c] mixed MA and FA cations and, moreover, iodine with bromine ions to bring the average tolerance factor close to 1. This mixture allows an easy formation of black cubic phase at low temperature (less than 315 °C) [Sutton et al., 2016].

In attempts to bring about a more stable perovskite solar cell, inorganic halide perovskite was tested against structural stability. These inorganic perovskites ($CsPbX_3$) also transform to low-symmetry phases at different ranges of operating temperatures.

Several works done in the last years bring the prospects of stabilising the cubic phase at room temperature within grasp. Protesescu et al. [2015] obtained monodisperse colloidal nanocubes (with edges 4–15 nm) of $CsPbX_3$ (X=Cl, Br, I), of which only $CsPbI_3$ transformed to the low-temperature yellow phase after long storage (months), whereas the two others stayed cubic. Swarnkar et al. [2016] fabricated films of cubic-structure quantum dots of $CsPbI_3$ (with edges $\sim$10 nm), stable during months in contact with air. Lai et al. [2017] induced a transformation from the yellow phase (orthorhombic phase) to the black cubic phase, following a rapid thermal quenching in $CsPbI_3$ nanowires of $\sim 10^2$ nm thickness. These results seem promising, yet further work needs to be done to improve the efficiency and device stability. The larger FA ion was mixed with the smaller Cs ion to tune the tolerance factor close to 1. Moreover, to obtain structures with better stability and efficiency Anaraki et al. [2016] have made various compounds with success by substituting A site cation with MA, FA, Cs, Rb and by mixing halides (I/Br).

Mixed cations and mixed halide ion approaches seem promising in improving the structure stability. However, this remains beyond the scope of the present work.

### 1.2.2 Stability in the presence of oxygen

**Effect of oxygen on halide perovskite**

The major problem the solar cells face is the oxidation of functional components in the presence of air. Despite proper packaging, oxygen can penetrate the solar cell, hence intrinsic stability to oxygen is important. In the presence of light, the degradation of perovskite by oxygen is accelerated (see Figure 1.5) as compared to the inert (nitrogen) atmosphere. It was reported earlier that in the presence of light and oxygen, the devices made based on $MAPbI_3$ degrade by 20% in a few hours [Pearson et al., 2016]. Aristidou et al. [2017] showed that reaction of oxygen with $MAPbI_3$ in the dark is not so pronounced and goes via superoxide pathway. $O_2^-$ reacts with photo oxidised $MAPbI_3$ as illustrated in the reaction below:

$$4\,CH_3NH_3PbI_3{}^* + O_2{}^- \longrightarrow 4\,PbI_2 + 2\,I_2 + 2\,H_2O + 4\,CH_3NH_2. \qquad (1.2)$$

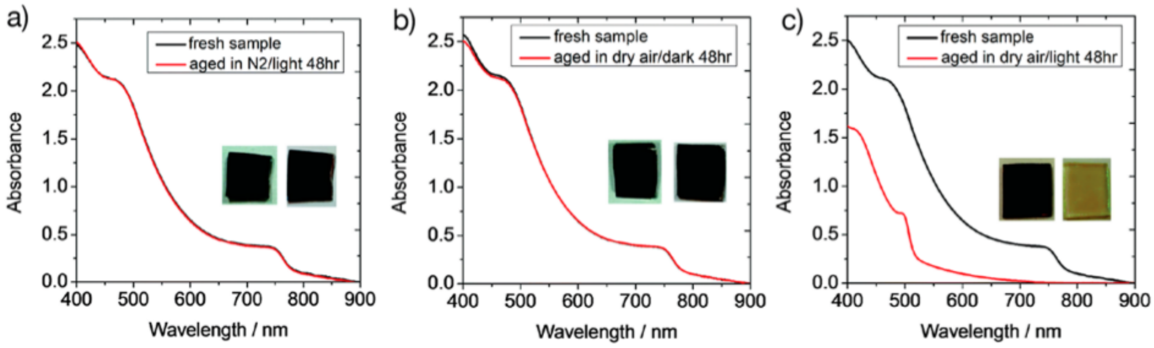

FIGURE 1.5: The absorbance of MAPI thin films at different wavelengths and under different oxidation conditions. (a) film when exposed to light under inert conditions; (b) film when exposed to air in the dark; (c) film exposed to both light and air. Figure taken from Bryant et al. [2016].

The critical step in the above reaction is the formation of $O_2^-$. Aristidou *et al.* suggested that the superoxide generation is linked with degradation and is often facilitated in the presence of iodide vacancies. The oxygen is first adsorbed at the vacancy sites; further on this molecular oxygen traps electrons from the conduction band of the perovskite and forms reactive superoxide. This superoxide starts an acid-base reaction, with A cation acting as an acidic entity, which results in the formation of water and lead iodide, as shown in the chemical equation (1.2). Bryant et al. [2016] suggested the use of interlayers to extract electrons from the perovskite layer to minimise the reaction of oxygen with the electrons and thus reducing the formation of superoxide species.

Meggiolaro et al. [2017] reported the passivation of the perovskite layer in the presence of oxygen. Oxygen goes into the deep traps resulting from iodide interstitials and forms partially stable oxides, such as hypoiodite, iodite and iodate.

$$I^- + \tfrac{1}{2}O_2 \longrightarrow IO^- \quad \text{(hypoiodite);} \tag{1.3}$$

$$I^- + O_2 \longrightarrow IO_2^- \quad \text{(iodite);} \tag{1.4}$$

$$I^- + \tfrac{3}{2}O_2 \longrightarrow IO_3^- \quad \text{(iodate).} \tag{1.5}$$

The interstitial iodine is an easier target for oxidation than the iodine in the lattice, the latter effectively inactivates the deep traps present in the bandgap of $MAPbI_3$, thus providing some stability to the perovskite. However, the long-term exposure to oxygen may result in oxidative damage which starts at the surface and eventually undermines the stability.

**Effect of oxygen on device as a whole**

The efficiency of the cell depends on the stability of all the materials in the cell. In the presence of air, there is a possibility of oxidation of charge transport layers, the ETLs and HTLs discussed earlier in this chapter. These charge transport layers can consist of a polymer, organic molecules, or inorganic materials, such as oxides. Organic molecules and polymers may be vulnerable to oxidation. The defects arising from the oxidation result in a decrease in the quantum efficiency of the cell [Abate et al., 2013]. Typically, degradation of these organic charge transport layers does not affect the recombination and generation of carriers but affects their mobility.

Sometimes the oxidation of materials for the charge transport layer, such as PTAA, alias poly(triarylamine), or Spiro-OMeTAD can be used to generate free holes in the HOMO (highest occupied molecular orbital) for reducing the series resistance by increasing the p-type conductivity [Cappel et al., 2012; Heo et al., 2013].

The most commonly used oxide transport layers such as $SnO_2$ or $TiO_2$ are known to have drawbacks of reacting with atmospheric oxygen in the presence of UV light. $TiO_2$ is well known to be used as a catalyst in the splitting of water and as a photocatalyst for decomposition of other organic materials [Ni et al., 2007; Matthews, 1986]. Oxygen can get into the vacancies of $TiO_2$, forming superoxide, which can then readily react with the perovskite. The issue of superoxide is discussed in the previous section.

To improve the stability of $TiO_2$ (ETL layer), CsBr is used to modify the layers of $TiO_2$, and this overall improves the stability of the perovskite cell [Li et al., 2016a]. The use of UV filters or thin layers of fullerenes over $TiO_2$ led to an improvement of the stability of $TiO_2$ [Bush et al., 2017].

### 1.2.3 Stability under moisture

**Effect of moisture on halide perovskite**

Humidity and the effect of oxygen are the most extensive environmental factors which affect the stability of the solar cells. Perovskites get corroded and oxidised in the presence of moisture and air, even if they are well encapsulated [Uddin et al., 2019; Kim et al., 2019]. In another work, the non-encapsulated cells were exposed to air and moisture for a few hundred hours with a relative humidity of more than 50% [Yang et al., 2015a]. In MAPI, the water penetrates the lattice. The nature of MA is acidic; it reacts with water by giving away a proton after that $CH_3NH_2$ is evolved and leaves behind the lead halide octahedra, thus degrading the perovskite structure. The crystal structure of the hydrated phase shows some hydrogen bonding with lead halide octahedra and the formation of cation-water-cation chains demonstrating solid interactions between water and the cation [Vincent et al., 1987]. Recently two mechanisms were proposed for the degradation of MAPI: one suggested the formation of transient $PbI_{2+x}^{x-}$ [Huang et al., 2016]:

$$4\,\mathrm{CH_3NH_3PbI_3(s)} + 8\mathrm{H_2O} \longrightarrow \mathrm{(CH_3NH_3)_4PbI_6 \cdot 2\,H_2O} \longrightarrow \mathrm{PbI_2} + \mathrm{complexes}\,, \tag{1.6}$$

whereas the other mechanism involved the decomposition of the MA molecule in presence of water [Huang et al., 2016]:

$$\mathrm{CH_3NH_3PbI_3(s)} \xrightarrow{\mathrm{H_2O}} \mathrm{CH_3NH_3I\ (aq)} + \mathrm{PbI_2(s)}\,. \tag{1.7}$$

In $MAPbI_3$, this process occurs under moisture and temperature (80 °C) when exposed for a longer time. Various efforts were made to slow down the degradation. The group of Seok [Noh et al., 2013] introduced Br in the lattice of $MAPbI_3$, whereby Br occupies the place of I. Introducing Br results in the shrinking of the lattice parameter, which strengthens the hydrogen bonding between the MA molecule and lead iodide octahedra, confining water to intercalate with MA and to form a hydrated phase. This tuning of constituents can affect the reaction of water with MAPI. Further on, Jiang et al. [2015] substituted some part of I with thiocyanate ion. The optoelectronic properties remain the same as for MAPI but with improved stability against moisture.

The compositional tuning for the cation also influenced the moisture resistance. $FAPbI_3$ also does not show better stability in the presence of moisture. The black cubic phase is accelerated to transform to the yellow hexagonal phase. A similar phase stability issue is important for $CsPbI_3$, where the black cubic phase is transformed to yellow orthorhombic phase in the presence of moisture. $FAPbI_3$ and $CsPbI_3$ show better thermal resistance but poor structure stability in the presence of moisture. So to improve the structure stability [Li et al., 2016b] mixed FA and Cs on the A site such that FA was 85% and Cs was 15% and it was observed that in 15% relative humidity, the performance was improved by 20% as compared to $FAPbI_3$. It was shown by the Snaith's group that $FA_{0.83}Cs_{0.17}Pb(I_{0.6}Br_{0.4})_3$ is stable for 650 h under ambient conditions and solar illumination, whereas $MAPbI_3$-based solar cells downgraded already before 100 h [Wang et al., 2017]. This can be understood in the following way. For the water to intercalate and form a hydrated phase, strong hydrogen bonding should occur between the water molecule and the organic cation. So, the positive charge on the organic cation has to become more delocalised, making the cation less acidic. Moreover, adding smaller-size Cs also reduces the reactivity of the overall A cation, thereby enhancing the stability against moisture.

In order to protect the perovskite surface from moisture, various passivation layers, e.g., of $Al_2O_3$ [Koushik et al., 2017], oleic acid [Abdelmageed et al., 2018], or alkylalkoxylilane can be deposited on top of the perovskite surface, as suggested by Zhang et al. [2015]. 2D perovskites [Lan et al., 2019] were also used to passivate and encapsulate 3D perovskites for better results [Grancini et al., 2017].

#### Effect of moisture on the device as a whole

The contact layers such as Spiro-OMeTAD, PTAA are hygroscopic and can initiate the degradation because of moisture and presence of heat [Habisreutinger et al., 2014]. The use of a transport layer such as random copolymer (RCP), which is hydrophobic in nature, can delay the degradation caused by moisture [Kim et al., 2016]. Also, one method is the use of graded layers of spiro-OMeTAD with P3HT layer [Kim et al., 2017].

The PV modules may have glass-glass packaging, preventing moisture from entering the cell. Various new technologies are evolved for flexible packaging with better resistance and low-cost [Yu et al., 2016].

## 1.3 Defects within halide perovskite solar cell

The defects, unavoidable at the manufacturing stage, can hinder the cell's performance. Some of these defects are particularly prone to form in particular materials. These can be intrinsic (defects due to atoms within the host material) or extrinsic (defects due to atoms outside the host material) in nature. In the following, we briefly discuss how the point defects may contribute to the degradation of solar cells. Among the halide perovskites, MAPI is known to be rich in point defects. Typical ones are the vacancy of MA ion, lead ion or the iodine ion; moreover these ions can be at the interstitial sites [Kim et al., 2014; Yin et al., 2014]. The interstitial defects with high formation energy usually contribute to deep levels, and those with lower formation energy contribute to shallow levels. The point defects with low formation energy should not contribute to high densities of non-radiative recombination centres which lie deep within the bandgap. Defects at shallow levels can result in unintentional doping at room temperature. This intrinsic doping can change the perovskite from $p$-type to $n$-type. The formation of Schottky defects, that is, vacancies, may occur in comparable concentrations on both cation and anion sublattices, which means that the defects may well be present even in samples obtained under stoichiometric growth conditions [Walsh et al., 2015]. Schottky defects can restrict the unintentional doping, as each vacancy type contributes to an opposite charge carrier which can compensate one another naturally.

The widely researched topic in the halide perovskites solar cells is the current–voltage hysteresis which could be observed while characterising the devices [Snaith et al., 2014]. This hysteresis, i.e., the difference in the forward and reverse current curves measured while scanning the voltage, poses a specific challenge in accurately estimating the power efficiency of solar cells.

Beyond ferroelectricity, which is a "usual suspect" for this kind of behaviour in perovskites but stays mainly beyond the scope of the present work, the defects mobility seems to be the second possible major reason for the current – voltage hysteresis [Ball and Petrozza, 2016]. The halide ions are mobile, generating the potential gradient within the device. Yang et al. [2015b] reported that the most mobile species were the point defects, mainly halide ions hopping over interstitial positions. Further, using a theoretical approach, it was suggested that the activation energy (for transport) of iodine interstitial and a vacancy are similar and lower than that of the other point defects [Azpiroz et al., 2015].

We mentioned only briefly and only few of the challenges arising in attempts to make perovskite materials practically usable in photovoltaics. Some obstacles are purely technical, with good prospects of being eventually overcome, whereas others demand certain ingenuity. Still, the perspectives of practical use, because of efficiency and low cost, make the ongoing research look rewarding.

To study the effect of water, a single water molecule will be adsorbed on the surfaces of perovskites. To study the effect of atmospheric gases, the molecules most commonly present in the air, such as CO, $CO_2$, $O_2$, will be tentatively adsorbed on the surfaces of inorganic halide perovskite. For organic halide perovskites, only the interaction with the oxygen molecule will be studied. The role of temperature and light will remain beyond the scope of our work.

Since perovskites are prone to develop defects, the role of vacancies in the above-mentioned processes of adsorption of gas molecules will be specifically studied. Other defects, such as grain boundaries or impurities, will not be addressed in this work.

# Chapter 2

# Theory foundations of the present work

## 2.1 Introduction

In this chapter, theory concepts (from the Born– Oppenheimer approximation through the hybrid functionals within the DFT) and calculation methods (notably the CRYSTAL17 code) applied in the present work are briefly discussed.

The theory plays a remarkable role in the study of materials since this branch of science exists. The theory allows to organise the knowledge and to make predictions based on the previous knowledge. The aspects related to elastic properties, heat transfer, interaction with light have long been – and still are – treated within empirical schemes; however, they are profoundly driven by processes played at the microscopic level – interactions between atoms, or excitations within (interacting) atoms. These processes fall into the range of applicability of quantum mechanics. The recognition of the fact that the interactions in question are of quite general character – basically they come down to electrostatic Coulomb interaction between charged particles (electrons and nuclei), taking also into account the Pauli exclusion principle – feeds an ambition that the understanding of various properties of different materials can be achieved *from first principles*, i.e., on the basis of universal quantum-mechanical laws, selecting just the chemical species of atoms which enter into interaction. However, the attempts of practical solution along the quantum mechanical path, operating in terms of Hamiltonians and wave functions, comes to its limits already at very compact systems. In fact, exact analytical quantum-mechanical solution was only found, to my knowledge, for two-particle systems, and numerical solutions, in many cases very accurate and promising, rely on approximations or model assumptions.

Grasping the behaviour of many-electron systems within quantum mechanics had a glorious history throughout the XX century. The schemes underlying an importance of many-electron wave function were interpenetrating the approaches coming from statistical side, aimed at description of ensembles of identical particles. A broad landscape and a certain hierarchy of practical schemes and approaches has been established (and still is under permanent development), aimed at different properties of systems of different sizes at different levels of accuracy. The part of this landscape which is "home" for the problematics and results of the present work is identified as the density functional theory (DFT). The "niche" of the DFT is treatment of systems (isolated molecules and/or periodic pieces of condensed matter) consisting of *many* (not just few but, say, $\sim\ 10^2 - 10^3$) atoms, at the level of accuracy (in relation to, say, energy) which is referred to as *chemical accuracy*. The latter means that reliable results are expected for, say, chemical reactions or structural phase transitions. In the rest of this chapter, the ideas and some practical aspects of the DFT will be outlined, in the utterly compact form, giving some references to extensive bibliography existing, from the very general foundations up to the technical details of performing practical calculations.

## 2.2 Born–Oppenheimer approximation and movement of nuclei

As a first step before entering the DFT as such, one can mention the Born-Oppenheimer (BO) approximation which justifies the separation of movements of electrons and nuclei [Born and Oppenheimer, 1927]. A priori, within the scope of quantum mechanics, all these particles are "actors" entering the definition of their common wave function. The BO approximation, arguing that the difference in masses between electrons and protons is important, justifies the separation of the common wave function into nuclei-only and electrons-only parts. In practical sense, this means that "from the point of view of electrons", the nuclei are too slow, and their effect can be taken into account adiabatically. In fact, this permits to solve just the problem of (interacting) electrons in the fixed Coulomb field of nuclei. In the subsequent sections, this electric field due to nuclei will often be included as the imposed external field, $V_{\mathrm{ion}}$ (the latter may, in principle, also incorporate the additionally imposed macroscopic electric field, e.g., in a polar material). As concerns the other part of the separation, "from the point of view of nuclei", the electrons are so fast that tracing the interaction with every single one among them makes no sense; they affect the nuclei rather by their averaged Coulomb field due to the charge distribution within the electron cloud. In practical sense (even if this is not essential in the BO approximation), this allows to abandon the quantum-mechanical description of nuclei and consider them as classical charged particles subject to electric fields (due to themselves and to the electron distribution). For a given spatial placement of nuclei, once the quantum-mechanical problem is solved for the electron system, the electric fields and hence forces acting on every nucleus can be calculated. The nuclei can then be shifted along these forces, arranging themselves in a modified spatial distribution. Such process can be repeated in consecutive alternating electronic (quantum-mechanical) and nuclear (classical) steps. Depending on how the whole algorithm is arranged, it can either aim at minimising the total energy (then we'll speak of structure relaxation), or, provided the nuclei have some initial resource of kinetic energy, let the process go on "forever", staging in this way an *ab initio molceular dynamics* simulation, the essential result of it is not the ultimate "frozen" solution, but the "history" and "trajectories" of the molecular dynamics run.

It is important to emphasize that the BO approximation is not universally valid, because in many situations, in particular those involving the movement of light atoms, the quantum nature of the movement of nuclei and their interaction with electrons is essential for the problems under study and cannot be simply discarded. Examples are not only light molecules and, e.g., photochemical processes in them [Capitani et al., 1982], but, for instance, "heavy" solids in which the energy profiles corresponding to some particular lattice distortions are particularly flat, and the classical description of corresponding effective "oscillators" becomes unsatisfactory [Bussmann-Holder et al., 2000]. In the scope of the present work, such situations do not come about, so that the BO approximation is valid and used throughout.

## 2.3 Frozen Phonons

Since the movement of ions will not be much discussed in the following sections related mostly to the solution of the electron problem, here can be an appropriate place to explain how the lattice vibrations are, in the simplest way, accounted for in *ab initio* calculations. Since the movement of nuclei is treated classically, and for every given spatial configuration of the nuclei the forces acting on them can be calculated, this permits to evaluate the classical force constants, which are by definition the derivatives of forces (acting on a given atom) in terms of displacements (of a given atom, in a given sense). Depending on the realisation in a calculation code, such derivatives may be available either directly (analytically, within the code), or calculated numerically by finite displacement technique. Either way, the matrix of force constants (numbered by atoms and Cartesian directions) can be accumulated and then diagonalized, yielding phonon frequencies and eigenvectors. Here, we skip the details of such scheme, namely, the construction of phonons corresponding to different values of the wavevector, the issues of convergence in the course of Fourier transformations, etc., and just outline the idea. The main role of phonons in the calculations described in the present work will be to identify the unstable modes (i.e. those for which the calculated frequency squared is negative) as guidelines for symmetry lowering and structure phase transitions.

## 2.4 Electronic part; precursors of DFT

A vast literature exists which offers quite accessible reviews of the history and the basics of DFT, ranging from Kohn [1999] to Becke [2014], Jones [2015] and Janesko [2021]. As important precursors, one traditionally identifies the Hartree–Fock (HF) theory which evolved along the line of specifying the "optimal" many-electron wave function [Hartree, 1928; Fock, 1930] and the Thomas–Fermi (TF) [Thomas, 1927; Fermi, 1927] theory which concentrates of electron density as an important variable, not bothering about the definition of the wave functions. In the interest of better understanding some issues important for the present work (e.g., the construction and use of hybrid functionals), it make sense to briefly explain what the HF theory is.

The starting point in a solution of any many-electron problem is the Schrödinger equation

$$H\Psi = E\Psi \quad . \tag{2.1}$$

with Hamiltonian for a system of $N$ electrons

$$\hat{H} = -\frac{\hbar^2}{2m}\sum_{i=1}^{N}\nabla_i^2 + \sum_{i=1}^{N} V_{ion}(\mathbf{r}_i) + \frac{1}{2}\sum_{ij(i\neq j)}^{N,N}\frac{e^2}{|\mathbf{r}_i - \mathbf{r}_j|} \quad , \tag{2.2}$$

where $V_{ion}$ is the Coulomb potential described as the interaction of nucleus $I$ with charge $Z_I e$ at position $\mathbf{R}_I$ with the electron at $\mathbf{r}_i$, given as:

$$V_{ion}(\mathbf{r}_i) = -\sum_I \frac{Z_I e^2}{|\mathbf{R}_I - \mathbf{r}_i|} \quad . \tag{2.3}$$

This expression is exact. The wave function, whatever the final expression for it, must satisfy the condition of being antisymmetric with respect to permutation of any two electrons. This can be enforced by postulating a special form of the wave function, that of (just one) Slater determinant [Slater, 1929] composed of one-electron functions to express the product of anti-symmetric wave functions in the form of determinant. This represents a (severe) limitation on the possible shape of the multi-electron wave function; yet this is a clearly defined limitation, which may serve an unambiguous reference point and beyond which the improvements can be systematically applied. This limitation being accepted, the focus of the method is placed onto the search of one-electron functions the Slater determinant of whose would provide the best expression for the wave function. The criterion of what is the "best" is the variational principle, in the spirit of which the expectation value of the Hamiltonian ($\langle\Psi|\hat{H}|\Psi\rangle$) calculated with wavefunctions $\langle\Psi|\Psi\rangle$ is minimised in terms of individual wavefunction ($\psi$) from which the Slater determinant is constructed. Individual variation of each wavefunction ($\psi_i \rightarrow \psi_i + \delta\psi_i$) leads to a system of HF equations:

$$\begin{aligned}\Big[\frac{1}{2}\,\bigtriangledown^2 + V_{ion}(\mathbf{r})\Big]\psi_i(\mathbf{r}) + \underbrace{\sum_j \int d\mathbf{r}'[\psi_j^*(\mathbf{r}')\psi_j(\mathbf{r}')]\frac{1}{|\mathbf{r}-\mathbf{r}'|}\psi_i(\mathbf{r})}_{V_H} \\ \underbrace{-\sum_j \int d\mathbf{r}'[\psi_j^*(\mathbf{r}')\psi_i(\mathbf{r}')]\frac{1}{|\mathbf{r}-\mathbf{r}'|}\psi_j(\mathbf{r})}_{V_X} = \epsilon_i\psi_i \quad ,\end{aligned} \tag{2.4}$$

$V_H$ and $V_X$ are the Hartree potential, and exchange potential respectively.

This is a system of coupled non-local integro-differential equations, the practical resolution of which would typically require resorting to numerical schemes and iterative self-consistent solution. By its shape, each equation resembles the Schrödinger equation on $\hat{H}$, however with a Hamiltonian which includes "specific" terms. One of these terms $V_H$ has a meaning of the electrostatic potential due to all the electrons available (including that for whose wave function the equation in question is formulated, that is, including the self-interaction of each electron with itself). The other "specific" term corrects this (nonphysical) self-interaction and takes into account the Pauli exclusion principle. This term is called *exchange* and is at the core of the HF approximation. One speaks of "exchange potential" $V_\mathrm{X}$ (the corresponding term in the Hamiltonian) or "exchange energy" $E_\mathrm{X}$ (the result of integration with the wave function). The index "X" is traditionally used as a reference to eXchange.

The *non-locality* of HF equations is related to the exchange term, which can be understood as an integral operator acting on a function under search. This creates certain technical difficulties in the practical solution of HF equations. Attempts to overcome these difficulties via certain approximations were on one line of development which lead to what later emerged as DFT. The other line of development run along the recognition of (electron) *density* of a basic variable, at least for a description of ground-state properties, which is much more "easy" than the multi-argument many-body wavefunction, and yet carries important information about the physical system. However, before concentrating on ground-state properties, we discuss electronic excitations and how they enter the context of the HF theory.

Studying excitations gives a clue to understanding the interactions of light with matter, therefore they must be important in our analysis of photovoltaic materials and processes in them. A priori an excitation means a transition of many-electron system between two states, one of which is usually the ground state and the other is one of possible excited states. Within the paradigm of the HF method, the states differ in how the corresponding one-electron states entering the Slater Hamiltonian are occupied by electrons. If the dynamical aspect of an excitation is not important for us, we can refer just to a difference between the two well-defined static states. The excitation energy, then, will be the difference between the total energies of system in these states.

The HF equations include energy parameters which emerge as Lagrange multipliers in the course of deriving the equations; however, by their place in the resulting equations, they resemble the energies in a Schrödinger equation. They are therefore usually referred to as one-electron energies, or HF eigenvalues. The Koopmans' theorem [Koopmans, 1934] establishes their physical meaning and relation with total energy differences. The prerequisite for a validity of the Koopmans' theorem is that the one-electron functions corresponding to the states under discussion (i.e., occupied and empty ones, at two sides of a transition) are the same, or, otherwise said, undergo no relaxation as the electron is transferred between them. This assumed, the difference of two one-electron states between which the electron is transferred emerges as an estimate of the corresponding excitation energy. It is understandable that such difference would usually come about *overestimated* (as compared to experiments, or with more accurate calculations) for the simple reason that the relaxation (modification) of the electronic system following an excitation would lower the system's total energy. Retrospectively, the experience of HF calculations shows that the estimations of excitation energies done on the basis of comparing the corresponding *total energies* is usually able to provide reasonable results (without going into details here) [Groß, 2009]. However, a systematic tendency of difference in *one-electron energies* to *overestimate* the energy of excitation between the corresponding states, which can be characterized as "unjustified expectations" from the Koopmans' theorem, is usually recognized as a shortcoming of calculation. With respect to situation in solids, where the optical excitation connects the states at the top of the valence band and at the bottom of the conduction band, and the corresponding calculation reveals the corresponding energy difference wrongly, the situation is typically casted as "gap problem". We just remark here that the HF calculations, judging by the predicted energy positions of corresponding one-electron states, tend to *overestimate* the band gap values.

Subsequent efforts, due e.g. to Slater [1929], aimed at "taming" the non-locality in the HF exchange term, which posed certain problems in practical calculations. This tendency merged with the other line of theory development for multi-electron systems, which originated from the works by Thomas [1927] and Fermi [1927] and emphasized the role and usefulness of the averaged *density* $\rho(\mathbf{r})$, rather than the wavefunction $\Psi$(r) in all its complexity. The expression for $\rho$ via $\Psi$ near the position $\mathbf{r}$ in space is the following:

$$\rho(\mathbf{r}) = N \int |\Psi(\mathbf{r}, \mathbf{r}_2, \mathbf{r}_3, ..., \mathbf{r}_N)|^2 d\mathbf{r}_2 d\mathbf{r}_3 ... d\mathbf{r}_N \quad . \tag{2.5}$$

The interest in density-related techniques considerably gained field as Hohenberg and Kohn [1964] demonstrated that the total energy *in a ground state* of a multi-electron system is fully determined by, i.e., is a *functional* of, just density, a simple function of **r**, whatever the complexity of its underlying multi-electron wave function would be. In spite of certain limitation (applicability to ground states, which limitation was subsequently weakened so as to encompass many practically interesting cases; the unknown form of this functional, etc.), the general paradigm of what thus became the density functional theory (DFT) fascinated many researches and led to remarkable practical results. It turned out that within this paradigm one can (at least hope to) overcome certain limitations inherent to the HF theory because of a priori single-determinant character of the wave function used within this theory. One says that the HF theory neglects *correlations*, that is, the tendency of electrons to avoid each other due to Coulomb repulsion between them as point charges, beyond whatever is already taken into account by the interaction of each electron with the whole electron density *and* mutual avoiding of electrons with the same spin, both these factors being already accounted for within the HF theory.

Kohn and Sham [1965] gave to the DFT its most recognizable "incarnation": on the way to apply variational principle to the total energy being functional of density, they expressed this density $\rho(\mathbf{r})$ as a sum over auxiliary functions $\varphi_i(\mathbf{r})$ so that

$$\rho(\mathbf{r}) = \sum_i |\varphi_i(\mathbf{r})|^2. \tag{2.6}$$

Formally not being anyhow related to one-electron wave functions (in eq. 2.4), these functions, called Kohn–Sham (KS) orbitals, behave very much like physically / chemically "meaningful" orbitals in molecules or solids; they satisfy a system of equations (Kohn–Sham equations)

$$\left[-\frac{\hbar^2}{2m}\nabla^2 + V_{eff}(\mathbf{r})\right]\varphi_i(\mathbf{r}) = \epsilon_i\varphi_i(\mathbf{r}) \quad , \tag{2.7}$$

$$V_{eff}(\mathbf{r}) = V(\mathbf{r}) + \int \frac{\rho(\mathbf{r}')}{|\mathbf{r}-\mathbf{r}'|}d\mathbf{r}' + V_{XC}(\mathbf{r}) \quad , \tag{2.8}$$

where $V(\mathbf{r})$ is the interaction with external potential, including electron-nuclei interaction, and $V_{XC}(\mathbf{r})$ is the exchange-correlation potential.

Eq. (2.7) resembles the HF system (see Eq. 2.4) or, more in general, the Schrödinger equation, and this without loss of generality. These KS orbitals are occupied according to the accedence of their corresponding energies $\epsilon_i$, and the $N$ orbitals with the lowest energies contribute to the definition of density according to Eq. 2.6. The generality of the KS scheme and all its potential power is then confined in the definition of *exchange-correlation potential* $V_{\mathrm{XC}}$, which can be considered as a counterpart of the exchange potential in the HF method, and which is defined as the functional derivative of the *exchange-correlation energy* over density.

Now, for practically implementing the solution of KS equations, one needs to explicitly specify an expression for $E_{\mathrm{XC}}[\rho(\mathbf{r})]$. This gave rise to a hierarchy of approximations and *ad hoc* schemes, which come about from time to time, typically suggested on the basis of combining some known and expected limiting cases (asymptotics, sum rules, etc.) with numerical results obtained with methods of superior accuracy, or simply adjusting to some experimental properties available for a large enough body of representative systems. Some schemes get broad recognition for their good predictive power, physical transparency, or practical simplicity, whereas others get lost in oblivion. For a minimal historical introduction, we should at least name the local density approximation (LDA), in which the density of exchange-correlation energy $\epsilon(\mathbf{r})$ at some point **r** depends only on the value of density in this very point, i.e.,

$$E_{\mathrm{XC}}^{(\mathrm{LDA})} = \int d\mathbf{r} \epsilon_{\mathrm{XC}}(\rho(\mathbf{r}))\,, \tag{2.9}$$

and generalized gradient approximation (GGA), in which the gradient of density along with the density itself, taken at spatial point **r**, give a closed expression for the density of XC energy.

Besides the total energy (from which the forces can be derived and used to drive the search for ground-state structure, hence *structure relaxation*), the KS eigenvalues $\epsilon_i$ provide an important portion of calculation results. The Janak's theorem [Janak, 1978] establishes the meaning of $\epsilon_i$ as derivatives of the total energy with respect to the occupation number of the corresponding electron state, $n_i$. We remind that in the HF theory, according to the Koopmans' theorem, the eigenvalues are "finite differences" between values of the total energy in two states of system in which the electron occupation numbers of the concerned electron state differ by one. Traced as functions of wavevector **k**, they represent *band structures*, and when integrated over the Brillouin zone they yield the *density of states*. The comparison of these properties with experimental results, e.g. photoemission or optical spectroscopy, even if not strictly justified, may often be instructive. "Not strictly justified" means that the "true" band gap has to do with excitations within a many-electron system rather than with one-electron (mean-field) properties. However, a more profound analysis (see, e.g., Perdew et al. [1982]) relates the "true" band gap with the "KS gap" (obtainable directly from the band structure) which has yet to be corrected by a term which, in the ideal case of "exact" (yet unknown) XC potential should take into account the fact that the total energy is a *piecewise linear* function of occupation numbers, the property which is not a priori present in LDA nor in the GGA. Due to this omission, the "KS gap" according to LDA or GGA is typically, and systematically, lower than the "true" value, which is routinely referred to as "gap problem". Among several ways suggested so far to cope with this problem, we single out (and use in the following) the hybrid approach.

## 2.5 Hybrid Functionals

An idea of hybrid functionals were first suggested by Becke [1993]. According to this idea, certain percentage of *exact exchange* energy (according to the HF scheme) replaces the corresponding fraction of the XC energy, calculated within a "conventional" DFT. These are sophisticated functionals known concerning the energetics of system, see e.g. see Ernzerhof and Scuseria [1999]. The amount of admixture is fixed by a coupling constant $\alpha$, which defines which percentage of HF is mixed with the DFT functionals e.g., as follows:

$$E_{XC} = (1-\alpha)E_{PBE} + \alpha E_{HF} \quad , \tag{2.10}$$

where $\mathrm{E_{PBE}}$ here and in the following will indicate the exchange-correlation energy as calculated at a GGA level according to initial prescription by Perdew, Burke and Ernzerhof [Perdew et al., 1996b], however, further on modified by [Perdew et al., 2008b] in their formulation of a GGA "revised for solids". This latter prescription, by now tested in an impressive number of publications, generally seems to yield acceptably accurate results concerning equilibrium structures and elastic properties for a large variety of densely packed solids and their surfaces. The (arbitrary) modification of the mixing parameter $\alpha$ brings with itself quite important variations of the results of DFT calculation, such as the vibration energies, or the band gap. Therefore, trading somehow the "first-principleness" of the approach for more accurate practical predictability, one can opt for tuning the value of $\alpha$ so as to faithfully reproduce some essential properties for a given class of materials. Following such tuning described in detail in the next chapter, we arrive at the optimal values $\alpha$=16% for inorganic halide perovskite and $\alpha$=19.87% from organic halide perovskite.

Further on, the numerical representation of density and potential may be constructed either by discretisation over a spatial grid or atom-centered radial mesh, or formulated in terms of expansions over appropriately chosen basis functions. Among the basis functions, two groups can be specially emphasized: delocalized ones (typically, plane waves) and atom-centered localized numerical or analytical functions. A vast literature exists on the relative merits and optimal domains of use of each of these two groups. In the present work, practical calculations have been done with the use of CRYSTAL code [Dovesi et al., 1988] (in particular, its CRYSTAL17 version, [Dovesi et al., 2018]) which was the pioneering software, nowadays leading with well established reputation of reliability, in the use of Gaussian-type basis functions in Hartree-Fock and DFT calculations on periodic solids. The Gaussian basis functions and their useful properties are discussed in the following.

## 2.6 Gaussian-type basis functions

Gaussian type orbitals (GTOs) are three-dimensional functions, usually (but not necessarily) "centered" at an atom, the angular form $(\theta, \phi)$ of which is represented by spherical harmonics, and the radial part – by a power function times Gaussian function with appropriate localization parameter $\beta$ :

$$G_{lmn}(r, \theta, \phi) = N_n r^{n-1} e^{-\beta r^2} Y_l^m(\theta, \phi) \quad . \tag{2.11}$$

The advantage of using such functions is that the multicenter integrals involving them can be calculated analytically, since a *product* of two Gaussian functions centered at different sites is a *sum* of some other Gaussian functions centered elsewhere, see e.g. Besalú and Carbó-Dorca [2011]. There is however a problem is their use, related to the fact that the radial shape of GTOs badly represents that of physical molecular orbitals: the GTOs do not possess a singularity at the origin which is a property of $s$-orbitals; moreover they fall down too fast at large distances from the center. For example, Slater-type orbitals (STO) $\sim r^n e^{-\alpha r}$ may serve to imitate the "natural" shape of the molecular orbitals much better. A standard practical way out of this difficulty is to use a (fixed) linear combination of several GTOs to approximate a single STO. The so formed combinations of (primitive) Gaussian functions are called contracted Gaussian functions.

The calculations done with GTO-type basis sets , as with any other system of basis functions centered on atoms, are vulnerable to Basis set superposition error which is explained in the following.

## 2.7 Basis set superposition error (BSSE)

This error has in its origin the fact that the basis set practically used is, out of technical necessity, *not complete*, so that the efficiency of minimizing the total energy by variational method (that is, in any self-consistency loop within electronic structure calculation) depends on the quality of the basis set available. As two atoms are close enough so that the basis functions centered on them do considerably overlap, the atoms may "borrow" the basis functions at a respective neighbour to "improve" the variational freedom of their "own" states. The overall "quality" of the basis is then not the same as when the atoms are placed at a distance, hence the energy in the extraction of, say, interaction energies can be erratic. Obviously, such kind of error does not come about if the basis set is fixed (e.g., consists of plane waves) and does not move with the atoms, even if such basis set is not complete either.

Consider a calculation of adsorption energy of a molecule on the surface, using the following "naive" formula:

$$\mathit{\Delta} E_{\text{adsorption}} = E_{\text{surface+mol}} - E_{\text{surface}} - E_{\text{mol}}\,. \tag{2.12}$$

$E_{\text{surface+mol}}$, meaning the result of a calculation for a combined system of a system with adsorbed molecule, is a priori "more accurately" estimated than in two others, "surface-only" and "molecule-only" calculations, simply for the reason that the two latter calculation operate with their correspondingly reduced basis sets and not the full (combined) one. Correspondingly, the calculated energy difference (i.e., adsorption energy) will suffer from a systematic error. One of the known methods suggested to eliminate BSSE is the counterpoise method, suggested by Boys and Bernardi [1970]. In this method, the consistency of the basis functions in the cases compared is maintained by introducing *ghost atoms* with their respective basis functions at the place of a (missing) neighbour to a molecule. In this way, the calculations for molecule and surface with molecule are done with exactly the same basis set. The expression for the adsorption energy of the molecule will then be as follows:

$$\Delta E^{CP}_{\text{adsorption}} = E_{\text{surface+mol}} - E_{\text{surface+ghost mol}} - E_{\text{mol+ghost surface}} \quad . \tag{2.13}$$

## 2.8 CRYSTAL17 code

The CRYSTAL program suite was designed to perform electronic structure calculations for periodic systems. In practical terms, this periodicity can be imposed in three dimensions (to treat crystals), in two dimensions (to treat films, slabs, or surfaces), in one dimension (to treat linear chain systems, e.g., like polymers) or in "zero dimension", i.e., excluded completely, for the treatment of isolated molecules or finite clusters. The package underwent a path of development and improvements since Dovesi et al. [1988] to its present version [Dovesi et al., 2018]. Within CRYSTAL, both the HF and KS equations, as well as hybrid schemes, can be solved self-consistently. The KS or HF orbitals are expanded over basis sets of GTOs discussed in Section 2.6. Closed shell and spin-polarised calculations can be performed. An "all-electron" approach is possible, within which all the orbitals from $1s$ onwards are explicitly included into the self-consistent scheme, with the use of the "full" potential, that is, without constraints on its spatial shape. One may choose the valence-only approach to certain atoms and treat other atoms according to the all-electron paradigm within the same calculation, guided by experience and the relative importance of different core states for the properties under study.

The use of "valence-only" scheme implies the use of *effective core pseudopotentials* (ECP) see Singh and Nordstrom [2006]. These are potentials acting on valence electrons in the presence of (excluded from the calculation) core electrons. By their constructions (see details in Martin [2004]; Dolg [2002]), these potentials are different (orbital moment dependent) in their action on different electron states, hence the definition "pseudo".

Pseudopotential implemented in CRYSTAL is a sum of three terms: Coulomb term (C), a local term (L) and a semi-local term (SL) [Dovesi et al., 2017]:

$$C = -Z_N/r \quad , \tag{2.14}$$

$$L = \sum_{k=1}^{M} r^{n_k} C_k e^{-\alpha_k r^2} \quad , \tag{2.15}$$

$$SL = \sum_{l=0}^{4} \left[ \sum_{k=1}^{M_l} r^{n_{kl}} C_{kl} e^{-\alpha_{kl} r^2} \right] P_l \quad . \tag{2.16}$$

$Z_n$ is the effective nuclear charge which is the difference of total nuclear charge and the number of electrons represented by effective core potential. $l$ is the angular quantum number and is related to the projection operator $P_l$. $C_{kl}$, $\alpha_k$, $\alpha_{kl}$, $M_l$, M, $n_{kl}$ are the pseudopotential parameters.

CRYSTAL can employ different sets of pseudopotentials, such as, Stuttgart-Dresden [Andrae et al., 1990], Durand and Barthelat [Durand and Barthelat, 1975], Hay and Wadt with small [Wadt and Hay, 1985] and large [Hay and Wadt, 1985d] cores.

In Stuttgart-Dresden, ECPs are of semi–local type and include non-relativistic and scalar-relativistic, spin-orbit and core-polarization potentials.

Durand and Barthelat [1975] developed an ECP that also is a semi-local shape-consistent type ECP. Hay and Wadt pseudopotentials also include scalar-relativistic effects and are used for transition and main group elements.

Stuttgart-Dresden fully relativistic pseudopotentials have been adopted for Br, I and Pb, and a Hay-Wadt pseudopotential for Cs in this work.

### 2.8.1 Theoretical framework within CRYSTAL code

Crystal17 uses CO-LCAO (linear combination of atomic orbitals) scheme for the treating periodic systems. CO is the crystalline orbital, $\psi$ (**r**; **k**), and in this case, CO is the linear combination of Bloch Functions, $\phi$(**r**; **k**) defined in terms of Atomic Orbitals, $\varphi_\mu(\mathbf{r})$.

$$\psi_i(\mathbf{r};\mathbf{k}) = \sum_{\mu} a_{\mu,i}(\mathbf{k})\phi(\mathbf{r};\mathbf{k}) \quad . \tag{2.17}$$

$$\phi_\mu(\mathbf{r};\mathbf{k}) = \sum_{\mathbf{K}} \varphi_\mu(\mathbf{r} - \mathbf{N}_\mu - \mathbf{K}) e^{i\mathbf{k}\cdot\mathbf{K}} \quad . \tag{2.18}$$

$\mathbf{N}_\mu$ is the nucleus' coordinate in the zero reference cell where $\varphi_\mu$ is centered, and the sum is extended over the set of all the lattice vectors, **K**. The local functions can be represented as linear combinations of (some number, n$_G$) individually normalised Gaussian type functions (GTO) with the same center and fixed coefficients, d$_j$ and exponents, $\alpha_j$ defined as:

$$\varphi_\mu(\mathbf{r} - \mathbf{N}_\mu - \mathbf{K}) = \sum_{j}^{n_G} d_j G(\alpha_j; \mathbf{r} - \mathbf{N}_\mu - \mathbf{K}) \quad . \tag{2.19}$$

These atomic orbitals of a given atom are assembled into shells, $\lambda$. These shells would include all the atomic orbitals with similar quantum numbers, $n$ and $l$, or these shells can also acquire atomic orbitals with similar principal quantum number, $n$ if the number of GTOs and their corresponding exponents are similar. The grouping of atomic orbitals can reduce the number of auxiliary functions which are required for the calculation of electronic integrals (see Pisani [1996] for details ) and thereby increase the calculation speed.

The coefficients of expansion of Bloch Functions, $a_{\mu,i}(\mathbf{k})$, are evaluated by solving the matrix equations at each reciprocal lattice vector: **k**.

$$F(\mathbf{k})N(\mathbf{k}) = S(\mathbf{k})N(\mathbf{k})E(\mathbf{k}) \quad , \tag{2.20}$$

where $S(\mathbf{k})$ is the overlap matrix for the Bloch Functions and $E$ (**k**) is the diagonal energy matrix and $F(\mathbf{k})$ is the Fock matrix:

$$F(\mathbf{k}) = \sum_{\mathbf{K}} F^{\mathbf{K}} e^{i\mathbf{k}\cdot\mathbf{K}} \quad . \tag{2.21}$$

The elements of matrix $F^{\mathbf{K}}$ can be expressed as a sum of one and two-electron contributions in atomic orbitals' basis set:

$$F^{\mathbf{K}}_{1\,2} = H^{\mathbf{K}}_{1\,2} + B^{\mathbf{K}}_{1\,2} \quad . \tag{2.22}$$

The sum of kinetic and nuclear interactions terms are included in one-electron contributions while Coulomb and exchange contributions are included in two-electron terms.

$$B^{\mathbf{K}}_{1\,2} = \sum_{3,4}\sum_{\mathbf{Q}} P^{\mathbf{Q}}_{3,4} \sum_{\mathbf{S}} [(\varphi_1^{\mathbf{0}}\varphi_2^{\mathbf{K}}|\varphi_3^{\mathbf{S}}\varphi_4^{\mathbf{S+Q}}) - \frac{1}{2}(\varphi_1^{\mathbf{0}}\varphi_3^{\mathbf{S}}|\varphi_2^{\mathbf{K}}\varphi_4^{\mathbf{S+Q}})] \quad . \tag{2.23}$$

The elements of density matrix, $P^{\mathbf{Q}}$, are evaluated by integration over the Brillouin zone volume.

$$P^{\mathbf{Q}}_{3,4} = 2\int_{BZ} d\mathbf{k} e^{i\mathbf{k}\cdot\mathbf{Q}} \sum_{n} a^{*}_{3n}(\mathbf{k}) a_{4n}(\mathbf{k}) \theta(\epsilon_F - \epsilon_n(\mathbf{k})) \quad , \tag{2.24}$$

where $a_{in}$ is $i$-th component of $n$-th eigenvector, step function is denoted by $\theta$, $\epsilon_F$ and $\epsilon_n$ are the Fermi energy and $n$-th eigenvalue respectively.

The total electronic energy per unit cell can be computed as:

$$E = \frac{1}{2}\sum_{1,2}\sum_{\mathbf{K}} P^{\mathbf{K}}_{1\,2}(H^{\mathbf{K}}_{1\,2} + B^{\mathbf{K}}_{1\,2}) \quad . \tag{2.25}$$

In CRYSTAL17, the idea to simulate the unpaired electrons are realized through spin polarised calculation. In the case of a system with all electrons paired, the latter referring to "up spin" and "down spin" states are restricted to the same spatial orbital. In case of spin polarised calculations, the spatial degeneracy of the orbitals marked by different spins does not hold anymore. In this work calculations of a priori or supposedly magnetic systems, for instance all cases involving the $O_2$ molecule, have been carried out with spin polarisation. Also, for the simulation of neutral vacancy, spin polarised approach is used, the reasons and implications of which are discussed in detail in Chapter 3.

### 2.8.2 Phonon calculation

Lattice dynamics is involved in the second-order derivatives of energy with respect to the nuclear coordinates. Some of the important physical properties, such as the vibration spectra, thermal expansion, specific heat can be obtained. The vibration spectra

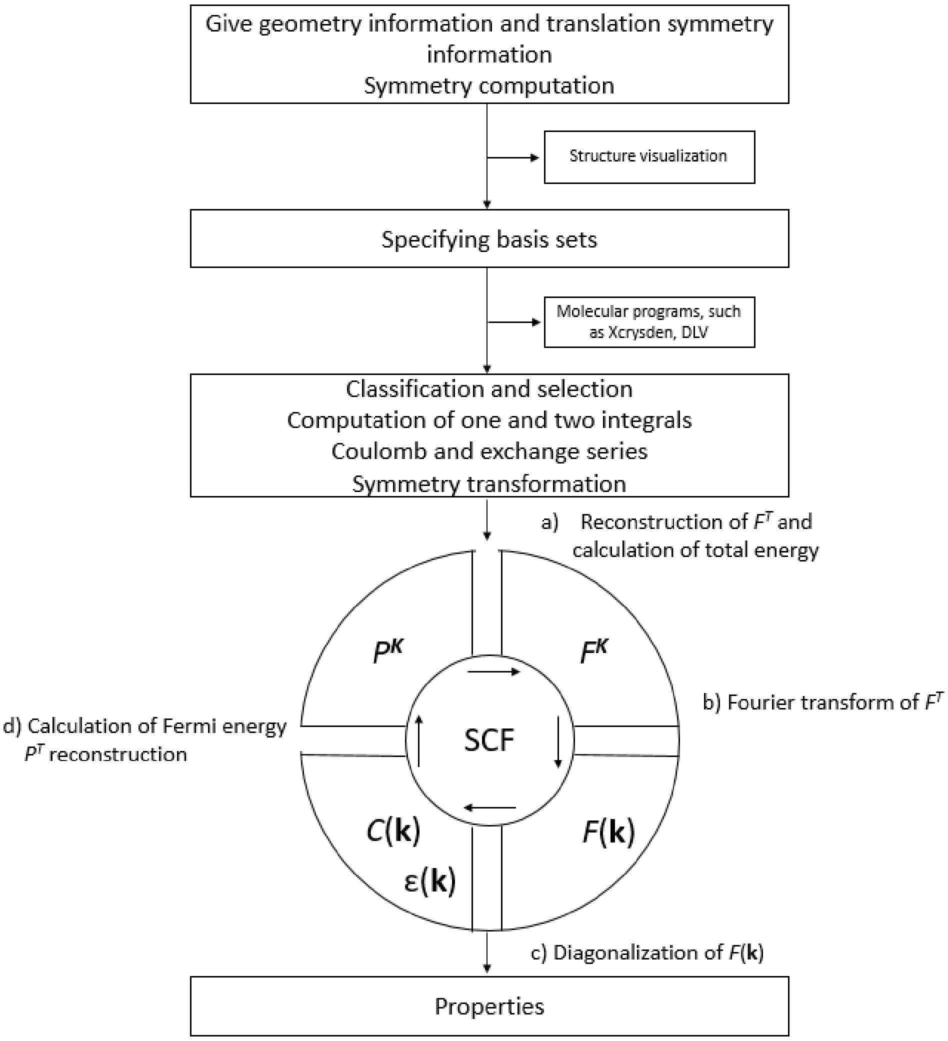

FIGURE 2.1: Flow chart of CRYSTAL code [Pisani, 1996]

can provide information about the stability of structure. The decoupling of electrostatic motion from nuclear motion through the Born-Oppenhimer approximation is the basic assumption for computing lattice dynamics. Under these approximations, the second derivatives of total energy with respect to the deviations **u** of nuclei from their equilibrium positions gives the force constants relative to all pairs of nuclei in the lattice.

$$H_{ij}^{g} = \frac{\partial^2 E}{\partial \mathbf{u}_{Ai}^{0} \partial \mathbf{u}_{Bj}^{\mathbf{g}}} \quad , \tag{2.26}$$

Eq. (2.26) represents one element of Hessian matrix relative to the oscillations along the $i^{th}$ coordinate of A atom in the 0 cell and along the $j^{th}$ coordinate of B atom in the **g** cell (because of the lattice transnational invariance one atom can be considered in the 0-cell). The size of Hessian matrix for a crystal can be infinite. However, the derivatives of energy have the same periodicity as does the potential energy, i.e., the periodicity of the lattice. Therefore, the oscillating nuclei in the lattice, should they be described by their respective vibrational wave functions, must also obey the Bloch theorem.The Hessian matrix can be made dependent on the reciprocal lattice vector, instead of be numbered by all possible atom pairs, by force of the lattice Fourier transform. The square matrix is associated with a **k** point within the reciprocal space and it can be obtained by Fourier transformation of Eq. 2.26

$$H_{ij}(\mathbf{k}) = \sum_{\mathbf{g}} e^{i\mathbf{k}\cdot\mathbf{g}} H_{ij}^{\mathbf{g}} \quad . \tag{2.27}$$

This lattice summation is done for each pair of atoms populating the unit cell, previously numbered by (A,B). Here, these indices are omitted for brevity.

For any reciprocal-space vector **k**, residing in the first Brillouin zone, the frequencies and eigenvectors of lattice vibrations can be obtained by diagonalising the matrix $\mathit{\Omega}$, following from Hessian by simply rescaling the latter with masses of atoms in the unit cell. Without applying any symmetry considerations, the size of the matrix is three times the number of atoms in the unit cell $N$.

As the **k** vector varies, the $3N$ solutions for vibration frequencies vary along (possibly degenerate) branches, revealing the *phonon dispersion*.

At $\mathit{\Gamma}$ point, the frequency is zero for the three branches. These modes are associated with translation of the whole crystal within the space in any direction. They are called *acoustic* modes. Vibration modes within other branches than these three, in which different atoms within the unit cell does not move in an identical way, are referred to as *optical* modes.

Once the dispersion relation is known, thermodynamical properties can be computed using statistical mechanics equations. One of such properties, the Helmholtz Free energy, $F$ can be calculated as:

$$F = \sum_{n,\mathbf{k}} \frac{1}{2}\hbar\omega_{n\mathbf{k}} + k_B T ln[1 - exp(-\frac{\hbar\omega_{n\mathbf{k}}}{k_B T})] \quad , \tag{2.28}$$

where $k_B$ is the Boltzmann constant and the sum is for all the lattice vibrations $\omega_{n\mathbf{k}}$.

## 2.9 Computational details

As regards the atomic basis sets, all-electron GTFs has been used for the carbon [Dovesi et al., 1990], oxygen [Sophia et al., 2013] and chlorine [Apra et al., 1993] while the Stuttgart-Dresden fully relativistic pseudopotentials have been adopted for Br [Peterson et al., 2003], I [Peterson et al., 2006] and Pb [Metz et al., 2000], and a Hay-Wadt pseudopotential for Cs [Hay and Wadt, 1985a,b,c].

The $3s$, $3p$, $3d$, $4s$ and $4p$ electrons of Br, $4s$, $4p$, $4d$, $5s$ and $5p$ electrons of I, $5s$, $5p$ and $6s$ electrons of Cs, and the $5s$, $5p$, $5d$, $6s$ and $6p$ electrons of Pb are treated as valence electrons in order to guarantee a good description of the structural and electronic properties of each perovskites with respect to experiment. The description of the basis sets are given in detail in Appendix A.

The Cl, Br, I, C and O and Pb basis sets are fully described in Appendix.

For the evaluation of the Coulomb and exchange series within CRYSTAL, the truncation thresholds for the bielectronic integrals were set to $10^{-8}$ (overlap threshold for Coulomb integrals), $10^{-8}$ (penetration threshold for Coulomb integrals), $10^{-8}$ (overlap threshold for HF exchange) , $10^{-8}$ (pseudo-overlap HF series) and $10^{-16}$ (pseudo-overlap HF series) a.u., respectively. When the bielectronic integrals values are smaller than the above mentioned parameters, the corresponding overlap value is not considered. The details can be found in the the CRYSTAL manual [Dovesi et al., 2017].

The calculations have been performed with a 14 × 14 × 14 and a 6 × 6 Monkhorst–Pack $k$-meshes [Monkhorst and Pack, 1976] for the bulk materials and the surfaces, respectively. The convergence criteria on total energies (and for the elastic constants and frequencies determination) were $10^{-9}$ ($10^{-12}$) Ha. Atomic displacements and forces thresholds were $1.8 \cdot 10^{-3}$ Bohr and $4.5 \cdot 10^{-4}$ Ha/Bohr, respectively. The details of calculations is discussed in the next Chapter. With these computational conditions, the obtained data can be considered as fully converged.

# Chapter 3

# Modelling of organic/inorganic halide perovskites: bulk and surfaces

In this chapter, we discuss the applications of the DFT in general, including the bulk and surface properties and the CRYSTAL method in particular to halide perovskites in order to stipulate some primary results and to set up further calculations on more complex perovskite systems.

Organic/inorganic halide perovskites exist in different phases (cubic, tetragonal, orthogonal), as discussed in chapter 1. The cubic phase (space group $Pm\bar{3}m$) is the high-temperature phase, which is suitable for photovoltaic applications. At the start of the calculation, the information of the Bravais lattice and atomic positions of cubic phase ($Pm\bar{3}m$) for organic and inorganic halide perovskites is taken from the literature [Jain et al., 2013; Brivio et al., 2015; Moller, 1958; Murtaza and Ahmad, 2011; Trots and Myagkota, 2008; Ma et al., 2017]. This is when several calculation parameters, essential for the accuracy of results and the efficiency of calculation, should be tested and fixed for subsequent use. In the following, we address these parameters one by one. After setting the parameters, the discussion is carried out to the slabs and the perfect surface (for organic/inorganic halide perovskite) followed by the halide vacancy defects (charged/neutral) on the surface of inorganic halide perovskites.

## 3.1 Parameters for the calculations

### 3.1.1 k-point sampling

Electron wavefunctions $\varphi_i(\mathbf{r}, \mathbf{k})$ and Kohn–Sham energies $\epsilon_i(\mathbf{k})$ in a periodic solid are numbered, among other quantum numbers, by values of wavevector $\mathbf{k}$ which are quasi-continuously distributed in the Brillouin zone. Any summation over electronic states, for example, in order to calculate charge density, total energy, or transport properties, would then involve integration over the Brillouin zone. In practical terms, this continuous integration is replaced by discrete summation or sampling, over a *mesh* of **k**-points generated with a certain density. Details of this procedure come back to Monkhorst and Pack [1976]. The appropriate number of **k**-points depends on the type of system. A denser **k**-points mesh improves the accuracy of calculation but consumes more computational resources.

The density of **k**-points mesh is tested against the bandgap of the system. Corresponding results of trial calculations are shown in Figure 3.1. One can conclude that the calculated band gap value stabilizes to $\sim$1 meV for the **k**-mesh with 12×12×12 divisions (along the reciprocal lattice vectors) for $CsPbCl_3$ and $CsPbBr_3$, whereas calculations for $CsPbI_3$ demand a bit denser mesh of 14×14×14, that can be due to a more covalent character of iodine–halogen bonding and comparatively larger lattice parameter. Bandgap, an important parameter characterising systems subject to optical excitations, is a property of particular attention in this work. Inorganic halide perovskites in their cubic phase show a direct bandgap. For systems with direct/indirect bandgap, the effect of **k**-mesh plays a role via the general accuracy of the calculation. More accurate **k**-space integration results in more accurate density, which gives more accurate potential resulting in a more accurate band structure. Keeping in mind the consumption of computational resources and not compromising with the accuracy in the bandgap, the **k**-mesh density corresponding to 14×14×14 divisions over the Brillouin zone of cubic perovskite was retained in subsequent calculations.

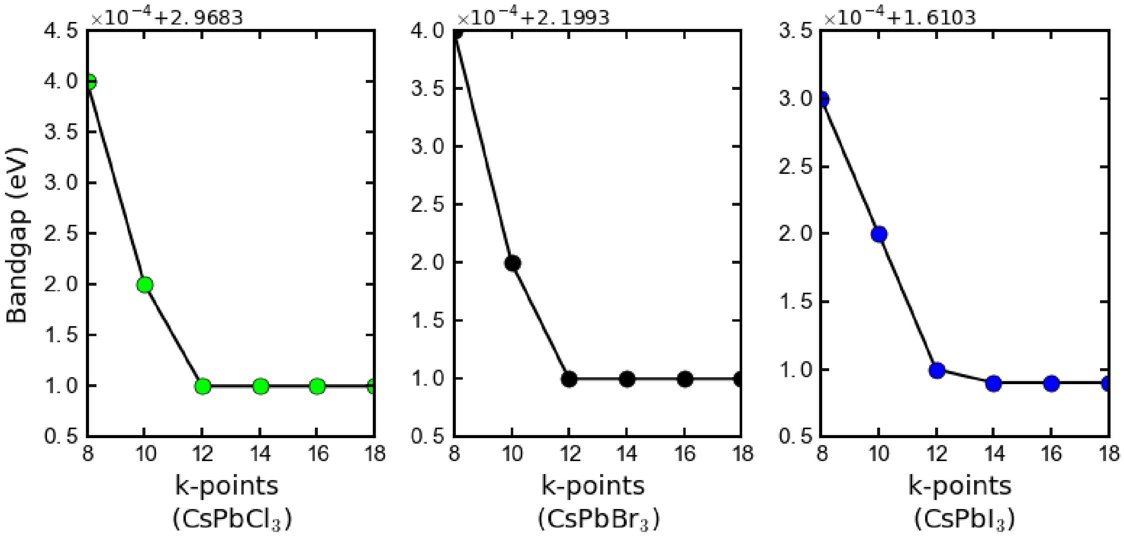

FIGURE 3.1: Calculated bandgap of cubic ($Pm\bar{3}m$ phase) $CsPbCl_3$, $CsPbBr_3$ and $CsPbI_3$ perovskites vs number of divisions in **k**-points sampling.

## 3.1.2 Hybrid Functional

In the attempts to accurately reproduce the ground-state properties (lattice parameters, equilibrium geometry) *and* properties related with excitations (bandgap, dielectric function) in practical DFT calculations, many researchers resort to the use of hybrid XC functionals. These functionals employ a certain admixture of the “exact” HF exchange to the expression for the “conventional” XC functional defined within one or other schemes. While intended to be suitable for general enough use, the hybrid functional is subjected to more or less “intelligent” choice of the mixing scheme and proportions of exact exchange and exchange-correlation. In practical terms, a priori accepting a nearly phenomenological nature of such adjustment, one faces a necessity of compromise between applicability to possibly many systems and high accuracy in the description of at least some of them. This approach allows to define the Hamiltonian best suited for describing the properties of a given family of materials. For example, recently it was used efficiently for the study of the influence of alkali metals on the properties of chalcopyrites [Lafond, 2019]). In this work, we neglect the spin-orbit interactions as they will have negligible contributions in the adsorption energy, which is focused in this work.

In the present work, the hybrid functional was optimised, specifically for the applications to halide perovskites. The target systems for tuning of hybrid functionals were $CsPbX_3$ (X=Cl, Br, I), and target properties – equilibrium lattice constant and bandgap. Table 3.1 shows the bandgap values for three perovskites, as calculated with different flavours of XC potentials. Among them are GGA functionals, such as PBE [Perdew et al., 1996b], PBEsol [Perdew et al., 2008a], which is a revised version of PBE for solids. Further on, the table includes results for PBE0 [Perdew et al., 1996a] and PBEsol0 (derived from PBE0) due to Adamo et al. [1999]; this latter mixes PBE exchange energy with some fixed percentage of HF exchange. Further on, the table includes B3LYP [Vosko et al., 1980], where Becke's three parameters functional combined with LYP, a non-local correlation part, and HSE06 [Heyd et al., 2003], which uses error function screened Coulomb potential to calculate the exchange part. With all these mentioned functionals, the lattice parameter was optimised and then the bandgap value was extracted. For one of GGA schemes, the PBEsol functional, the effect of additional admixture of the HF exchange according to Eq. 2.10 was explicitly studied, in order to inspect how sensitive the optimised lattice parameter and the corresponding band gap would be to the mixing coefficient. The percentage relative error in the bandgap, referred to the experimental value, is shown in Figure 3.2. The relative error in the lattice parameter did not exceed $10^{-3}$ throughout the range of mixing studied, and hence is not specially addressed. Based on these results, the admixture level of 16% has been taken as a reasonable compromise value minimises the band gap value and lattice parameter error for the three systems studied.

As can be seen from Table 3.1, GGA functionals, such as PBEsol and PBE, underestimate the bandgap. Global hybrid functional, such as B3LYP, HSE06, PBE0, overestimate the bandgap and lattice parameter. Hybrid functional (PBEsol + 16% of HF exchange) optimised with an appropriated admixture of HF percentage is found to be more accurate in this sense than the other ones, yielding an error in the band gaps close to 6% for $CsPbI_3$, 4% for $CsPbBr_3$ and 3% for $CsPbCl_3$, whereas the error in the lattice the parameter is around 0.001% for the three compounds.

For $MAPbI_3$ and $FAPbI_3$, the hybrid functional used is a mixture of GGA functional, PBE and 19.87% of HF exchange. For MAPI, the error in bandgap with used

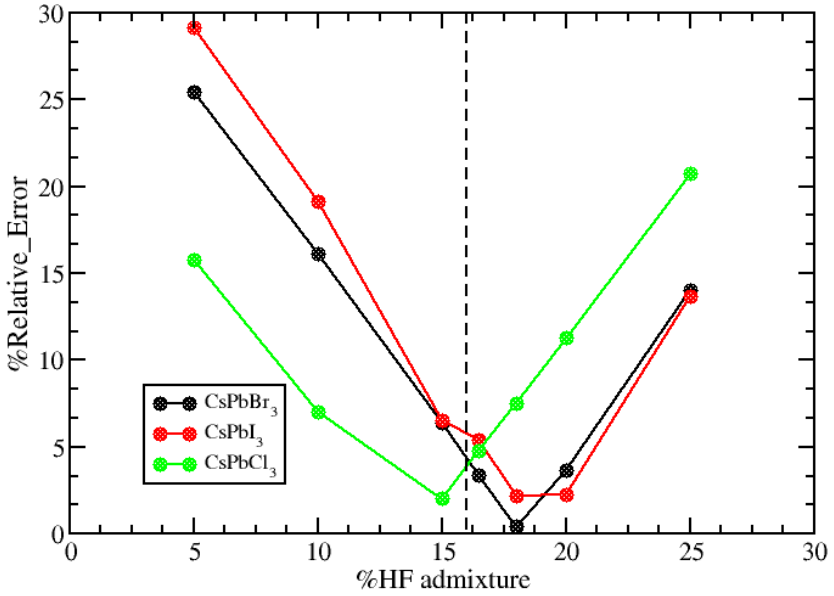

FIGURE 3.2: Percentage relative error in the band gap with respect to value obtained from calculation against the experimental value for cubic ($Pm\bar{3}m$) CsPbX$_3$ (X=I, Br, Cl) perovskites tested for PBE functional revised for solids with admixture of different percentage of HF exchange.

TABLE 3.1: Bandgaps ($E_g$, in eV) and lattice parameters ($a$, in Å) calculated using different functionals (using CRYSTAL17) for CsPbX$_3$ type perovskites (see text for details).

| Functional | CsPbI$_3$ | | CsPbBr$_3$ | | CsPbCl$_3$ | |
|---|---|---|---|---|---|---|
| | $a$ | $E_g$ | $a$ | $E_g$ | $a$ | $E_g$ |
| PBE | 6.308 | 1.41 | 5.995 | 1.91 | 5.762 | 2.45 |
| PBEsol | 6.198 | 1.20 | 5.884 | 1.50 | 5.661 | 2.21 |
| PBEsol0 | 6.202 | 1.95 | 5.885 | 2.70 | 5.660 | 3.42 |
| B3LYP | 6.393 | 2.41 | 6.062 | 3.02 | 5.816 | 3.65 |
| HSE06 | 6.284 | 1.90 | 5.968 | 2.45 | 5.734 | 3.25 |
| PBE0 | 6.283 | 2.45 | 5.968 | 2.51 | 5.735 | 3.25 |
| Hybrid | 6.196 | 1.61 | 5.884 | 2.20 | 5.659 | 2.91 |
| Exp | 6.198[a] | 1.73[b] | 5.883[a] | 2.30[c] | 5.660[a] | 2.86[c] |

[a] Moreira and Dias [2007]; [b] Eperon et al. [2015]; [c] Liu et al. [2013].

Hybrid functional is close to 1%, and within the lattice parameter, the error recorded is around 0.001%.

## 3.2 Bulk properties of perovskites

With the parametrisation of hybrid functionals thus fixed, we now turn to discussing the results of hence resulting crystal structures at equilibrium.

### 3.2.1 Lattice parameter and internal coordinates

Structural optimisation is carried out for organic/inorganic halide perovskites in order to estimate the equilibrium lattice parameter. The corresponding results are shown in the table 3.2.

For $CsPbX_3$ (X=I, Br, Cl), the high-temperature cubic phase ($Pm\bar{3}m$) is used initially, the lattice parameter and the internal coordinates are optimised. The perovskite-type materials are known to develop structure instabilities, which can be grasped as softening of particular phonon modes (see, for instance, Yang et al. [2017], concerning the instabilities in $CsPbX_3$ materials). The most typical is the zone-boundary instability, which manifests itself as a tilting of the $PbX_6$ octahedra leading to the cubic to tetragonal phase transition (see Figure 1.2). In a calculation, the instability reveals itself as a softening, i.e. exhibiting low frequency squared and even getting the frequency imaginary, of a particular vibration mode over certain areas of the Brillouin zone. In the cubic phase, instability is present along the edges of the Brillouin zone (see Figure 3.3

TABLE 3.2: Calculated lattice parameters ($a$, in Å) and optical band gap ($E_g$, in eV) for the cubic structure (space group $Pm\bar{3}m$) of the $CsPbX_3$ (similar to the Table 3.1 using of hybrid functionals), $MAPbI_3$ and $FAPbI_3$ (pseudo cubic phase) perovskites, as determined with the hybrid functional used. The experimental data are given for comparison.

| Compound | $a$ | | $E_g$ | |
|---|---|---|---|---|
| | Calc. | Exp. | Calc. | Exp. |
| $CsPbI_3$ | 6.196 | 6.198[a], 6.289[b], 6.177[c], 6.189[d] | 1.61 | 1.73[c,d], 1.76[e] |
| $CsPbBr_3$ | 5.884 | 5.883[a], 5.870[b], 5.874[e,f] | 2.20 | 2.30[g] |
| $CsPbCl_3$ | 5.659 | 5.660[a], 5.605[e] | 2.91 | 2.86[g] |
| $MAPbI_3$ | 6.363 | 6.330[h] | 1.62 | 1.60[i] |
| $FAPbI_3$ | 6.428 | 6.362[j] | 2.04 | 1.48[k] |

[a] Moreira and Dias [2007]; [b] Stoumpos et al. [2013a] ; [c] Eperon et al. [2015]; [d] Swarnkar et al. [2016]; [d] Møller [1958]; [e] Lai et al. [2017] (nanowires); [f] Natarajan and Prakash [1971]; [g] Liu et al. [2013]; [h] Poglitsch and Weber [1987]; [i] Noh et al. [2013]; [j] Leblanc et al. [2019]; [k] Eperon et al. [2014].

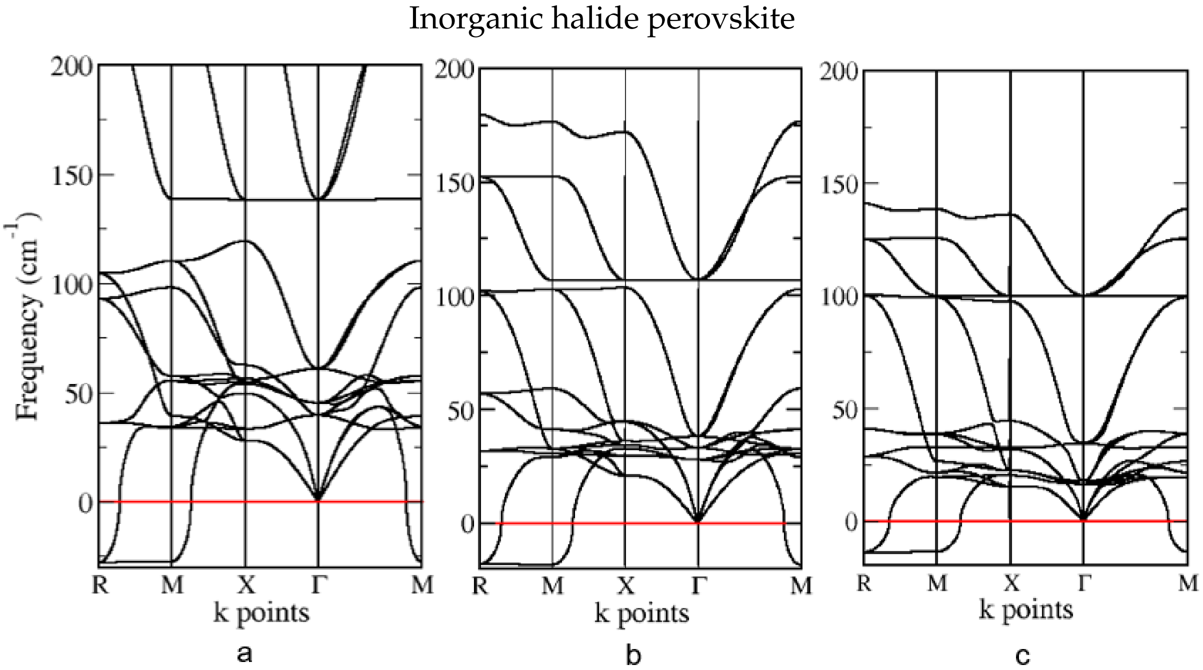

FIGURE 3.3: Phonon dispersion curves for bulk perovskites with $Pm\bar{3}m$ cubic phase calculated along high-symmetry lines of Brillouin Zone $\Gamma$ (0 0 0), X (0$\frac{1}{2}$0), M ($\frac{1}{2}\frac{1}{2}$0), R ($\frac{1}{2}\frac{1}{2}\frac{1}{2}$) for inorganic halide perovskite a) $CsPbCl_3$, b) $CsPbBr_3$ and c) $CsPbI_3$ in cubic phase.

a b and c). For resolving the instability, as indicated by the phonon eigenvector of the corresponding unstable mode, the symmetry constraints were removed subsequently (lowering of symmetry from cubic to orthorhombic one) for structure relaxation, and structure optimisation was redone. The final structure is in the orthorhombic phase ($Pnma$). In the case of $CsPbI_3$, the orthorhombic phase formed is distorted and of type $Amm2$.

In the case of MAPI, similar to $CsPbX_3$ perovskites, the initial structure used is the high-temperature cubic one, for which the lattice parameter and the internal coordinates were optimised. On lowering of symmetry from cubic to orthorhombic, the structure is re-optimised. The final structure is in the orthorhombic phase ($Pnma$).

In case of FAPI, the initial trial structure was taken orthorhombic, as suggested by Weller et al. [2015]. Figure 3.4 a, b describes the tilting of octahedra and arrangement of organic molecule in rhombohedral phase of MAPI and FAPI respectively.

The organic molecules in the organic halide perovskites are polar. The MA molecule has a dipole moment of 2.46 D, pointing from carbon towards the nitrogen, whereas

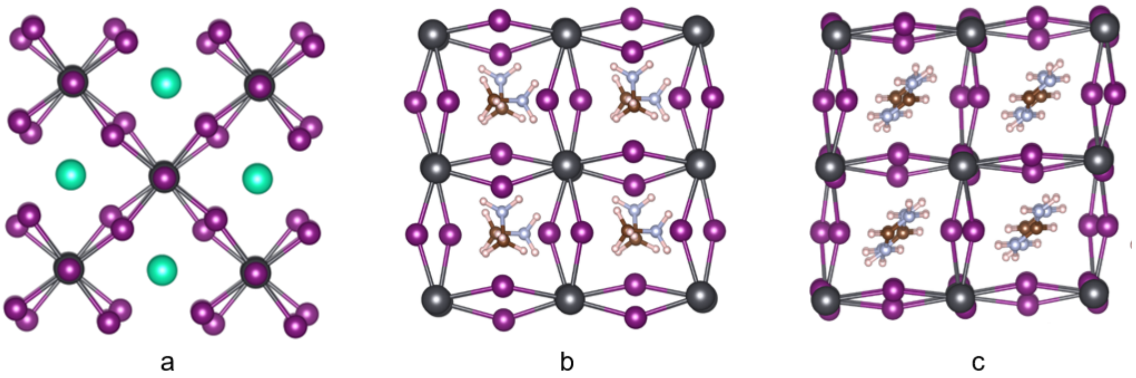

FIGURE 3.4: [100] view of tetragonal phase of a) $CsPbI_3$ and rhombohedral phase of b) MAPI c) FAPI.

the FA molecule has a dipole moment of 0.74 D pointing in the direction opposite to H–C bond as indicated in Figure 3.5. The phase transitions in the organic halide perovskites result from a complex interplay between dipole-dipole interactions, steric and electrostatic interactions between the organic cations, lead-halide lattice, and tilting of lead-halide octahedra. This can result in the organised arrangement of organic cations, which can influence the electronic structure of these materials. The details of the effects of the rotation of organic cations (MA and FA) on the properties of organic halide perovskite are discussed elsewhere [Maheshwari et al., 2019; Carignano et al., 2016].

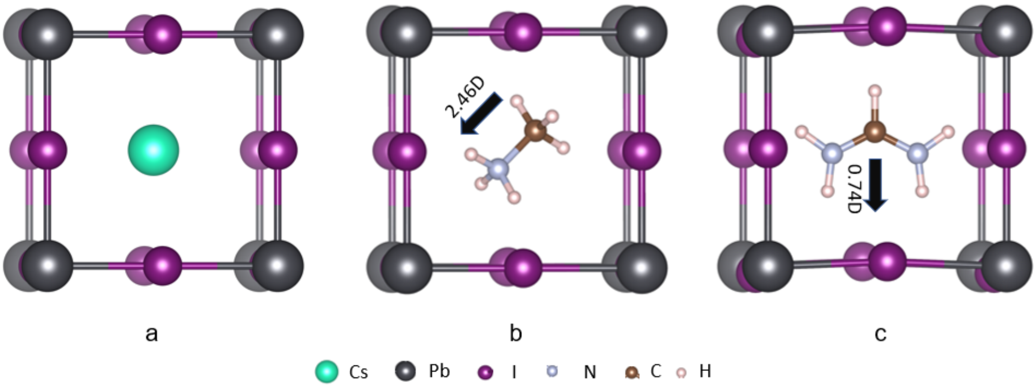

FIGURE 3.5: Tilted [100] view of pseudo cubic phase of perovskites with different cations in the center of cage formed by PbI units: a) $CsPbI_3$, b) MAPI and c) FAPI. The arrow indicates the direction of the dipole moment of the organic cation.

TABLE 3.3: Band gaps (in eV) for different phases of organic /inorganic halide perovskites.

| Compound | phase (space group) | | |
|---|---|---|---|
| | cubic | tetragonal | orthorhombic |
| $CsPbI_3$ | 1.61 | 1.85 | 3.49 |
| $MAPbI_3$ | 1.62[a] | 1.71[a] | 2.24[a] |
| $FAPbI_3$ | 2.07* | 2.21 | 2.04 |

[a] Baranek [2019]

* Band gap value for FAPI is of pseudo cubic phase.

### 3.2.2 Electronic properties

Out of the different crystalline structures of perovskites, the cubic phase for each compound seems to be best suited for the photovoltaic applications because of its band gap being about optimal (around 1.6 eV). A phase transition from cubic to tetragonal or orthorhombic phase brings changes in the electronic structure and hence influences the electronic properties [Yang et al., 2017; Stoumpos and Kanatzidis, 2015].

The bandgap in halide perovskite depends on the chemical nature of A, B and X atoms and also is influenced by the crystalline symmetry of valence band maximum (VBM) and conduction band minimum (CBM) [Meloni et al., 2016]. VBM is formed by combination of antibonding $n$s and $m$p orbitals of B and X atom, that would mean e.g., (Sn-5$s$, Pb-6$s$) and (I-5$p$, Br-4$p$, Cl-3$p$) respectively. These orbitals have a high covalent character with B/X orbital contribution around 30-40/70-60% depending on the crystal symmetry and chemical nature of A, B and X atoms. The CBM is formed by the combination of antibonding $np$ and $ms$ orbitals of B and X atoms, respectively. These orbitals are more ionic, in contrast to those present at the VBM, so that the orbital contribution of the B atom is around 70–90%.

From Table 3.3, different phases of perovskite show different bandgaps, which is due to the changing symmetry from cubic to orthorhombic phase. This change in symmetry results in the reduced overlap between $ns$ orbitals of B atom and $mp$ orbitals of X atom forming the VBM [Meloni et al., 2016]. In the cubic phase, the $mp$ orbitals of X are aligned along the B–X bond. The nature of alignment gets worse for tetragonal and orthorhombic phases. For the cubic system, the size of the A cation affects the lattice parameter, which, in its turn, affects the B-$ns$/X-$mp$ orbital overlap. However, for tetragonal and orthorhombic systems, the size of the cation and the tilting angles influence the overlap of B-$ns$/X-$mp$ orbitals.

From the Figure 3.6, $CsPbX_3$ perovskites (cubic phase), MAPI (rhombohedral phase) and FAPI (orthorhombic) show a direct bandgap at $R$ $(\frac{1}{2}\frac{1}{2}\frac{1}{2})$ point of the Brillouin zone.

## 3.3 Surfaces of perovskites

In order to study adsorption from first principles, a practical model of the crystal surface has to be first created for the calculation. Two surfaces simultaneously can be generated by cutting a crystal along a crystallographic plane, moving the pieces apart while maintaining periodic boundary conditions in all three directions. The thickness of the repeated layer (slab) between the two surfaces and the thickness of the "vacuum gap" added on separating the surfaces, as well as the shape of the lateral (two-dimensional) unit cell in the plane parallel to the surface, can be freely chosen.

One can underline an essential technical difference between methods that use plane waves as basis functions and those which rely on atom-centred localised functions. In the first case, the number of basis functions and hence the computational load increases with the size of the unit cell, be it filled with atoms or remain empty. In the

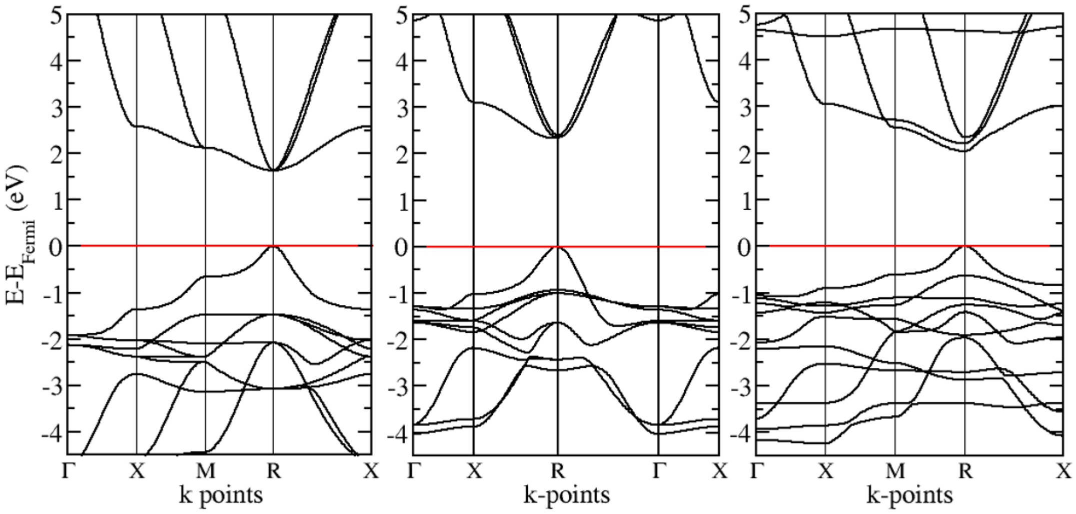

FIGURE 3.6: Band structure for bulk perovskites calculated along high-symmetry lines of Brillouin Zone from $\Gamma$ (0 0 0) to X $(0\frac{1}{2}0)$, M $(\frac{1}{2}\frac{1}{2}0)$, R $(\frac{1}{2}\frac{1}{2}\frac{1}{2})$ for a) $CsPbI_3$ (cubic), b) MAPI (rhombohedral) and c) FAPI (orthorhombic)

second case, to which namely belong the use of the CRYSTAL code, only the number of actually present atoms matters, whereas the size of the unit cell as such is not of immediate importance. As the slab geometry implies periodicity also in the direction perpendicular to the surface and hence a possibility of a spurious interaction of atoms across the vacuum gap, the interest of minimising this effect demands to increase the vacuum gap. Since Gaussian-type functions have an infinite extension (even if they are well localised), their overlap across the vacuum gap is always technically present. A sufficient length of the vacuum gap should be chosen at which this interaction could be considered negligible. In our calculation, the interlayer distance between the two periodically separated slabs in the direction normal to the surface is technically set to 500 Å.

### 3.3.1 Thickness of $CsPbX_3$ slabs

In the study of $CsPbX_3$ perovskites, the (001) surface has been considered which offers two types of termination: CsX and $PbX_2$. Both being saturated concerning the formal valence of the constituents, the slabs are not stoichiometric as a whole. To avoid spurious polarisation across the slab, the symmetry of the slab concerning its median layer is maintained. To ensure that the the thickness of the slab be sufficient, the formation energies have been calculated for a different number of layers in the slab. Note that we are not interested in calculating the absolute formation energy of slabs, to which there would be conceptual obstacles, but rather try to control the convergence of results as a function of the slab thickness, in view of getting results relatively independent on the latter.

The slabs so formed are non-stoichiometric. To calculate the formation energy, the energy of the slab formation is added with the energy of the cubic bulk CsX/$PbX_2$ (depending on the termination) to make the slab stoichiometric. The sum of energy obtained is subtracted from the number ($n$) of bulk $CsPbX_3$ units, the reference system in our case. The formation energy for CsX and $PbX_2$ terminated structures are given as:

$$E^{\mathrm{slab}}_{\mathrm{form}} = E^{\mathrm{slab}}_{\mathrm{CsPbX_3}} + E^{\mathrm{bulk}}_{\mathrm{CsX}} - nE^{\mathrm{bulk}}_{\mathrm{CsPbX_3}}, \qquad \text{(for PbX}_2\text{ termination)} \tag{3.1a}$$

$$E^{\mathrm{slab}}_{\mathrm{form}} = E^{\mathrm{slab}}_{\mathrm{CsPbX_3}} + E^{\mathrm{bulk}}_{\mathrm{PbX_2}} - nE^{\mathrm{bulk}}_{\mathrm{CsPbX_3}}, \qquad \text{(for CsX termination)} \tag{3.1b}$$

where $n$ is the number of bulk $\mathrm{CsPbX_3}$, $E^{\mathrm{bulk}}_{\mathrm{CsPbX_3}}$ is the energy of bulk $\mathrm{CsPbX_3}$, $E^{\mathrm{bulk}}_{\mathrm{CsX}}$ is the energy of bulk CsX and $E^{\mathrm{bulk}}_{\mathrm{PbX_2}}$ is the energy of bulk $\mathrm{PbX_2}$. The formula works as follows, taking the results shown in Figure. 3.7 as an example. In case of CsBr termination, the (non-stoichiometric) slab consists of 11 layers and contains 27 atoms. $E^{\mathrm{slab}}_{\mathrm{CsPbX_3}}$ is the energy of the slab. To restore the stoichiometricity, an additional $\mathrm{PbBr_2}$

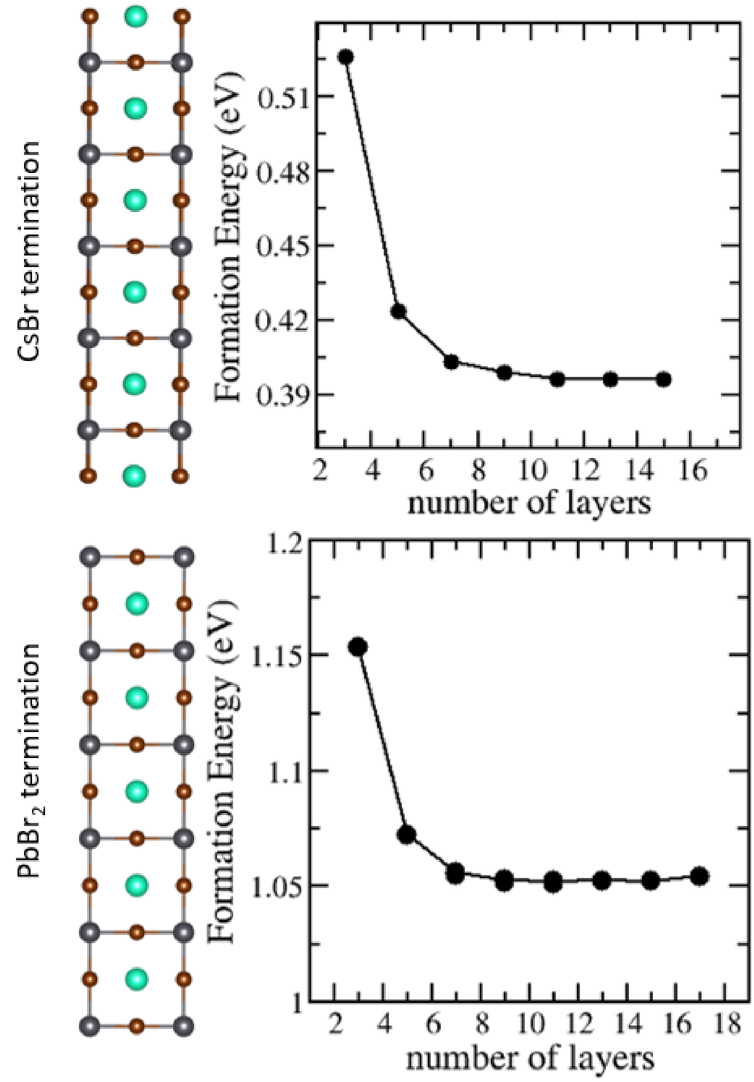

FIGURE 3.7: Formation energy of CsBr and $\mathrm{PbBr_2}$ terminated structure plotted against the number of layers of slab. See text for details.

unit will be required. To make the necessary correction, the total energy is added corresponding to a formula unit of bulk cubic $PbBr_2$ ($E^{\mathrm{bulk}}_{\mathrm{PbX_2}}$). The total energy of the thus "constructed" stoichiometric slab ($Cs_6Pb_6Br_{18}$) is subtracted from $6\times E^{\mathrm{bulk}}_{\mathrm{CsPbX_3}}$ to calculate the formation energy of the slab.

Eglitis and Vanderbilt [2007] suggested a method for the calculation of formation energy of the slabs. The reference system (bulk) adopted in their work and our work is similar, but the calculation of formation energy of the slab is different (see Eglitis and Vanderbilt [2007] for details). The conceptual problem of calculating the surface formation energy of a compound like a present one is that every cut along with a (001) plane would create two different surfaces simultaneously, and the energy attributed to one or the other type of surface cannot be specified without ambiguity. In our method of calculating the formation energy of the slab, the source of such ambiguity is a a procedure of "merging" the slab total energies with those from bulk CsX or $PbX_2$ types. However, this helps to recover the "reasonable" / comparable orders of magnitude for the surface formation energies to discuss them on equal footing. Moreover, as indicated above, the absolute energy values are not our primary interest, but their convergence is important, and the latter depends on the slab thickness.

In Figure 3.7, for CsX and $PbX_2$ terminated structures, the formation energy of the slabs is plotted against the thickness of the slab. The convergence of formation energy stabilises within the limit of 0.001 eV. For each termination, 11 layer slabs were sufficiently thick to be proceeded to the next step to study adsorption.

### 3.3.2 Thickness of FAPI slabs

In the case of FAPI, 2-D slabs are created by cutting the crystal along (100), (001) and (010) planes for cubic and tetragonal phases. Sufficiently thick slabs are needed for carrying out adsorption; for this reason, the slabs were created of different thicknesses, and the formation energy of each slab (orthorhombic phase) is calculated using the same formula mentioned in the equation 3.1.

For different terminations, the formation energies of slabs are plotted against the layer thickness of the slab (see Figure 3.8). For the (001) slab, the formation energy stabilises up to 0.001 eV after 11 layers of thickness for both FAI and $PbI_2$ terminations.

For (010) surface, convergence is reached after 15 layers for both types of termination with an accuracy of 0.001 eV.

As discussed before, the dynamics of the FA molecule influences the electronic structure of the halide perovskite [Carignano et al., 2016; Maheshwari et al., 2019]. The reason for an ominous convergence of energy of (100) slab is linked to the dynamics of the FA molecule. In the first two cases, those of the (001) and (010) surfaces, the molecule is intentionally kept constrained within its plane, which is the symmetry

FAI termination

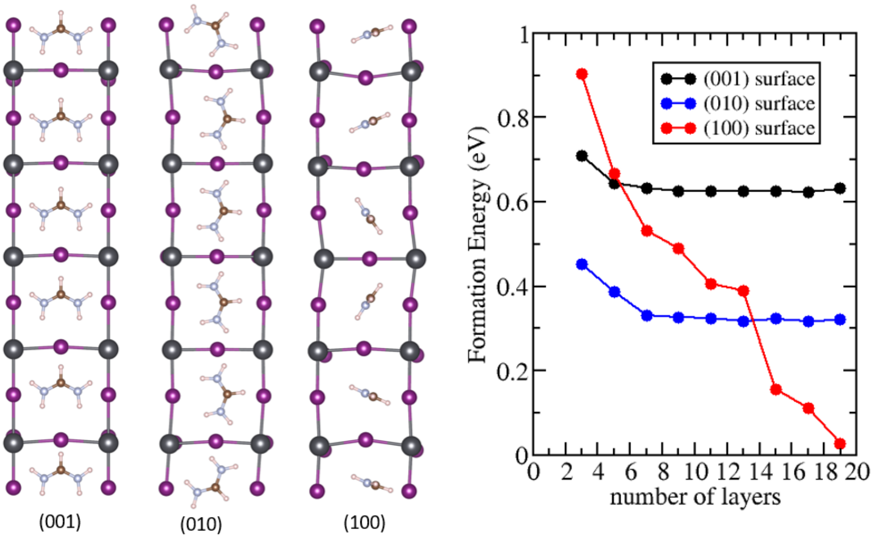

PbI$_2$ termination

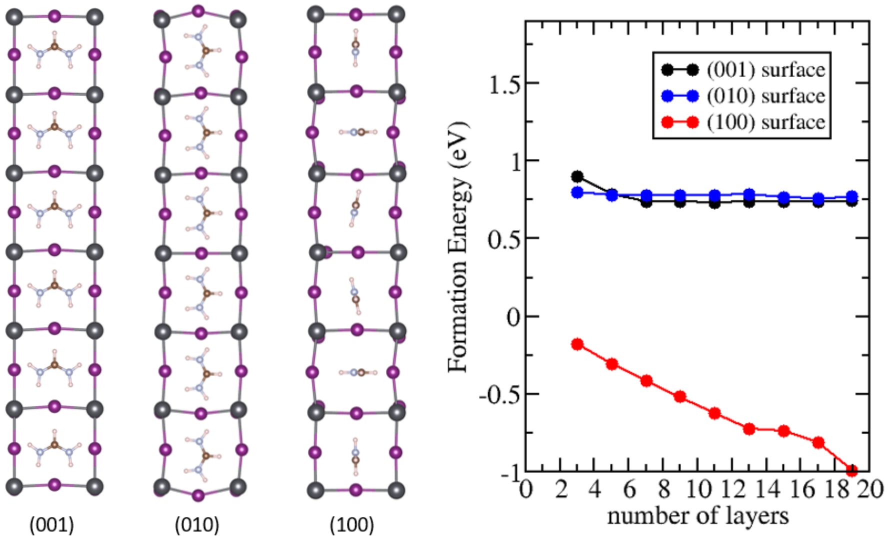

FIGURE 3.8: Energy of formation of slab, (001) (010) (100) with FAI and PbI$_2$ termination against the thickness of the slab.

plane of the perovskite cage, and hence is only slightly shifted within this plane in the course of relaxation. However, in the third case, that of the (100) surface, there was neither physical justification nor technical possibility to keep the plane of the molecule parallel to the slab surface when going from layer to layer into the depth. And further on, the resulting big variations in the molecule's orientation from layer to layer, and consequently in the molecule's placement within the cage formed by PbI units led to considerable variations of the total energy, to the extent that the latter, taken as a function of the slab thickness, did not converge, up to the maximal number of layers in the slab we considered. On removing the symmetry constraints, the FA molecule is free to rotate as suggested in Maheshwari et al. [2019]. For the (100) surface, more study is needed to understand the issue.

### 3.3.3 Perfect $CsPbX_3$ surface for adsorption

Once the issue of the necessary thickness of the slab is settled for $CsPbX_3$ surfaces, we recall that the essential priority of the present study is the simulation of molecules adsorbed on the surface. As this should be compatible with periodic boundary conditions within the surface plane, the choice has to be done of the lateral size and shape of the supercell that would keep the adsorbed molecules (one per supercell) far enough from each other. In principle, the study of an adsorbed molecule would be best done on supercells of infinitely large lateral size, employing, e.g., a Green's function technique in order to treat a local perturbation over an infinite system. In practical terms, however, one uses periodic boundary conditions, and the lateral supercell size is subject to tests, performed on supercells of gradually increasing size: the properties which are of interest, such as the adsorption energy, must be well converged (to the accuracy which is meaningful) as a function of the supercell size before the latter becomes prohibitively large. Supercells of different size were generated by choosing gradually increasing in-plane translation vectors, ranging from $(\sqrt{2}\times\sqrt{2})$ to $(4\times4)$. To estimate the appropriate size of the **k**-points mesh, adsorption energy (discussed later) of the surface is calculated against varying **k**-points for each surface, and the total energy stabilises to 0.0001 eV with the **k**-points mesh of $6\times6$.

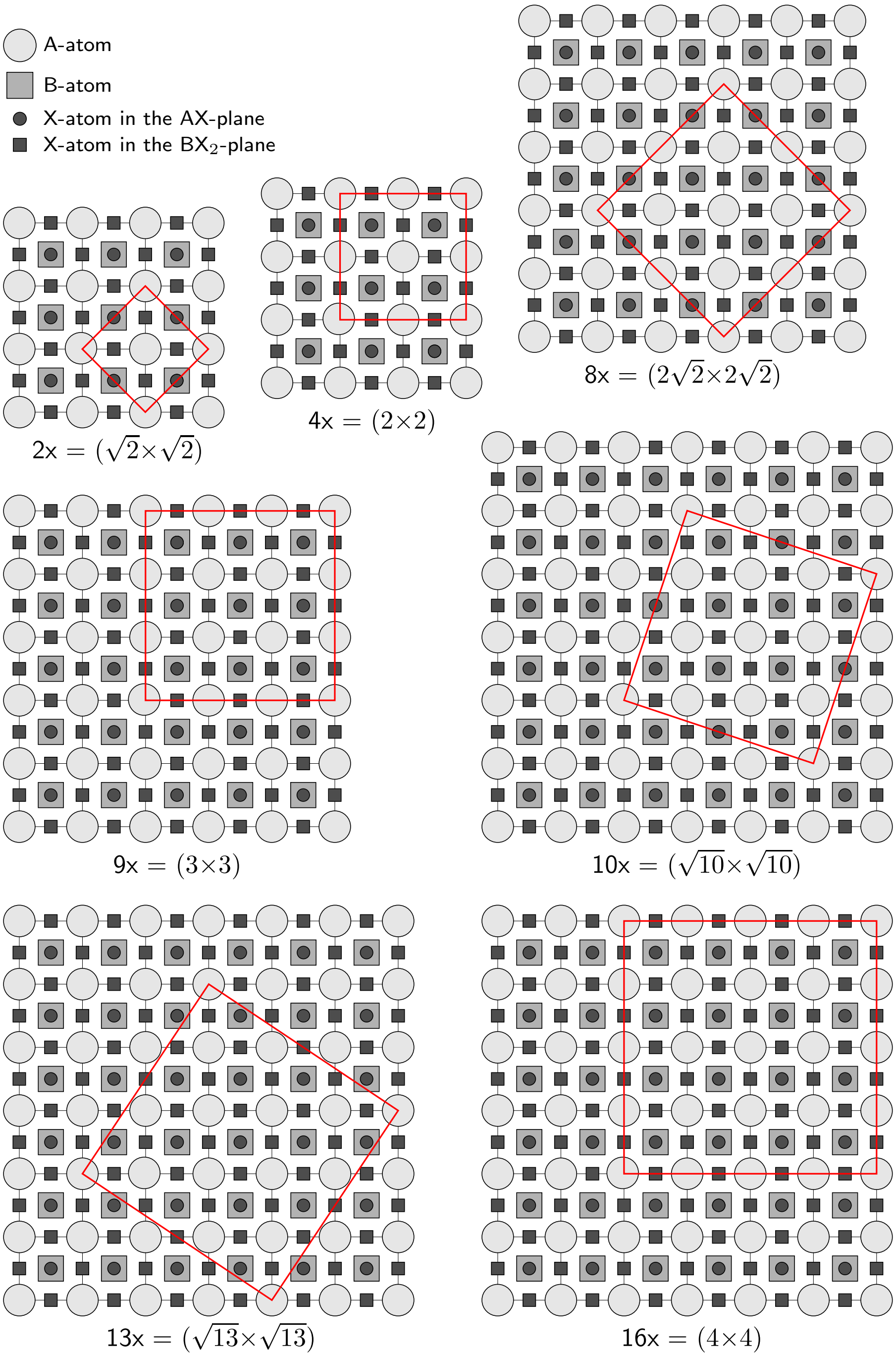

FIGURE 3.9: Supercells of different sizes with the A-atoms at the origin.

### Reconstruction in CsPbX$_3$ perovskite

To analyze the free surface, the idea is to systematically increase the size: $(\sqrt{2}\times\sqrt{2})$, $(2\times2)$, $(2\sqrt{2}\times2\sqrt{2})$, $(3\times3)$, $(4\times4)$ like the "straight square" cells with 16 operations of symmetry and "twisted" cells such as $(\sqrt{10}\times\sqrt{10})$ and $(\sqrt{13}\times\sqrt{13})$ with 8 operations of symmetry. The cutting of various sizes of the supercell are shown in the figure 3.9.

As discussed before, bulk $CsPbX_3$ type perovskites possess instabilities at the high symmetry points in the Brillouin zone. So, for the surface, following an initial relaxation of each supercell within its respective symmetry constraints, the calculation of $\Gamma$ phonons (of the respective supercell, which mapped different $\mathbf{q}$ values of the underlying "perfect" surface Brillouin zone) were done.

The symmetry constraints for the structure relaxation were correspondingly reduced, and the structure optimisation was redone to enable displacements to resolve the instability. From Figure 3.10, a noticeable relaxation, including the in-plane displacement, evolved already at clean surfaces, as a result of lowering of symmetry, after which the lattice parameter is no longer fixed. In the present study, the symmetry group corresponding to the orthorhombic structure is considered for re-optimisation,

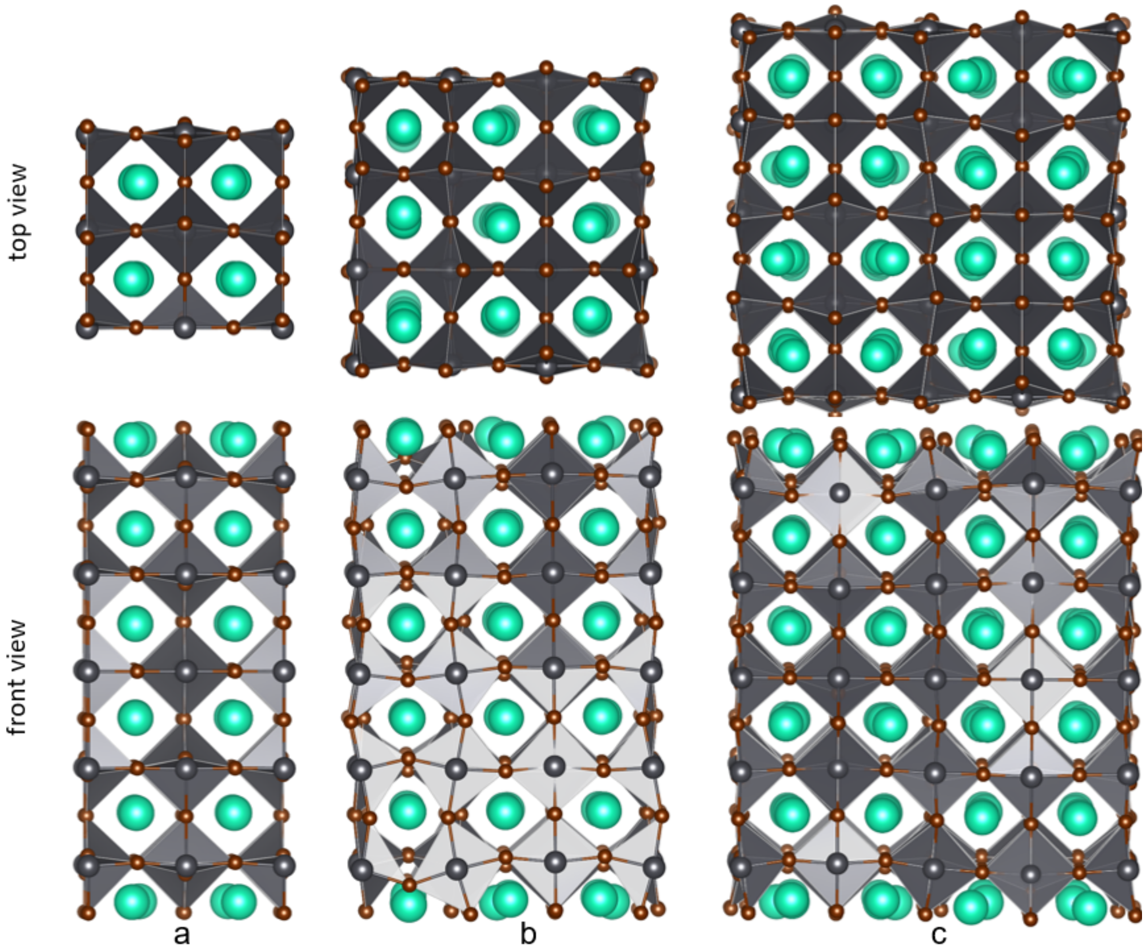

FIGURE 3.10: Top view (above) and front view (below) on the reconstructed slabs of $CsPbBr_3$ for $2 \times 2$ (a), $3 \times 3$ (b) and $4 \times 4$ (c) supercells with CsBr termination slab.

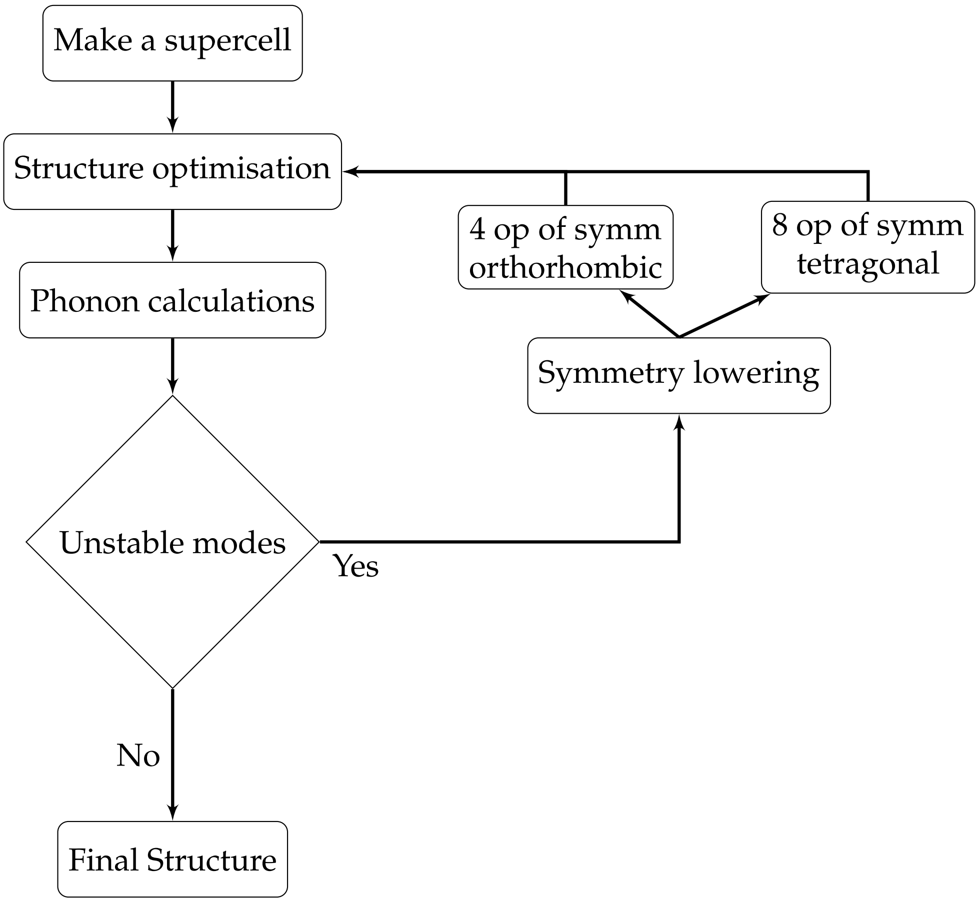

FIGURE 3.11: Structure optimisation scheme followed to determine the stable structure of the supercells (see text for details).

which is more stable than the tetragonal structure. The flow chart of the optimisation scheme followed in this work is illustrated in Figure 3.11.

The surface structures (with reduced symmetry) which emerge from the clean surface relaxation, the top of the surface appears to be "reconstructed" and the local environment within the upper layer of the slab is modified. Different sizes of the supercells showed different "reconstruction" patterns (see Figure 3.10). (3×3) reconstructed surface of $CsPbX_3$ is sufficient to provide distance between adsorbed molecules and their periodic images and hence chosen to study reconstruction followed by adsorption of molecules (discussed in Chapter 4) in the present work.

The Figure 3.12 and Table 3.4 summarize the main characteristics of the reconstructed surfaces for both terminations.

The modifications of the in-plane lattice parameters are about 0.2% and 1% with respect to those in the 1×1 tetragonal slabs for $CsPb(Cl/Br)_3$ and $CsPbI_3$, respectively;

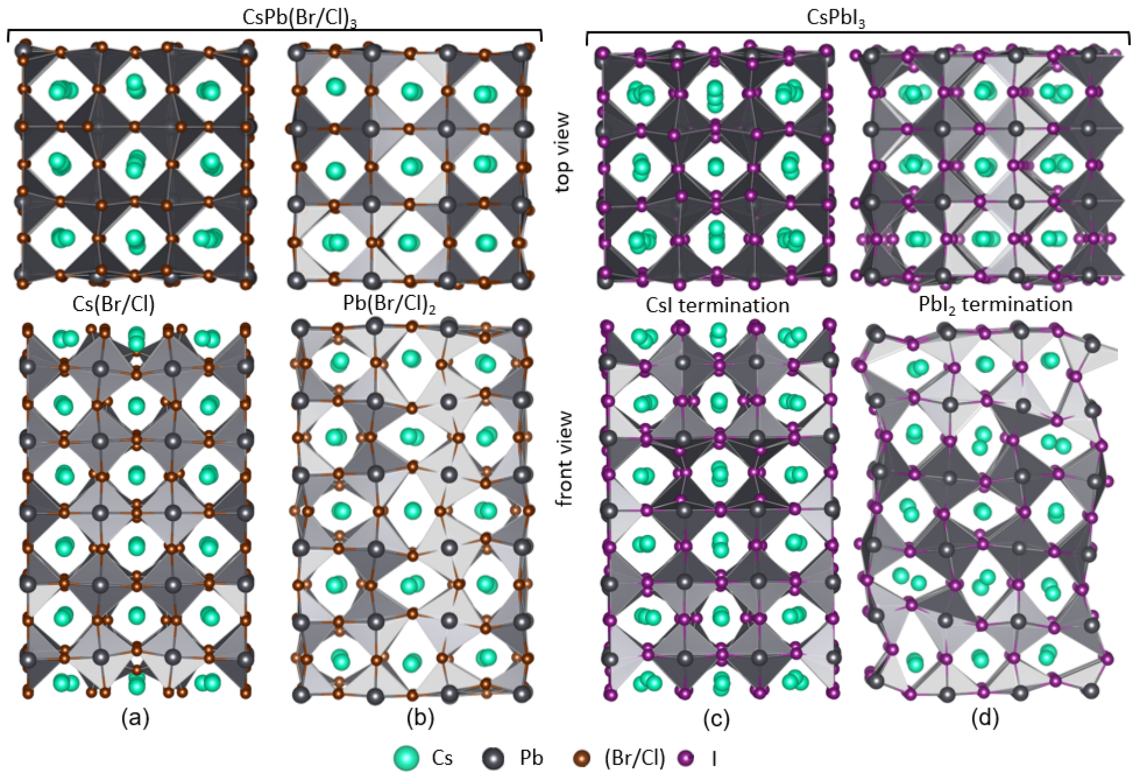

FIGURE 3.12: Top view (above) and front view (below) on the reconstructed slabs of CsPb(Cl/Br)$_3$ (a, b) and of CsPbI$_3$ (c,d). The slab terminations are CsX (a, c) and PbX$_2$ (b, d).

the $[(b/a)_{\mathrm{CsX}}, (b/a)_{\mathrm{PbX_2}}]$ ratii are $[1.005,\ 1.000]$, $[1.002,\ 1.012]$ and $[1.012,\ 1.020]$ for CsPbCl$_3$, CsPbBr$_3$ and CsPbI$_3$, correspondingly.

Two types of deformation can characterise the atomic structure:

(1) The variations of interlayer distances;

(2) The in-plane displacements of atoms and the warpings of atomic planes linked to the tiltings and deformations of vertices-coupled PbX$_6$ octahedra (see Figure 3.12, side view of the relaxed slabs). These atomic relaxations gave rise to variation in layer thickness, referred to as the layer width.

The consecutive interlayer distances between the top and the median planes of the slab along with the width of each layer are listed in Table 3.4 and illustrated by the Figure 3.14. Whatever the surface, the range of the different atomic relaxations increases with the increasing lattice parameter from CsPbCl$_3$, CsPbBr$_3$ to CsPbI$_3$ due to the steric effect.

In what concerns the evolution of interlayer distances into the depth, the relaxation was accompanied by a considerable warping of CsX and $PbX_2$ atomic layers within the supercells. The values in the depth of the slab are gradually approaching those of perfect bulk perovskites. Whatever the compounds and termination of the surfaces, the perturbations of the interlayer distance (concerning the perovskite structure, see Table 3.4) are most prominent for the first layer (around 15%) and are reduced towards the interior of the slab to come down to a variation of 0.5% by an alternate increase and decrease in the interlayer distance.

TABLE 3.4: Interlayer distances ("inter" in Å) and widths of (warped) atomic layers (width in Å) in relaxed slabs of $CsPbX_3$ for both CsX and $PbX_2$ terminations (see Figure A.3). For perovskite structure, the interlayer distance is half of the lattice parameter corresponding to 3.09, 2.94 and 2.82 Å for $CsPbI_3$, $CsPbBr_3$ and $CsPbCl_3$, respectively

| | | $CsPbI_3$ | | $CsPbBr_3$ | | $CsPbCl_3$ | |
|---|---|---|---|---|---|---|---|
| | layer | width | inter | width | inter | width | inter |
| CsX termination | | | | | | | |
| (top) | CsX | 1.30 | | 0.99 | | 0.84 | |
| | | | 2.72 | | 2.57 | | 2.49 |
| | $PbX_2$ | 2.04 | | 1.72 | | 1.53 | |
| | | | 3.20 | | 3.17 | | 3.03 |
| | CsX | 0.37 | | 0.14 | | 0.13 | |
| | | | 2.88 | | 2.74 | | 2.66 |
| | $PbX_2$ | 1.77 | | 0.92 | | 0.90 | |
| | | | 3.11 | | 2.91 | | 2.82 |
| | CsX | 0.85 | | 0.25 | | 0.21 | |
| | | | 2.99 | | 2.90 | | 2.80 |
| (median) | $PbX_2$ | 1.63 | | 1.25 | | 0.90 | |
| $PbX_2$ termination | | | | | | | |
| (top) | $PbX_2$ | 1.72 | | 1.14 | | 0.57 | |
| | | | 2.63 | | 2.57 | | 2.47 |
| | CsX | 1.45 | | 0.53 | | 0.26 | |
| | | | 3.27 | | 3.05 | | 2.95 |
| | $PbX_2$ | 1.75 | | 1.49 | | 0.74 | |
| | | | 2.97 | | 2.84 | | 2.69 |
| | CsX | 1.13 | | 0.34 | | 0.07 | |
| | | | 3.07 | | 2.93 | | 2.86 |
| | $PbX_2$ | 1.92 | | 1.30 | | 1.13 | |
| | | | 3.08 | | 2.91 | | 2.80 |
| (median) | CsX | 0.91 | | 0.62 | | 0.00 | |

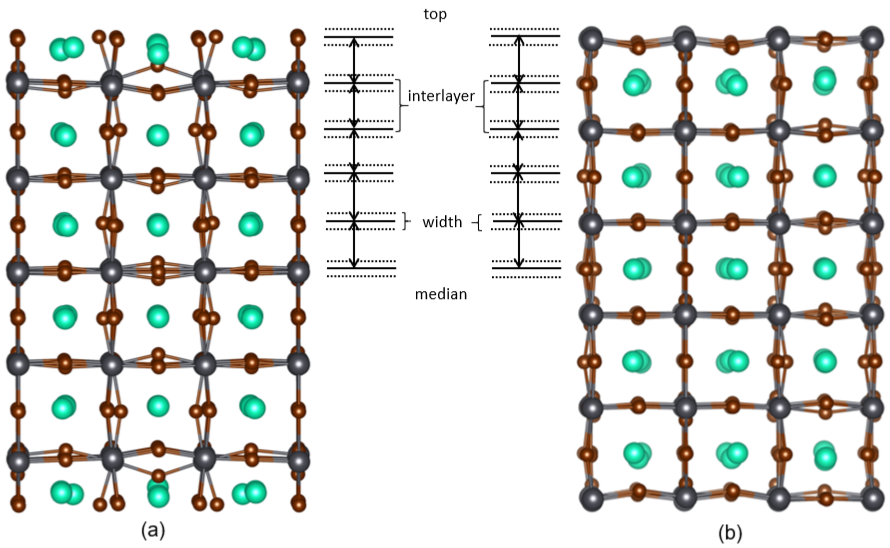

FIGURE 3.13: Schematic view of the interlayer and the range of atomic relaxations around the interlayer (width), as defined in Table 3.4, for the CsX termination (a) and the $PbX_2$ termination (b).

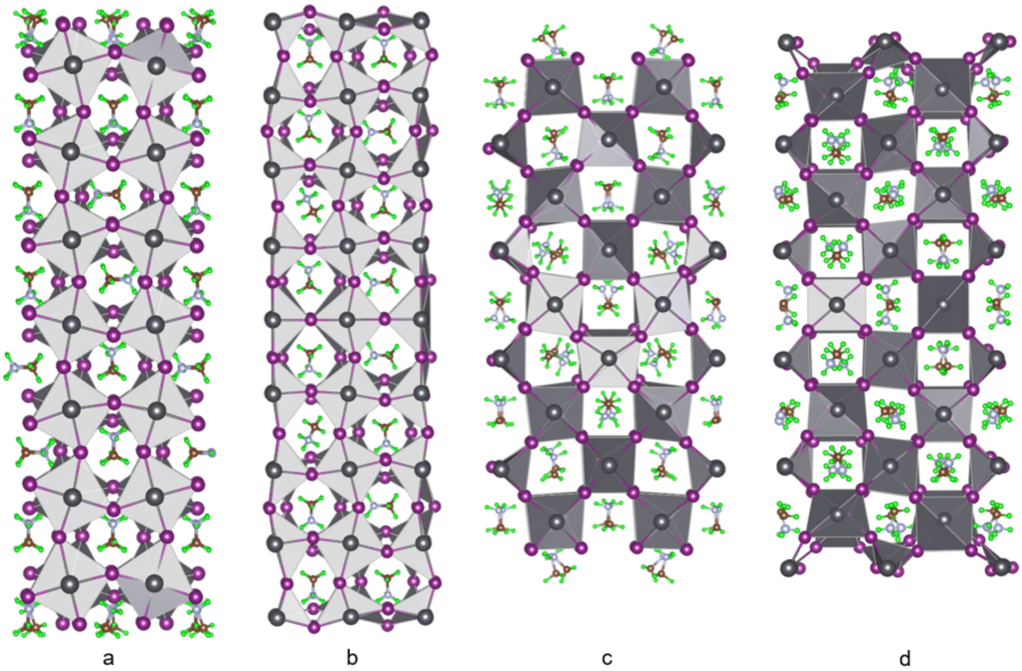

FIGURE 3.14: Front view of the reconstructed MAPI slab with MAI (a, c) and $PbI_2$ (b, d) termination for (001) (a, b) and (110) (c, d) surfaces. Data of MAPI surfaces adapted from Baranek [2019].

Apart from this, the relaxation pattern in the interior of the slabs reveals the tiltings and deformations of $PbX_6$ octahedra (see Figure 3.12); as the octahedra are corner-coupled, their tiltings propagate in “waves”. In the periodic directions, due to the choice of the 3×3 supercell, these "waves" are artificially confined, whereas, throughout the slab, they can freely evolve. Consequently, the variations of thickness of the $PbX_2$ layers are more potent than for the CsX layers, whatever the compounds and the termination. It turns out that the surfaces with $PbX_2$ and CsX terminations exhibit two different types of reconstruction.

### 3.3.4 MAPI surfaces for adsorption

(001) and (110) surfaces with MAI, and $PbI_2$ terminations are simulated using the bulk structures. The slabs thus cut out of the orthorhombic phase possess 16 operations of symmetry. The in-plane lateral sizes of the supercells, in terms of the bulk unit cells, are $(2{\times}2)$ [Baranek, 2019]. The in-plane dimensions of the (2x2) supercell of MAPI are very close to those of the (3×3) supercell of $CsPbX_3$. A small in-plane multiplication factor in the construction of slab supercells puts limitations on the tilting patterns which may come about on the surfaces. Namely, these patterns ought to be commensurate with the surface supercell. A more sophisticated reconstructions on the surface, like those discussed above in relation with $CsPbX_3$ perovskites, did not occur therefore in calculations with MAPI.

The interlayer distances for MAPI (001) and (110) surfaces for both MAI and $PbI_2$ terminations are shown in the table 3.5.

In order to express interlayer distances, we need to refer to the sequence of $PbX_2$ / (cation)-X layers. In $CsPbX_3$, the $z$-position of a CsX layer was expressed as the average $z$ coordinate of all atoms belonging to it. In the case of MAPI, however, it is problematic to pinpoint the "position" of the large enough molecule, so it was neglected, and only the $z$ coordinates of I atoms in this layer were taken into account to identify this layer's position. The variation in the interlayer distance for the (001) surface of MAPI is similar to that of its $CsPbX_3$ counterpart. The interlayer distance is larger for MAPI (001) surface from the top to the centre of the surface as compared to that of the $CsPbX_3$ surface because of relatively larger lattice parameter of MAPI. For (110) surface, the change in interlayer distance varies as around 16% for the top and, gradually approaching the slab's interior, the change in the interlayer distance goes down to 8%.

TABLE 3.5: Interlayer distances ("inter" in Å) and widths of (warped) atomic layers (width in Å) in relaxed slabs of MAPI for both MAI and $PbI_2$ terminations (see Figure A.3). Interlayer distance is calculated similar to Figure A.3. See text for details. For perovskite structure, the interlayer distance is half of the lattice parameter corresponding to 3.18 Å.

| | | (001) | | (110) | |
|---|---|---|---|---|---|
| | layer | width | inter | width | inter |
| CsX termination | | | | | |
| (top) | I | 0.10 | | 0.14 | |
| | | | 2.92 | | 2.49 |
| | $PbI_2$ | 1.75 | | 0.52 | |
| | | | 3.44 | | 2.09 |
| | I | 0.09 | | 0.41 | |
| | | | 2.92 | | 2.46 |
| | $PbI_2$ | 1.88 | | 0.80 | |
| | | | 3.32 | | 2.12 |
| | I | 0.09 | | 0.54 | |
| | | | 0.06 | | 2.39 |
| | $PbI_2$ | 2.05 | | 1.07 | |
| | | | 3.09 | | 2.13 |
| | I | 0.07 | | 0.61 | |
| | | | 3.25 | | 2.34 |
| | $PbI_2$ | 1.72 | | 0.50 | |
| $PbI_2$ termination | | | | | |
| (top) | $PbI_2$ | 1.57 | | 0.33 | |
| | | | 2.92 | | 2.06 |
| | I | 0.14 | | 1.23 | |
| | | | 3.32 | | 2.09 |
| | $PbI_2$ | 1.70 | | 0.95 | |
| | | | 3.01 | | 2.26 |
| | I | 0.07 | | 0.72 | |
| | | | 3.30 | | 2.36 |
| | $PbI_2$ | 1.82 | | 0.82 | |
| | | | 2.95 | | 2.06 |
| | I | 0.05 | | 0.57 | |
| | | | 3.35 | | 2.32 |
| | $PbI_2$ | 1.66 | | 0.97 | |
| | | | 3.01 | | 2.19 |
| median | I | 0.08 | | 0.63 | |

## 3.4 Vacancy defects on $CsPbX_3$ surface

As discussed in Chapter 1, perovskites are prone to form point defects, e.g. vacancies or interstitials. In the present study, only the vacancy defects are focused on. In organic halide perovskites, halide ion vacancies are more likely to be formed in comparison to the cation vacancies [Eames et al., 2015]. The halogen vacancies are attracted by grain boundaries and the surfaces. So, these point defects are most likely to be present as the local imperfections at the surface of perovskites [Lei et al., 2021]. The halogen vacancies are known to exist either in neutral, or in charged state.

Upon removing an atom, the vacancy may remain neutral or acquire a charge due to redistribution of electron density within an extensive system of the slab. From the point of view of calculation, the neutral and charged vacancies may correspond to distinct metastable situations; into each of them the system can be intentionally "forced" and then left to evolve towards a possible stabilisation in the course of relaxation. As the periodic crystal as a whole, and the supercell under study in particular, cannot but remain neutral (for physical and technical reasons), the difference between"neutral" and "charged" scenarios for the vacancy amounts to specifying, in the latter case, the charge compensation mechanism – either on a short range (possibly, including another charge-compensation defect), or on a long range, whereby no specific microscopic compensation is explicitly built in, but the charge compensation is assured by adjusting the background charge over the supercell. In this work, charged and neutral halide vacancies are modelled on the surfaces of inorganic halide perovskites. In the framework of the Gaussian-type basis sets, the modelling of charged or neutral defects is relatively easy to implement : As the starting point of the SCF cycles, the electronic re-partition is given for each atomic orbital; then, for each atom, it is possible to choose between their fundamental neutral configuration or their ionic configuration. For instance, for $CsPbX_3$, the neutral system can be initially prepared in (at least) two ways, either with $Cs^0$, $Pb^0$ and $X^0$, or with $Cs^+$, $Pb^{2+}$ and $I^-$ for the neutral and ionic configurations, respectively.

The simulation of a charged vacancy, say following a removal of $I^-$, imposes, in technical terms, adding a uniform (negative) charge density in the background. In

CRYSTAL17, this does not bring about any modification in the simulation, as the Ewald technique [Kolafa and Perram, 1992] is adopted for the treatment of long-range Coulomb terms, see Dovesi et al. [2017] for details) to ensure the charge neutrality. For practical reasons, namely for avoiding the convergence issues, the halide vacancies expected to be charged were created in the simulations by pairs at opposite surfaces of a slab. As mentioned before, the CsX terminated structure has 243 atoms, while the $PbX_2$ terminated structure has 252 atoms. Upon creating a charged vacancy, the surface has 241 and 250 atoms for CsX and $PbX_2$ terminated structures, respectively. The formation of charge vacancy can be described by the equation:

$$\mathrm{CsPbX_3} \longrightarrow \mathrm{CsPbX_2}^{+} + \mathrm{X}^{-} \quad . \tag{3.2}$$

For the neutral anion defect, the starting electronic re-partition for the perfect surface is $Cs^0$, $Pb^0$ and $I^0$. So, when the $I^0$ is removed, the system stays neutral. The basis set and the electrons of one Iodine have been removed. It is essential to perform this calculation in spin-polarised mode in order to anticipate and correctly describe the situation in which an unpaired electron (present after a halogen atom with its odd number of electrons is removed) would reside on one of the neighbouring Pb atoms. Such localisation of spin on a Pb atom indeed occurs and is visible in spin density maps that are shown in Figure 3.15. Upon creating a neutral vacancy, the number of atoms in CsX and $PbX_2$ terminated surfaces are 242 and 251, respectively. The formation of neutral vacancy can be described by the equation:

$$\mathrm{CsPbX_3} \longrightarrow \mathrm{CsPb^{\uparrow}X_2} + \mathrm{X} \quad . \tag{3.3}$$

All the vacancies are created on the already reconstructed surface. Figure 3.16 shows the charge density maps of top of CsX and $PbX_2$ terminated structures. The red colour there indicates electron-deficient region and blue colour indicates the electron-rich regions. The charged vacancy has a pile-up of positive charge around the white spot (indicating halide vacancy), which is much less pronounced in the case of a neutral vacancy.

The formation energy for charged vacancy is given by the following expression:

$$E_{\text{vac}} = E_{\text{slab}} - E_{\text{slab with defect}} - E_{\text{mol X}_2} \pm q \times E_f \quad , \tag{3.4}$$

where $q$=+2 for charged vacancy (two positive charged vacancies, added at both sides of the slab). $E_f$ is the Fermi energy. The formation energy so obtained is for two charged vacancies and is further divided by 2 to obtain the formation energy of one charged vacancy.

The formation energy for neutral vacancy is described as:

$$E_{\text{vac}} = E_{\text{slab}} - E_{\text{slab with defect}} - n \times E_{\text{mol X}_2} \quad , \tag{3.5}$$

where $n$ = 1/2 as only one atom is removed.

Table 3.6 shows the vacancy formation energy for $CsPbX_3$ surface for CsX and $PbX_2$ terminated structures. Charged vacancies are more likely to be formed on whatever be the surface and surface termination. $CsPbI_3$ surface shows the lowest vacancy formation energy for both types of termination. While for the case of neutral vacancy, the $CsPbCl_3$ surface shows the lowest vacancy formation energy (for both types of termination) that may be related to chlorine being more ionic than the heavier halogens.

With the introduction of the charged or neutral vacancy on the surface, the relaxation pattern of the surface did not show any drastic change for all three compounds.

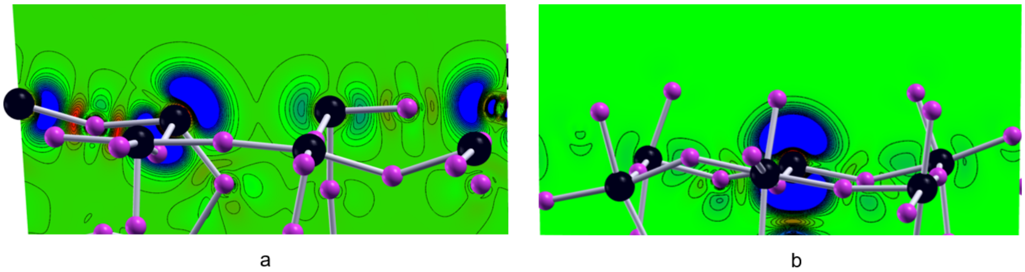

FIGURE 3.15: [100] view of alpha-spin density associated to the unpaired electron on Pb atom at the uppermost layer (for $PbX_2$ termination, a) and the second layer from the uppermost layer (for CsX termination, b) of the $CsPbI_3$ surfaces. For sake of clarity, Cs atoms are hidden. Pb atoms are in black. The separation between contiguous isodensity curves corresponds to 0.001 e/Bohr$^3$ in the spin maps; curves corresponding to absolute values larger than 0.02 spin-density e/Bohr$^3$, are omitted.

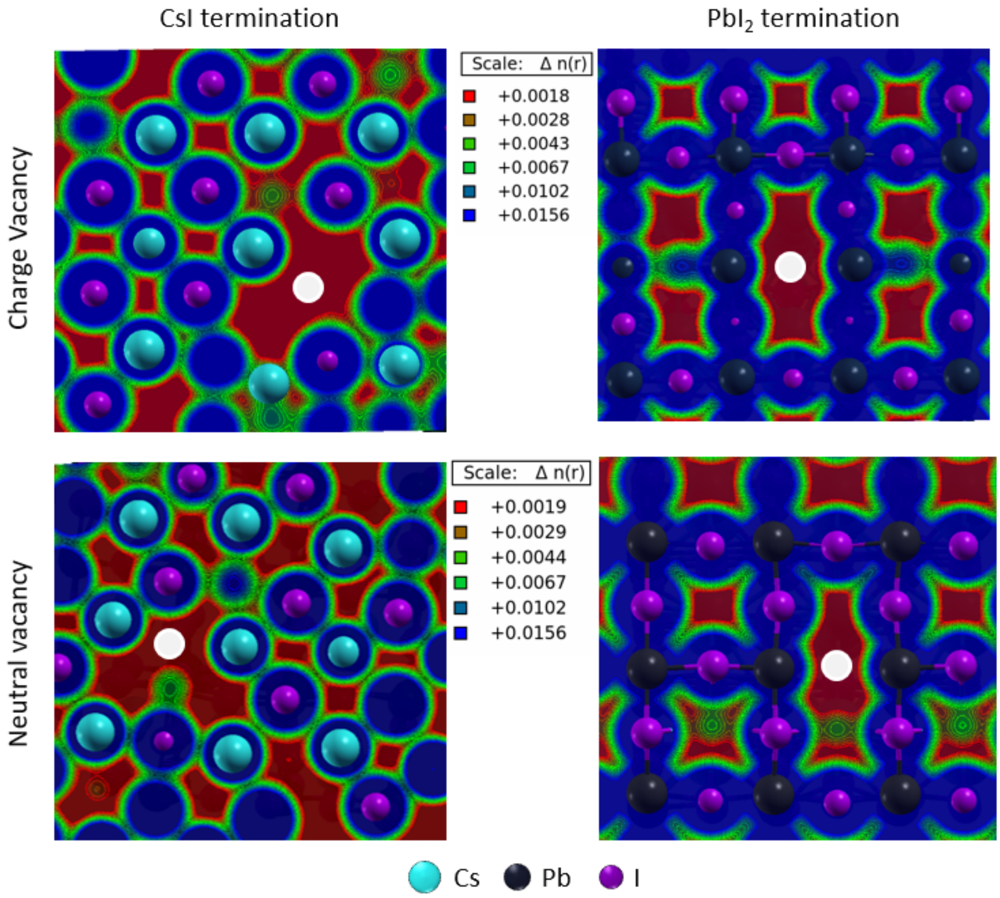

FIGURE 3.16: Charge density maps of top of the surface with charged and neutral vacancies on CsX and $PbX_2$ terminated structures. Halogen vacancy is marked with white circle.

TABLE 3.6: Vacancy formation energy (in eV) for charged and neutral vacancies calculated for CsX and $PbX_2$ terminated structures for $CsPbX_3$ (X=Cl, Br, I) compounds.

| X | Charged vacancy | Neutral Vacancy |
|---|---|---|
| CsX termination | | |
| Cl, V-CsCl | 3.64 | −4.31 |
| Br, V-CsBr | 3.52 | −3.96 |
| I, V-CsI | 3.44 | −3.50 |
| $PbI_2$ termination | | |
| Cl, V-$PbCl_2$ | 3.16 | −3.80 |
| Br, V-$PbBr_2$ | 3.01 | −3.27 |
| I, V-$PbI_2$ | 2.85 | −2.96 |

The relaxation pattern remains similar to that of the perfect surface. The tables of interlayer relaxations are included in the Appendices A.6 and A.7.

In this chapter, we modelled the bulk and surfaces of organic and inorganic halide perovskites with our optimised hybrid functional approach. For the inorganic halide perovskite, halide vacancy defects were introduced. The surfaces modelled in this chapter are further used to carry out adsorption of molecules which is part of the coming chapters.

# Chapter 4

# Adsorption on inorganic halide perovskites

This chapter addresses the issue of *degradation* of halide perovskites under the influence of molecules (water, oxygen, carbon dioxide and carbon monoxide) adsorbed at the surface. The role of water is studied only on the $CsPbX_3$ surface with defects, as the issue of water on the perfect surface is being specially studied by Baranek [2019]. The adsorption of molecules should simulate the effect of ambient conditions to which the perovskites are unusually exposed, and the effect of degradation of perovskites can be studied under these conditions.

The adsorption is simulated in the calculations by placing one molecule per supercell (of sufficient lateral size) over a clean surface represented by a slab, which probably underwent a relaxation. Important points to discuss in this relation are the supercell size (the stability and convergence of results in the course of gradually increasing the latter), the choice of initial docking position of the molecule, and the initial orientation of the molecule. In the ideal case, concerning two latter factors, reasonable good statistics have to be collected in order to be able to make reliable conclusions. The adsorption energy is calculated as:

$$E_{\mathrm{ads}} = E_{\mathrm{molecule/surface}} - \left[E_{\mathrm{surface}} + E_{\mathrm{molecule}}\right] \quad . \tag{4.1}$$

## 4.1 Understanding the issues of convergence of adsorption energy

To study the issue of convergence, the logical way to start is to freeze the atoms of the surface and place the molecule at different heights over the surface in a series of single-point calculations to obtain the potential energy (PE) curve. Such PE curve (see Figure 4.1) did not show significant change depending on lateral size of the supercell.

However, if unconstrained relaxation is allowed throughout the supercell for each fixed position of the molecule from the surface, then the PE curves become much less smooth and, in fact, wildly fluctuating. Therefore, some systematics needs to be established so that the effect of the supercell size be carefully controlled. The issues responsible for fluctuating results are different symmetries and different relaxation patterns compatible with different supercells. The instructive way is to "release" the atoms for

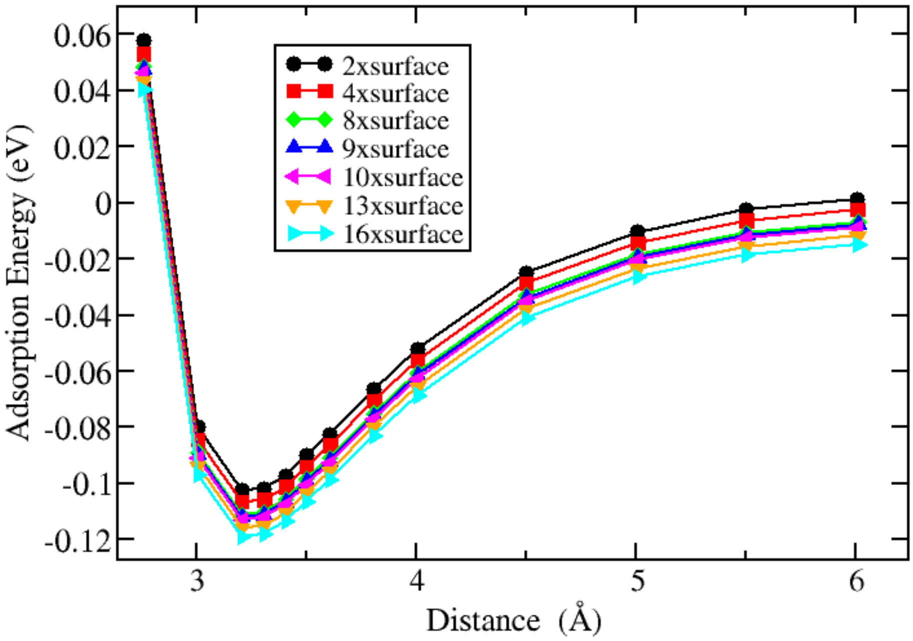

FIGURE 4.1: Adsorption energy of $CO_2$ molecule placed on top of Cs over $CsPbBr_3$ surface with CsBr termination, plotted against distance of $CO_2$ molecule from the top of the surface.

relaxation around the impurity (e.g., an adsorbed molecule) shell by shell, from the closest to more distant ones. Obviously, the number of "relaxable" more distant atoms increase with supercell size.

In the following, a sequence of lateral supercells of gradually increasing size is considered for CsX terminated structures. In fact, the molecule is placed over the A atom, i.e. Cs in this case. The supercells considered assume that the (quadratic, in two dimensions ) point group symmetry is preserved around the sites in question. These situations are not exclusive since the molecule might be adsorbed not necessarily atop the A site; it can be rotated or tilted to the surface, effectively destroying any nominal symmetry. However, we consider the idealised symmetric cases useful for studying size convergence issues.

Figure 3.9 depicts a sequence of supercells, labelled from $2\times$ to $16\times$, according to the replication of the original cubic perovskite cell in the $(x, y)$ plane. Table 4.1 below gives explicit coordinates of the atoms in the AX planes of the supercells $1\times$ through $8\times$. The sequences can be straightforwardly continued towards larger supercells, resulting in longer tables and an increased number of "free" atoms. The tables can be verified by checking that for a $N\times$ supercell; one finds $N$ (A, B, $\mathrm{X_A}$) atoms and $2N$ $\mathrm{X_B}$ atoms. The $x$- and $y$-coordinates in the Table are subject to relaxation and are, in principle, different from atom to atom and between different planes in the slab. In the Figure 4.2, the first shell is the atoms described in the Table, while for the second shell, the atoms released are lying in the layers exactly underneath the atoms of the top layer, and it continues until the cuboid formed by Pb atoms is released altogether.

The systematic approach helps to achieve controllable convergence of the size-dependent properties are described as follows:
The "shells of neighbours" for the adsorbed molecule (i.e., atoms situated at a given distance from the $[001]$ axis pinpointing the adsorbed molecule) will be released for relaxation one by one. For example, the four $X_\mathrm{B}$ atoms, situated at the lateral distance $\frac{1}{2}$ from the A atom, are the only relaxable atoms in the $2\times$ supercell (see Table 4.1), but they are merely the most inner ones among a longer list of neighbours in $4\times$, $8\times$ etc. supercells. In these larger supercells, the more distant neighbours than these $X_\mathrm{B}$ at the $\frac{1}{2}$ lateral distance will be fixed, and the trends (e.g., adsorption energy) are analysed,

TABLE 4.1: Atom positions in the supercells organized around the A atom at $(0\,0)$, in terms of nominal in-plane perovskite lattice parameter. $z=0$ and $z=\frac{1}{2}$ mark coordinates within two consecutive planes, $AX_A$ and $B(X_B)_2$, repeated into the depth by steps $z=1$. The last column shows the lateral distance of each atom to the origin (irrespective of the $z$-value) for the non relaxed lattice, so that the "relaxable" atoms are ordered as their distances from $(0,0)$ increase.

| cell | in-plane translation vectors | atoms fixed | atoms free to relax | ideal lateral distance |
|---|---|---|---|---|
| 1× | $(1\,0)$, $(0\,1)$ | 1A $(0\,0\,0)$<br>$1X_A$ $(\frac{1}{2}\,\frac{1}{2}\,0)$<br>1B $(\frac{1}{2}\,\frac{1}{2}\,\frac{1}{2})$<br>$2X_B$ $(\frac{1}{2}\,0\,\frac{1}{2})$, $(0\,\frac{1}{2}\,\frac{1}{2})$ | none | |
| 2× | $(1\,\bar{1})$, $(1\,1)$ | 1A $(0\,0\,0)$<br>1A $(1\,0\,0)$<br>$2X_A$ $(\frac{1}{2}\,\pm\frac{1}{2}\,0)$<br>2B $(\frac{1}{2}\,\pm\frac{1}{2}\,\frac{1}{2})$ | $4X_B$ $(\pm x\;0\;\frac{1}{2})$, $(0\;\pm x\;\frac{1}{2})$ $[x\approx\frac{1}{2}]$ | $\frac{1}{2}$ |
| 4× | $(2\,0)$, $(0\,2)$ | 1A $(0\,0\,0)$<br>2A $(1\,0\,0),(0\,1\,0)$<br>1A $(1\,1\,0)$ | $4X_B$ $(\pm x\;0\;\frac{1}{2})$, $(0\;\pm x\;\frac{1}{2})$ $[x\approx\frac{1}{2}]$ | $\frac{1}{2}$ |
| | | | 4B $(\pm x\;\pm x\;\frac{1}{2})$ $[x\approx\frac{1}{2}]$ | $\frac{\sqrt{2}}{2}$ |
| | | | $4X_A$ $(\pm x\;\pm x\;0)$ $[x\approx\frac{1}{2}]$ | $\frac{\sqrt{2}}{2}$ |
| | | | $4X_B$ $(1\;\pm x\;\frac{1}{2})$, $(\pm x\;1\;\frac{1}{2})$ $[x\approx\frac{1}{2}]$ | $\frac{\sqrt{5}}{2}$ |
| 8× | $(2\,\bar{2})$, $(2\,2)$ | 1A $(0\,0\,0)$<br>2A $(1\,\pm1\,0)$<br>1A $(2\,0\,0)$ | $4X_B$ $(\pm x\;0\;\frac{1}{2})$, $(0\;\pm x\;\frac{1}{2})$ $[x\approx\frac{1}{2}]$ | $\frac{1}{2}$ |
| | | | 4B $(\pm x\;\pm x\;\frac{1}{2})$ $[x\approx\frac{1}{2}]$ | $\frac{\sqrt{2}}{2}$ |
| | | | $4X_A$ $(\pm x\;\pm x\;0)$ $[x\approx\frac{1}{2}]$ | $\frac{\sqrt{2}}{2}$ |
| | | | 4A $(\pm x\;0\;0)$, $(0\;\pm x\;0)$ $[x\approx 1]$ | 1 |
| | | | $8X_B$ $(\pm x\,\pm y\,\frac{1}{2})$, $(\pm y\,\pm x\,\frac{1}{2})$ $[x{\approx}1, y{\approx}\frac{1}{2}]$ | $\frac{\sqrt{5}}{2}$ |
| | | | $4X_B$ $(\pm x\;0\;\frac{1}{2})$, $(0\;\pm x\;\frac{1}{2})$ $[x\approx\frac{3}{2}]$ | $\frac{3}{2}$ |
| | | | 4B $(2{\pm}x\;\pm x\;\frac{1}{2})$ $[x\approx\frac{1}{2}]$ | $\frac{\sqrt{10}}{2}$ |
| | | | $4X_A$ $(2{\pm}x\;\pm x\;0)$ $[x\approx\frac{1}{2}]$ | $\frac{\sqrt{10}}{2}$ |

depending on the supercell size. Then, the four B neighbours at the lateral distance $\frac{\sqrt{2}}{2}$ will be added, starting from the $4\times$ supercell onward towards larger cells, and so on. The convergence with the supercell size is achieved fast enough. This procedure helps to understand the two issues:

$(i)$ the supercell size necessary to simulate the adsorption of a supposedly isolated molecule in a calculation with periodic boundary conditions,

$(ii)$ the physically important range of perturbations (at the surface and into the depth) induced by the adsorbed molecule at the perovskite surface.

The test also helped to understand the relaxation patterns around the landing point of the molecule; at the same time, one cannot *a priori* exclude long-range tilting deformations, to which perovskite materials are notorious, to develop at the surface. Certain small supercells may be commensurate with such tiltings (e.g., the $4\times$ supercell would permit to accommodate a $SrTiO_3$-like antiferrodistortive deformation) whereas the others not (see fig 3.10). However, in order to accommodate such distortion, the 2-dimensional supercell must have lower symmetry than that of the square lattice. In general, the larger the supercell, the more sophisticated "deformation wave" it can accommodate. However, the fact that the supercell symmetry may differ from one supercell to another, – e.g., the $(010)$ and other mirror planes of $9\times$ in Fig. 3.9 are no more there in $10\times$, – is at the origin of numerical "noise" in an attempt to attain convergence. The situation may somehow resemble a conditionally converging series whose direct summation is, in principle, possible, under imposing some constraints (an example: a direct summation of the Madelung potential over charge-neutral shells of increasing radii).

The adsorption energy of $CO_2$ as calculated while gradually including controlled relaxation within different shells against the increasing supercell size is shown in Figure 4.2. As described above, while following the controlled relaxation, the adsorption energy for supercells with gradually increasing sizes reached convergence with an accuracy of 0.003 eV after 9x surface (3×3). This confirms that the adsorbed molecule does not bring drastic change on top of the surface and into the depth. However, the adsorption energy starts to wiggle when going further down the surface and allowing unconstrained relaxation. The possible reason is the octahedral tilting which the perovskites are well known for [Yang et al., 2017].

The reconstruction on $(001)$ $CsPbX_3$ surfaces occurs so that the CsX terminations yield multiple structurally inequivalent sites for the adsorption of molecules, marked by distinct relaxation patterns around them. On the $PbX_2$ terminated surfaces, on the contrary, the surface reconstruction is much more uniform, so that only one potential

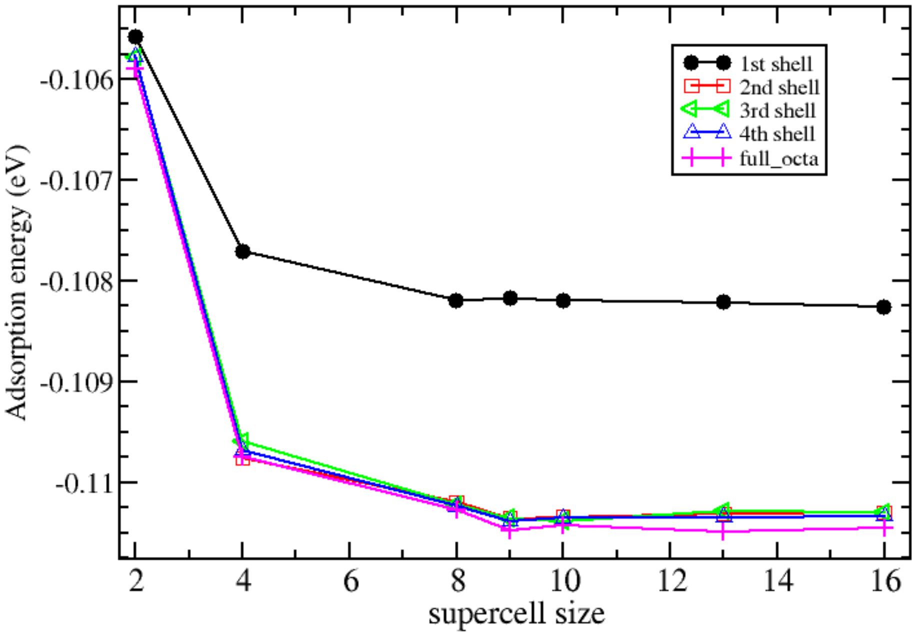

FIGURE 4.2: Adsorption energy of $CO_2$ molecule on $CsPbBr_3$ surface with CsBr termination, plotted against the supercell size. The system is allowed to relax in a controlled manner. See text for details.

site is identified as a distinct one for the adsorption.

## 4.2 Adsorption of molecules on perfect $CsPbX_3$ surfaces

One should have in mind that different sizes of supercell will show different reconstruction patterns because the large size of the supercell can accommodate the in-plane tiltings, which become incommensurate with the imposed periodicity that is generally blocked in a small-size supercell. In the present work, adsorption on $CsPbX_3$ surface is carried out on the 9x surface or (3×3) supercell, sufficient to provide distance between adsorbed molecules in their subsequent study.

The free (001) surfaces of perovskites with different termination and corresponding reconstruction patterns were then inspected in the context of their interaction with $O_2$, CO and $CO_2$ molecules, simulating in this way the modification in the surface under atmospheric conditions. The adsorption sites in the $3\times3$ supercell for both terminations have been distinguished through their numbering, mentioned in the previous chapter and elucidated in Appendix.

In the case of the $PbX_2$ termination slab, since all Pb sites can be considered equivalent, only one has been explored. In contrast, for the CsX termination, the adsorption of the molecules has been systematically investigated, placing the molecules initially over seven different cation sites and two interstitial sites – see Figure A.1 in the Appendix. The molecule has been brought to the surface at one side of the slab only, in a vertical position (the CO has been tried in both orientations). The symmetry constraints have been fully removed at this stage; all the atomic positions and cell parameters have been optimised. The molecules may have drifted over the surface to adjacent positions and/or changed their orientation.

The multitude of trails departing from various starting (docking) positions ended up in just a few markedly distinct final configurations. The scattering of the adsorption energies between different realisations of each given configuration can be hereby considered as being within the "calculation noise". For reference purposes, the detailed data on the adsorption results stemming from different surface sites are given in the Tables A.3 through A.5 of the Appendix. In the following discussion, however, we concentrate on the "final" adsorption configurations.

### 4.2.1 Adsorption on CsX-terminated surfaces

Notwithstanding the diversity of relaxation starting positions and paths, for all the three halides inspected, all the adsorbed molecules get stabilised in a position nearly parallel to the surface, over a "hole" marked by a dashed square in Figure A.1 of Appendix, referred there as `CsX-4` and `CsX-9`. In the process, two of the adsorbed moleculies in the upper CsX layer move slightly apart.

This situation is well seen in the snapshots of the final (relaxed) situation, shown in Figure 4.3 in top-view and front-view projections. Figure 4.4 schematically shows the "docking geometry" of molecules, also, in two projections, indicating the calculated interatomic distances, which are further specified in Table 4.2. One can distinguish between "low" and "high" settings of the adsorbed molecule, markedly different in the distances to the underlying halogen atom of the subsurface layer, indicated as $X_{-1}$ in Figure 4.4 and Table 4.2. Both these settings, marked CsX-l and CsX-h, correspondingly, in Table 4.2, are stable in the sense that they correspond to the total energy minimum. The "low" setting is characterised by a stronger pushing apart the Cs and X atoms in the surface layer, as is evidenced by larger values of Cs–Cs and $X_0$–$X_0$ distances in Table 4.2, as compared to those in the "high" setting.

Table 4.2 reveals the trend which holds for all X halogens: the adsorption energies of $CO_2$ are larger (in absolute value) than CO than $O_2$. As a priori expected, the importance of the $E_{\mathrm{BSSE}}$ correction decreases with the increasing distance between the molecules and its first neighbours at the surfaces, as the data on C illustrate it–$X_{-1}$ and O–$X_{-1}$: $E_{\mathrm{BSSE}}$ is larger for CO than for $CO_2$ than for $O_2$.

In any case, BSSE correction represents a non-negligible contribution to $E_{\mathrm{ads}}$: with BSSE, $E_{\mathrm{ads}}$ becomes more negative, i.e., the interaction of molecules with the surfaces is stronger. For instance, not taking into account the BSSE, CO shows higher interaction with the surfaces than $CO_2$.

Except for CO, the molecules show stronger interaction with the $CsPbI_3$ surfaces than with $CsPbCl_3$ and $CsPbBr_3$. This can be traced to larger atomic relaxation in a material with a larger lattice parameter. The adsorption energies of CO at different surfaces are very close.

It seems that, whatever the molecules and surfaces, the sites with "low" setting are energetically more favourable than the sites with "high" settings.

The CO molecule always "comes to rest" hanging over a "hole" in the CsX layer, on top of a halogen atom from the underlying $PbX_2$ layer ($X_{-1}$, in Figure 4.4a), anchored between two Cs atoms along the molecule's axis (so that respective Cs–C and Cs–O distances are roughly the same, within $\sim 10\%$) and between the $X_0$ atoms (see Figure 4.4a). In the other case of "high" setting, the positioning of the Cs–Cs and the X–X distances in the upper layer remain roughly the same as in an unperturbed crystal, and the molecule places itself at the half of the lattice constant above the CsX layer. By comparison, the "low" setting allows larger atomic relaxations of the anchoring

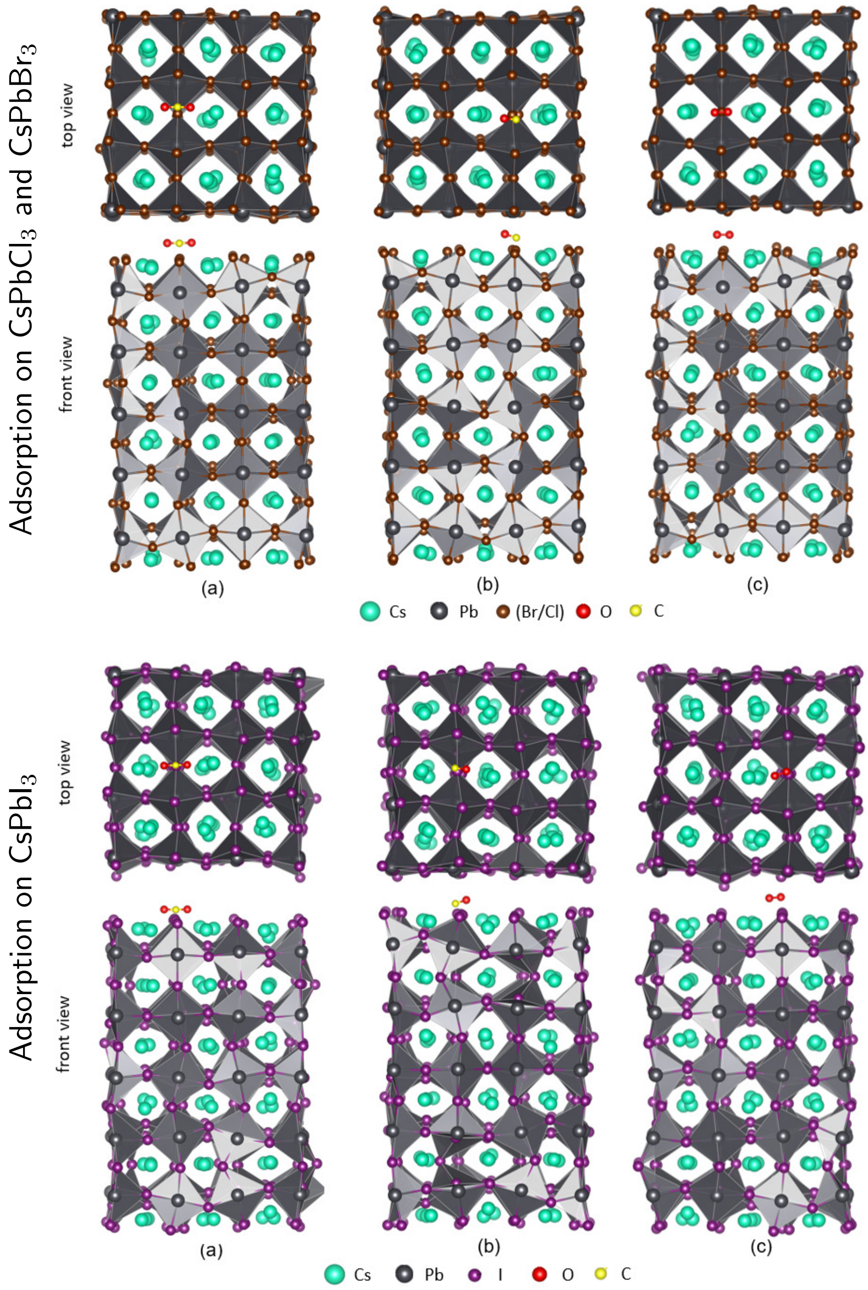

FIGURE 4.3: Representative snapshots in two projections of $CO_2$ (a), CO (b) and $O_2$ (c) molecules adsorbed at the CsX-terminated (001) surfaces of $CsPbX_3$ (X = Cl, Br and I).

Cs–Cs and $X_0 - X_0$ pairs around CO; the molecule then can enter deeper into the surface, coming at a much shorter distance of the $X_{-1}$ halogen atoms of the subsurface layer. This may account for larger adsorption energies in “low” setting configurations, as compared to the “high” setting ones.

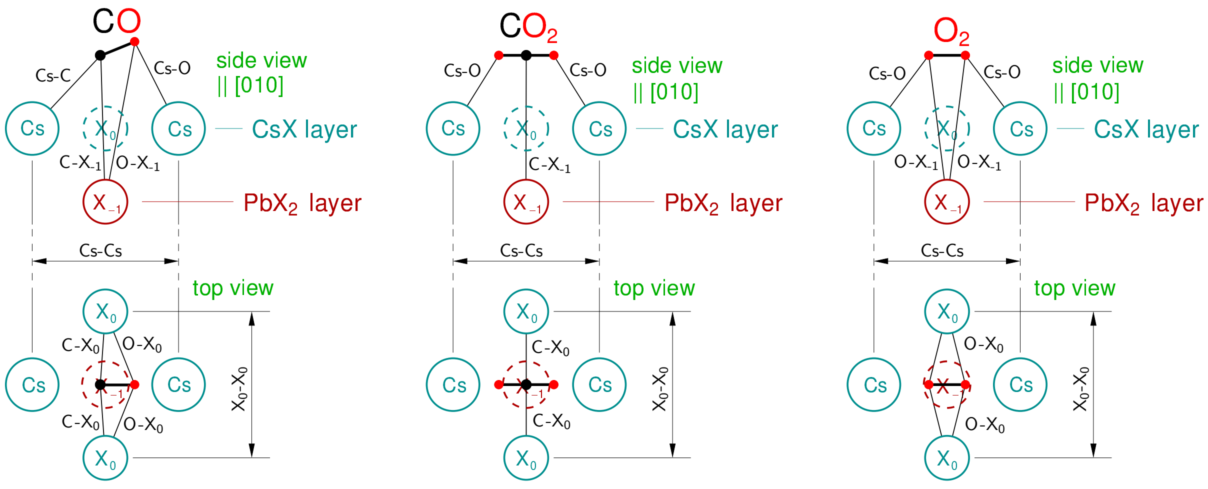

(a) (b) (c)

FIGURE 4.4: Schemes of docking of molecules at CsX surfaces of $CsPbX_3$ in [010] and $[00\bar{1}]$ projections. $X_0$ mark halogen atoms in the surface layer (CsX) and $X_{-1}$ – in the subsurface layer ($PbX_2$). The values of interatomic distances indicated are specified in Table 4.2. Dashed circles indicate atoms positioned behind (in the side view) or below (in the top view) of the other atoms shown.

TABLE 4.2: Geometry and adsorption energies ($E_{ads.}$) of CO, $CO_2$ and $O_2$ on CsX surfaces. The interatomic distances (indicated according to Figure 4.4) are in Å. The adsorption energies $E_{ads.}$ (in eV) are BSSE corrected; the BSSE contribution ($E_{BSSE}$) is given separately, for reference.

| X | | Cs–C | Cs–O | C–$X_0$ | O–$X_0$ | C–$X_{-1}$ | O–$X_{-1}$ | Cs–Cs | $X_0$–$X_0$ | $E_{ads}$ | $E_{BSSE}$ |
|---|---|---|---|---|---|---|---|---|---|---|---|
| CO configuration as described by Figure 4.4 (a) | | | | | | | | | | | |
| Cl: | CsCl-l | 3.48 | 3.34 | 3.30 | 3.62 | 3.18 | 3.60 | 6.67 | 6.92 | −0.12 | −0.16 |
| | CsCl-h | 3.50 | 3.64 | 3.19 | 3.60 | 5.19 | 5.68 | 5.37 | 4.96 | −0.07 | −0.15 |
| Br: | CsBr-l | 3.55 | 3.41 | 3.36 | 3.71 | 3.19 | 3.60 | 6.92 | 7.24 | −0.12 | −0.17 |
| | CsBr-h | 3.48 | 3.62 | 3.24 | 3.65 | 5.10 | 5.65 | 5.47 | 5.28 | −0.07 | −0.17 |
| I: | CsI-l | 3.61 | 3.48 | 3.51 | 3.85 | 3.28 | 3.72 | 6.96 | 7.21 | −0.12 | −0.23 |
| | CsI-h | 3.43 | 3.34 | 3.34 | 3.79 | 4.77 | 5.20 | 5.94 | 6.09 | −0.09 | −0.23 |
| $CO_2$ configuration as described by Figure 4.4 (b) | | | | | | | | | | | |
| Cl: | CsCl-l | | 3.19 | 3.21 | | 3.38 | | 6.86 | 6.99 | −0.29 | −0.07 |
| | CsCl-h | | 3.29 | 3.31 | | 5.45 | | 5.53 | 4.87 | −0.20 | −0.07 |
| Br: | CsBr-l | | 3.19 | 3.38 | | 3.38 | | 7.04 | 7.33 | −0.30 | −0.10 |
| | CsBr-h | | 3.26 | 3.45 | | 5.07 | | 6.05 | 5.74 | −0.20 | −0.10 |
| I: | CsI-l | | 3.27 | 3.77 | | 3.37 | | 7.60 | 7.33 | −0.34 | −0.20 |
| | CsI-h | | 3.22 | 3.50 | | 5.75 | | 6.57 | 5.77 | −0.19 | −0.20 |
| $O_2$ configuration as described by Figure 4.4 (c) | | | | | | | | | | | |
| Cl: | CsCl-l | | 3.51 | | 3.97 | | 3.70 | 6.61 | 6.97 | −0.05 | −0.05 |
| | CsCl-h | | 3.55 | | 3.62 | | 5.72 | 5.27 | 5.02 | −0.02 | −0.04 |
| Br: | CsBr-l | | 3.59 | | 4.04 | | 3.67 | 6.89 | 7.28 | −0.05 | −0.06 |
| | CsBr-h | | 3.76 | | 3.61 | | 5.70 | 5.54 | 5.31 | −0.01 | −0.07 |
| I: | CsI-l | | 3.51 | | 3.87 | | 3.64 | 7.70 | 7.61 | −0.15 | −0.05 |
| | CsI-h | | 3.51 | | 3.62 | | 5.70 | 5.30 | 5.84 | −0.11 | −0.04 |

The situation is the same for $CO_2$. The carbon dioxide molecule ended up in asymmetric horizontal orientation, similarly to CO bridging two adjacent top-layer Cs sites while hanging over the halogen atom of the underlying $PbX_2$ layer (cf. Figure 4.4b). As for CO, the "low" setting configurations bring about larger atomic relaxations around the molecules than the "high" setting ones, thus stabilising the molecule at the surface.

The $O_2$ molecule stabilizes itself in a similar configuration over the CsX surfaces (cf. Figure 4.4c). Remarkably, $E_{\mathrm{ads}}$ for $CsPbI_3$ is three times larger than for $CsPbCl_3$ and $CsPbBr_3$. Similarly as for the other molecules, the "low" settings induce larger atomic relaxations around the molecules.

To conclude, one should keep in mind that the adsorbed molecules, along with their underlying fragment of surface, find themselves in thermal vibrations, not grasped by the present static simulation. The zero-point energies of vibrations according to the highest modes of CO, $CO_2$ and $O_2$ (2102 $\mathrm{cm}^{-1}$, 2349 $\mathrm{cm}^{-1}$ and 2061 $\mathrm{cm}^{-1}$, respectively) are 0.13 eV, 0.15 eV and 0.10 eV, respectively (the vibration of adsorbed molecules is slightly different from the isolated ones, the chemical shift being less than 100 $\mathrm{cm}^{-1}$). It means that the only molecule about which one can reliably conclude that it tends to be adsorbed on the CsX surfaces is $CO_2$, whereas for the other two the adsorbed state might be dynamically unstable.

### 4.2.2 Adsorption on $PbX_2$-terminated surfaces

Similarly to how it was done above for the CsX-terminated surfaces, Figure 4.5 shows some representative snapshots of the adsorbed molecules, and Figure 4.6 marks the interatomic distances in the docking geometry, the numerical values of which are further on specified in Table 4.3, along with the respective adsorption energies. Here the situation is more straightforward than for the CsX-terminated surfaces. Since the surface remains relatively flat and each Pb site can be roughly considered as equivalent, it suffices to explore the adsorption properties near one site only. However, different molecules may accommodate themselves over the surface in two different ways depicted in Figure 4.6. The first possibility (see Figure 4.6 a and c) is that the molecule is pinned on top of an X atom in the $PbX_2$ layer (the case of $CO_2$ and $O_2$), or slightly displaced from it towards one of the Pb atoms, which make the 180° Pb-X-Pb bond. The

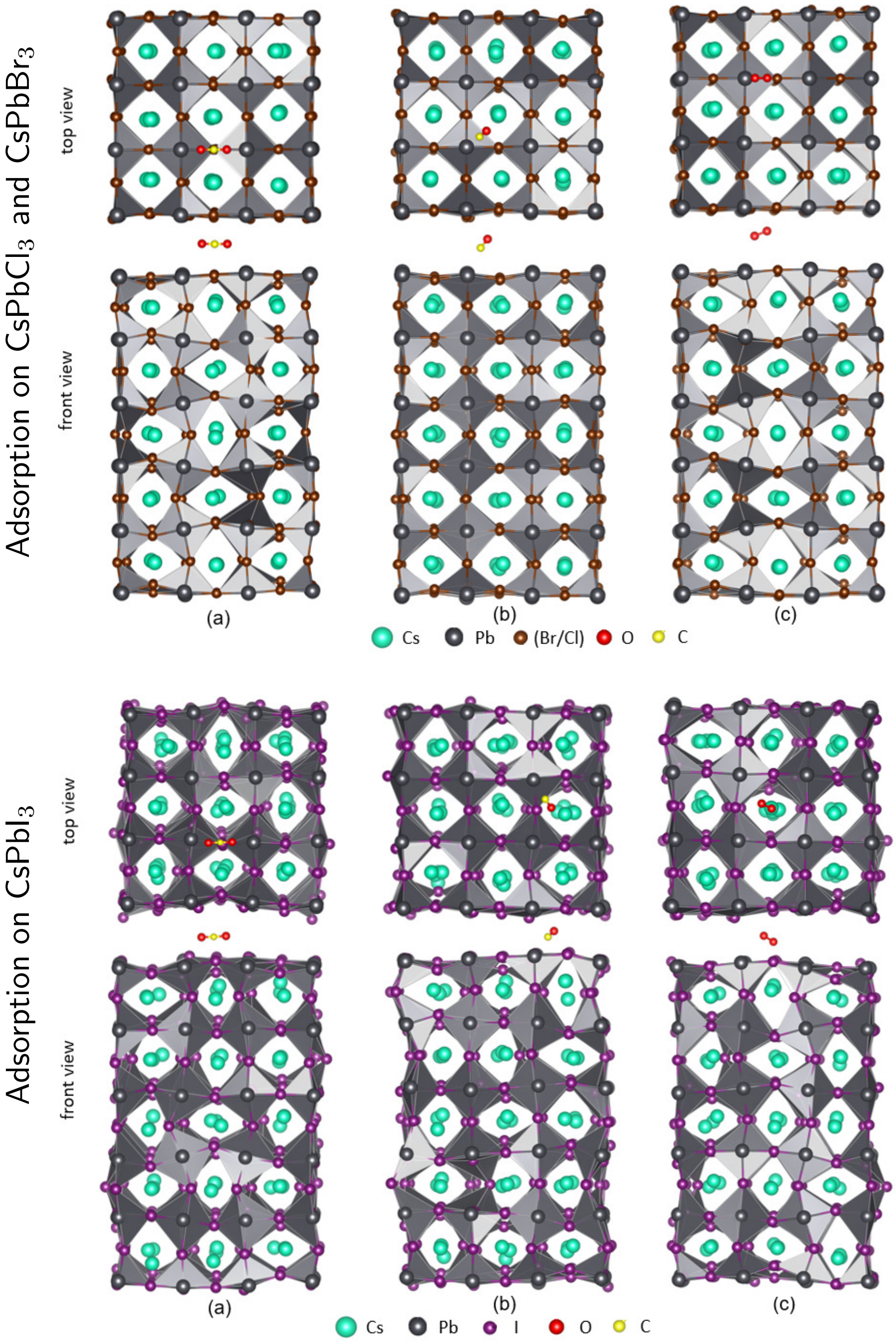

FIGURE 4.5: Similar to Figure 4.3, for the $PbX_2$-terminated (001) surfaces.

second possibility is the case of CO molecule (see Figure 4.6 b), still in the vicinity of a Pb atom, but oriented along the diagonal of a square formed by Pb atoms so that the molecule hangs over the Cs atom of the underlying (CsX) layer, and is flanked by $X_0$ atoms neighbouring the Pb (see Figure 4.6 b and d). Either way, the more negatively charged end of the molecule (C in CO, or O in $CO_2$) is turned towards the cation. Finally, only for $O_2$ adsorbed on $PbI_2$ surface (see Figure 4.6 d), the molecule lies on the top of the underlying Cs atom having very weak interaction with the surfaces.

The adsorption energies in Table 4.3 show that, for all materials, $CO_2$ and CO exhibit comparable interaction with the surfaces, exceeding that of $O_2$. As was already mentioned for the Cs-X terminated slabs, the BSSE correction was necessary, sometimes achieving the same size as the energy itself (for CO or over iodides). Neglecting it would have, therefore, completely distorted the trends.

Summarising this part, the adsorption energies of CO and $O_2$ with the $PbX_2$-terminated surfaces are comparable to their counterparts for CsX-terminated surfaces. In contrast, the adsorption energy for $CO_2$ on $PbX_2$ is roughly two times weaker than on CsX. This strengthens the observation done in the previous section concerning the comparison of these adsorption energies with the zero-point energies of the highest vibration modes of CO, $CO_2$ and $O_2$. From this comparison, none of these molecules can be adsorbed to be dynamically stable at the surface.

Since the adsorption of molecules was not so pronounced on these perfect $CsPbX_3$ surfaces, it is interesting to observe a similar effect on $CsPbX_3$ surfaces with defects.

TABLE 4.3: Geometry and adsorption energies ($E_{\mathrm{ads.}}$) of CO, $CO_2$ and $O_2$ on $PbX_2$ surfaces. The interatomic distances for different cases categorised depending on the orientation of molecules (indicated according to Figure 4.6) are in Å. The adsorption energies $E_{\mathrm{ads.}}$ (in eV) are BSSE corrected; the BSSE contribution ($E_{\mathrm{BSSE}}$) is given separately, for reference.

| | CO | | | $CO_2$ | | | $O_2$ | | |
|---|---|---|---|---|---|---|---|---|---|
| | case (a) | | | case (b) | | | case (c) | | case (d) |
| distance | X = Cl | X = Br | X =I | X = Cl | X = Br | X = I | X = Cl | X = Br | X = I |
| Pb−C | 2.96 | 2.97 | 3.01 | | | | | | |
| Pb−Cs | 4.75 | 4.85 | 5.92 | | | | | | 4.82 |
| Pb−O | | | | 3.26 | 3.40 | 3.33 | 3.37 | 3.27 | 4.31 |
| Pb−Pb | | | | | 5.70 | 5.90 | 6.15 | | |
| Pb−$X_0$ | | | | | | 2.85 | 2.95 | | |
| C−$X_0$ | 3.21 | 3.29 | 3.32 | 3.38 | 3.06 | 3.16 | 3.40 | | |
| Cs−O | 5.60 | 6.06 | 5.60 | 6.61 | | | | | 5.82 |
| O−$X_0$ | 3.80 | 3.89 | 3.93 | | | | 3.64 | 3.78 | 3.75 |
| $X_0$−$X_0$ | 3.98 | 4.17 | 4.65 | | | | | | |
| $E_{\mathrm{ads}}$ | −0.12 | −0.17 | −0.16 | −0.18 | −0.15 | −0.11 | −0.03 | −0.05 | 0.02 |
| $E_{\mathrm{BSSE}}$ | −0.16 | −0.16 | −0.19 | −0.05 | −0.05 | −0.14 | −0.02 | −0.01 | −0.13 |

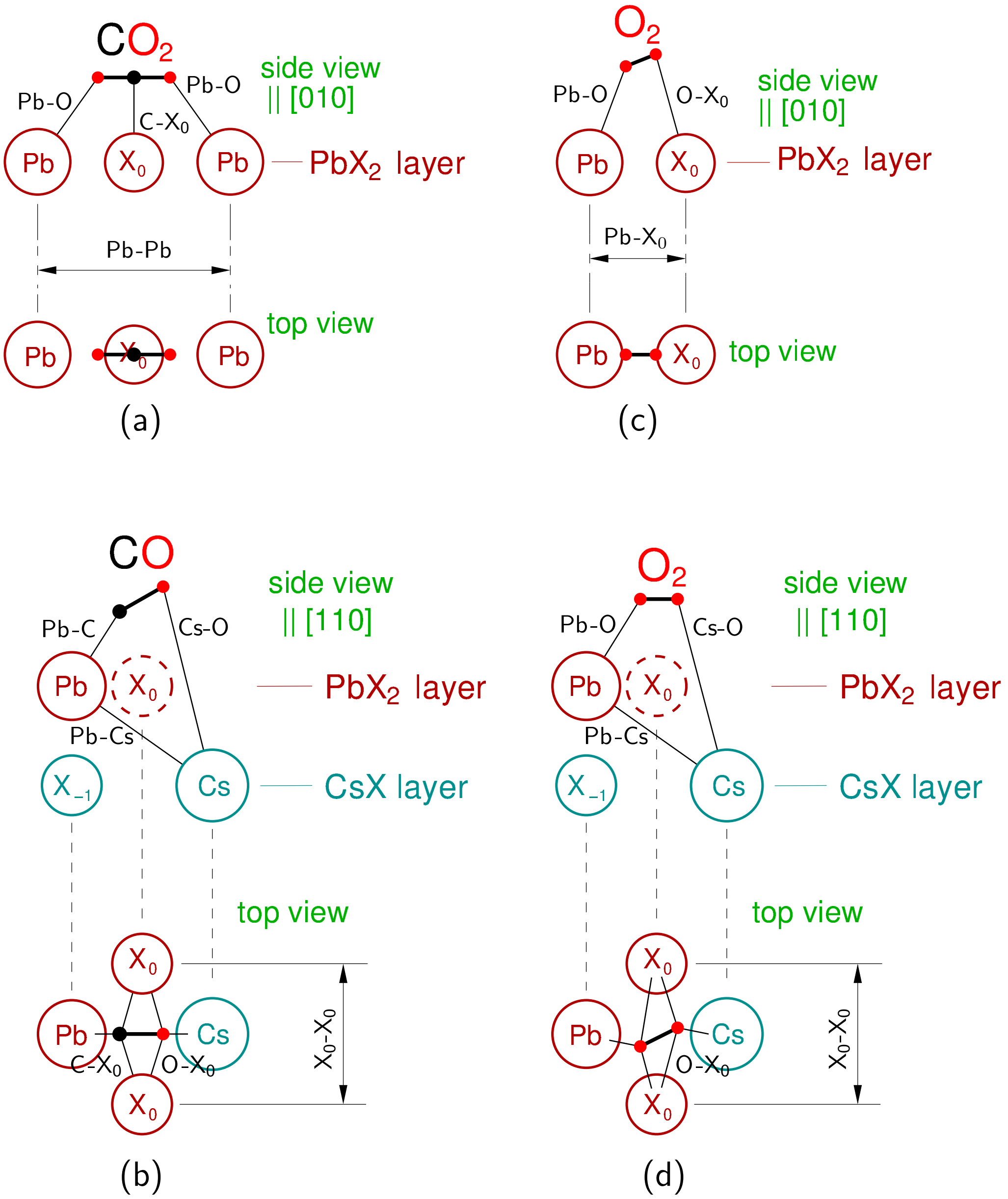

FIGURE 4.6: Schemes of docking of molecules at $PbX_2$ surfaces of $CsPbX_3$ in [010] (cases a, c) and [110] (cases b, d) projections, along with, in each case, the $[00\bar{1}]$ projection. $X_0$ mark halogen atoms in the surface layer ($PbX_2$), and $X_{-1}$ – in the subsurface layer (CsX). The values of interatomic distances indicated are specified in Table 4.3. Dashed circles indicate atoms positioned behind (in the side view) or below (in the top view) of the other atoms shown.

## 4.3 Adsorption on $CsPbX_3$ surfaces with vacancy defect

In the following, we attempt to simulate how such imperfections as vacancies defects on the surface may affect the adsorption of molecules.

For the (001) reconstructed surface of perovskites with different terminations, corresponding sites for halide vacancy were then inspected to study the interaction of $O_2$, $H_2O$, CO and $CO_2$ molecules. The sites for creating vacancies in the 3×3 supercell are again distinguished through numbering and are well discussed in Appendix. For CsX termination, different sites for creating charged and neutral vacancies were inspected due to the reconstruction of the CsX terminated surface. In the case of $PbX_2$ termination, no significant reconstruction is observed; hence all the halide sites are considered equivalent, and just one site has been explored. The details of vacancy creation are discussed in detail in Chapter 3. Following the trend from the perfect surface, the molecules are always introduced on the upper layer of the surface over the vacancy. The symmetry constraints are removed entirely, and the system is fully optimised. The molecules change the orientation and stay hanged over the vacancy.

For the different sites of vacancy, the final configurations of molecules are approximately the same for a similar type of vacancy with minor fluctuations in the adsorption energies, which can be again due to the “calculation noise” likewise as in the case of a perfect surface. The details of different sites of adsorption are given in the Tables A.9 through A.12.

### 4.3.1 Adsorption on CsX terminated surfaces

In principle, charged and neutral vacancies exhibit a variety of “docking positions”. An inspection of relaxed geometries throughout different trial adsorption sites and halogen species X permits however to single out just several “scenarios” of adsorption, which differ only in interatomic distances. In Table 4.4, the adsorption energy is reported for sites with high adsorption energy (absolute value) and the vacancy sites are indicated as V-CsCl, V-CsBr, V-CsI for the surfaces $CsPbCl_3$, $CsPbBr_3$ and $CsPbI_3$ respectively. Figure 4.7 schematically shows the “docking geometry” of oxygen and water (in two projections), which are similar for the cases of charged and neutral vacancy. $CO_2$ exhibits two different geometries for charged and neutral vacancies in the left and right panel respectively of Figure 4.8. The non-linearity of the $CO_2$ molecule is discussed in detail later. The interatomic distances and the adsorption energies are further specified in Table 4.4.

In what concerns the adsorption at the sites of charged vacancies, all the molecules turn out to hang between the two Cs atoms from the upper ( CsX) layer (see Figure 4.7 and Figure 4.8). In the case of charged vacancies, the $\mathrm{O{-}Pb_{-1}}$ (Pb from the $PbX_2$ layer) distance (see Tables 4.7 and 4.8) reveals that the molecules do not penetrate into the lattice. The $H_2O$ molecule on adsorption somehow displaces towards one of the neighbouring Cs atoms, as is seen from the disparity of the two Cs-O distances specified in Table 4.4. The $CO_2$ molecule practically aligns itself between the two Cs atoms such that, the two oxygen aligns close to the cesium and the two Cs−O distance varies around 5%. CO hangs between the two Cs such that the oxygen roughly hangs over the Pb atom.

For all the molecules, the charged defect does not make the adsorption of oxygen energetically favourable for all the surfaces. The adsorption energy is comparable to that at the perfect surface. $H_2O$ shows the highest adsorption energy for all the surfaces on the surfaces with charged vacancies. On $CsPbI_3$ surface, its adsorption energy is higher than on $CsPbBr_3$ and on $CsPbCl_3$ surfaces. This is due to the larger lattice parameter of $CsPbI_3$ allowing higher relaxations. $H_2O$ is followed by $CO_2$ in terms of adsorption energy, whereas $O_2$ has the lowest adsorption energy, as was the case for perfect surfaces.

Water can attack the perovskite in the dissociated state. This is modelled concerning the reaction of water on $CsPbX_3$ perovskite with charged vacancy. The corresponding reaction can be as follows:

$$\mathrm{CsPBX_3 + H_2O \longrightarrow CsPbX_2OH + HX} \quad . \tag{4.2}$$

The OH fragment enters the vacancy site at the surface $CsPbX_3$ surface, the final configuration of the OH molecule staying in the same way (see Figure 4.7) as the O–H branch of the water molecule on the CsX surface when the vacancy is charged. The

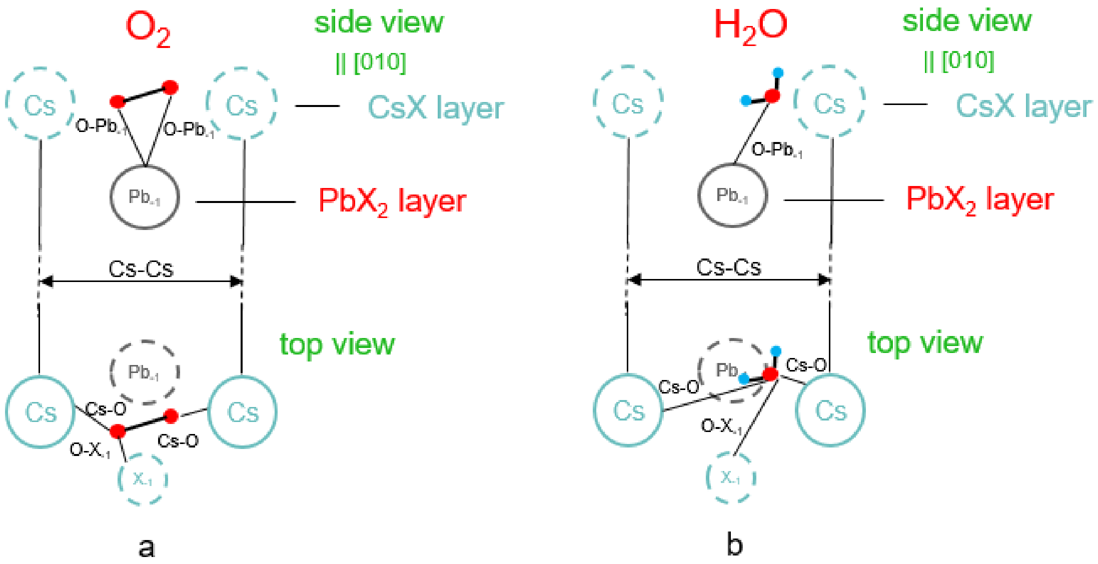

FIGURE 4.7: Schemes of docking of $O_2$ (a) and $H_2O$ (b) molecules at CsX surfaces of $CsPbX_3$ in [010] projections, along with, in each case, the $[00\bar{1}]$ projection. $X_{-1}$ is indicated for the subsurface layer (CsX). The values of interatomic distances indicated are specified in Tables A.12 and A.9. Dashed circles indicate atoms positioned behind (in the side view) or below (in the top view) of the other atoms shown. The schemes apply to both charged-vacancy and neutral-vacancy cases.

adsorption energy of the OH ion is $-3.97$ eV and $-3.47$ eV for $CsPbBr_3$ and $CsPbCl_3$ respectively. For the $CsPbI_3$ surface, the work is in progress. The adsorption energy of *dissociated* $H_2O$ specie indicates that the interaction of water molecules with the surface is enhanced when it attacks the perovskite in the dissociated state. In contrast, in the case of *non-dissociated* $H_2O$ molecule, the adsorption energy is lower and makes $-0.77$ and $-0.80$ eV respectively for $CsPbCl_3$ and $CsPbBr_3$.

In case of neutral vacancies, the molecules dock themselves slightly deeper as compared to the cases of charged vacancy. In the case of neutral vacancy, the calculation is spin polarised. The magnetic moment is assigned to the Pb atom (to which the removed halide atom was bonded) as discussed in Chapter 3. The interaction of oxygen with the surface having neutral vacancy is increased due to the interaction between the unpaired electron of Pb and the unpaired oxygen electron. Considerably shorter Pb$-$O distances indicated in Table 4.4 for neutral vacancies, as compared to charged ones, reveal this enhanced Pb–O interaction. The oxygen molecule tends to align between the two Cs atoms in an inclined position. Distances between the lower O atom

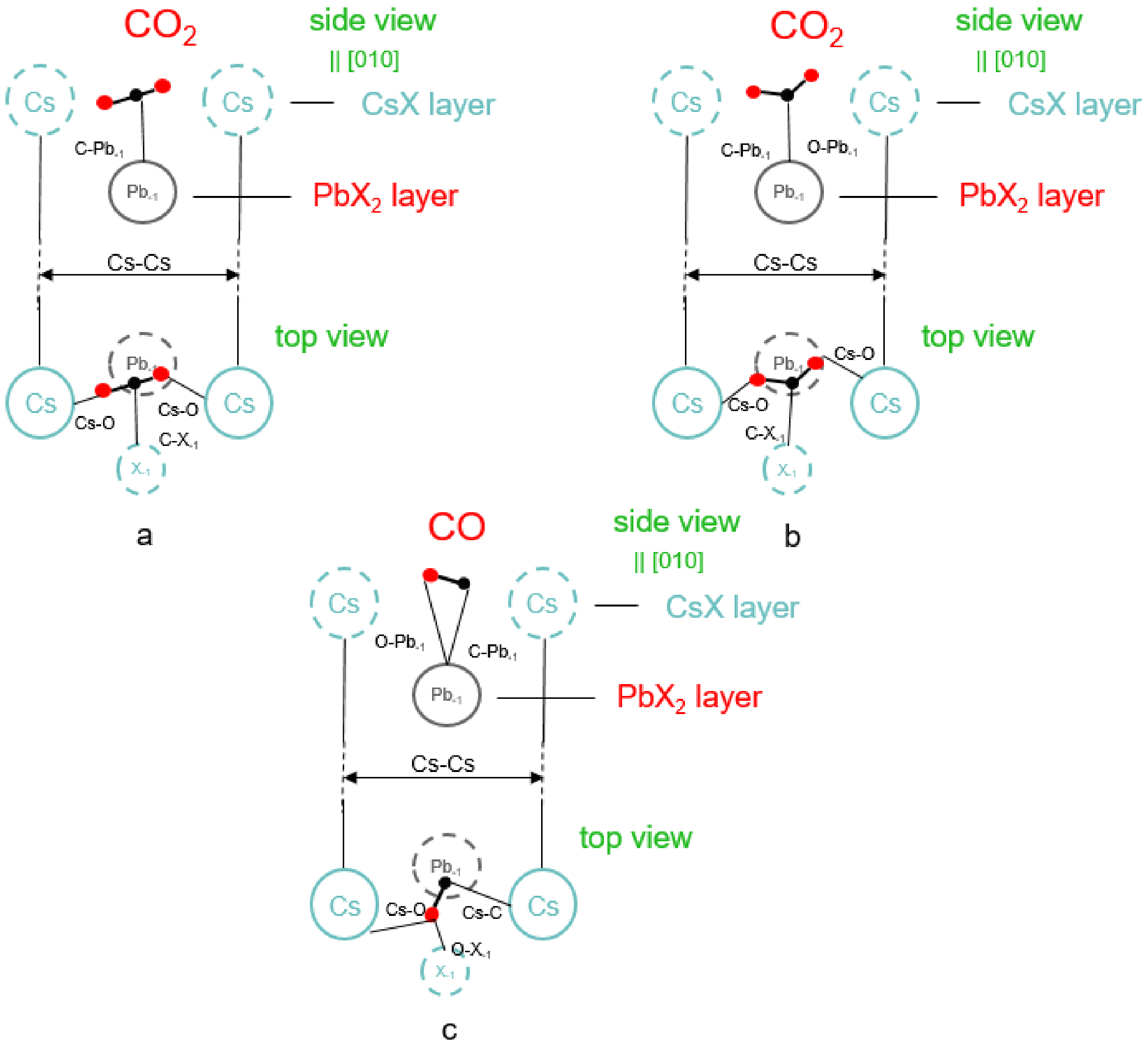

FIGURE 4.8: Similar to Figure 4.7. (a) and (b) are cases for arrangement of $CO_2$ on charged and neutral vacancy (non-linearity of $CO_2$ is discussed in the text) on CsX terminated structure respectively and; (c) applies to CO in both charged-vacancy and neutral-vacancy cases. Interatomic distances are specified in Tables A.10 and A.11.

TABLE 4.4: Relaxed interatomic distances (in Å) and adsorption energy (in eV) of different molecules, calculated for different sites shown in Figures 4.8 and 4.7

| | X | | Cs−C | Cs−O | C−Pb$_{-1}$ | O−Pb$_{-1}$ | O−X$_{-1}$ | Cs−Cs | $E_{\text{ads.}}$ |
|---|---|---|---|---|---|---|---|---|---|
| $CO_2$ molecule | (see Figure 4.8 a, b) | | | | | | | | |
| Charged Vacancy | Cl | V-CsCl | | 3.54−3.29 | 4.00 | | 3.60 | 6.23 | −0.24 |
| | Br | V-CsBr | | 3.22−3.23 | 5.88 | | 3.58 | 7.12 | −0.38 |
| | I | V-CsI | | 3.10−3.16 | 4.31 | | 3.87 | 8.07 | −0.39 |
| Neutral Vacancy | Cl | V-CsCl | | 3.24−3.16 | 2.64 | | 3.81 | 5.86 | −0.98 |
| | Br | V-CsBr | | 3.46−3.26 | 2.30 | | 4.33 | 5.92 | −1.04 |
| | I | V-CsI | | 3.39−3.24 | 2.64 | | 3.82 | 5.48 | −0.90 |
| CO molecule | (see Figure 4.8 c) | | | | | | | | |
| Charged Vacancy | Cl | V-CsCl | 4.56 | 3.69 | 3.34 | 3.95 | 3.58 | 6.88 | −0.25 |
| | Br | V-CsBr | 4.63 | 3.45 | 2.93 | 4.02 | 3.91 | 6.30 | −0.36 |
| | I | V-CsI | 4.62 | 3.36 | 2.92 | 4.07 | 3.91 | 7.69 | −0.35 |
| Neutral Vacancy | Cl | V-CsCl | 3.35 | 3.27 | 2.67 | 3.38 | 3.95 | 5.62 | −0.69 |
| | Br | V-CsBr | 4.63 | 3.31 | 2.66 | 3.40 | 3.72 | 5.36 | −0.68 |
| | I | V-CsI | 3.58 | 3.19 | 2.76 | 3.43 | 4.04 | 7.03 | −0.85 |
| $O_2$ molecule | (see Figure 4.7 a) | | | | | | | | |
| Charged Vacancy | Cl | V-CsCl | | 4.58−3.84 | | 3.50−4.08 | 3.76 | 6.42 | −0.09 |
| | Br | V-CsBr | | 3.74−4.01 | | 3.77−4.07 | 3.69 | 6.50 | −0.10 |
| | I | V-CsI | | 3.49−3.56 | | 3.38−3.97 | 3.72 | 7.52 | −0.21 |
| Neutral vacancy | Cl | V-CsCl | | 3.24−3.31 | | 2.43−2.44 | 3.54 | 5.44 | −2.53 |
| | Br | V-CsBr | | 3.30−3.51 | | 2.58−2.59 | 4.14 | 5.49 | −2.32 |
| | I | V-CsI | | 3.09−3.14 | | 2.44−3.24 | 3.68 | 5.39 | −2.43 |
| $H_2O$ molecule | (see Figure 4.7 b) | | | | | | | | |
| Charged vacancy | Cl | V-CsCl | | 3.22−3.54 | | 5.69 | 4.42 | 6.05 | −0.77 |
| | Br | V-CsBr | | 3.45−4.45 | | 2.70 | 3.72 | 5.82 | −0.80 |
| | I | V-CsI | | 3.23−4.83 | | 2.74 | 3.49 | 7.21 | −0.93 |
| Neutral Vacancy | Cl | V-CsCl | | 3.33−3.44 | | 3.73 | 3.96 | 6.02 | −0.94 |
| | Br | V-CsBr | | 3.45−4.46 | | 2.70 | 3.24 | 7.01 | −0.89 |
| | I | V-CsI | | 3.07−4.60 | | 3.77 | 3.62 | 7.37 | −1.28 |

and the Pb atom of $PbX_2$ layer are listed in Table 4.4 for every adsorption site. In the final configuration, Pb loses its magnetic moment indicating stronger interaction of oxygen with the surface. However, for the cases of CO, $CO_2$ and $H_2O$ molecules, the Pb atom in the final configuration has a magnetic moment.

$H_2O$ and CO molecules behave similarly in the final configuration as in individual cases related to charged vacancy. For $CO_2$, the molecule bends such that the C atom is close to the Pb atom and the two oxygen atoms are at some angle pointing towards the Cs atom. The bending of the $CO_2$ molecule is attributed to the transfer of charges from Pb to C of $CO_2$. It is further discussed in the coming paragraphs.

For all the molecules, the adsorption energies on the surface with neutral vacancy are higher than that of the surface with charged vacancy. The adsorption energy of the $O_2$ molecule is the highest, followed by $H_2O$, $CO_2$ and CO.

To better understand the delocalisation of charges, Mulliken population analysis indicating the overlap occupation values are shown in the Table 4.5. In the case of neutral vacancies, the overlap occupation values of Pb–O are higher than the charged ones. For the $CO_2$ molecule on surfaces with neutral vacancy, the overlap occupation value is over 0.08 between C and the neighbouring Pb atom and 0.06 for the two O of $CO_2$ molecule (for the independent $CO_2$ molecule, the overlap occupation value between O and C is 0.55). This indicates that the charges are redistributed between the $CO_2$ molecule and Pb atom. Also, for the case of $O_2$ and CO on surfaces with neutral vacancies, the charges are delocalised within $O_2$ and its neighbouring atoms. To further investigate the bonding between the molecule and surface, the density of states of the pure surface and surface with the molecule is compared. This will be further discussed in the section on Electronic structures.

### 4.3.2 Adsorption on $PbX_2$ terminated surfaces

Unlike CsX termination, the $PbX_2$ termination provides only one site for vacancy creation. The molecules are introduced in the vacancy site. All trial molecules, initially placed at the vacancy site, remained their also following the full relaxation. They do not penetrate deeper into the lattice. In case of charged vacancy, the molecules hang between the two Pb atoms such that the O atom from $CO_2$, $H_2O$ and $O_2$ and C atom

TABLE 4.5: Mulliken population analysis for $CO_2$, CO, $O_2$ and $H_2O$ molecules adsorbed on the CsX terminated surface of $CsPbX_3$ with charged and neutral halide vacancy. Only the three nearest neighbours of molecules adsorbed at the surface are shown in the Table.

| | X | | Cs−C | Cs−O | C−Pb | O−Pb | O−C | O−O | O−H |
|---|---|---|---|---|---|---|---|---|---|
| $CO_2$ molecule | | | | | | | | | |
| Charged Vacancy | Cl | V-CsCl | 0.00 | 0.002−0.002 | 0.001 | 0.006−0.000 | 0.498−0.469 | 0.082 | |
| | Br | V-CsBr | 0.00 | 0.00−0.001 | 0.00 | 0.00−0.00 | 0.482−0.482 | 0.087 | |
| | I | V-CsI | 0.00 | 0.008−0.008 | 0.00 | 0.001−0.001 | 0.542−0.542 | 0.090 | |
| Neutral Vacancy | Cl | V-CsCl | 0.00 | 0.00−0.00 | 0.093 | 0.020−0.018 | 0.067−0.067 | 0.012 | |
| | Br | V-CsBr | 0.00 | 0.00−0.00 | 0.092 | 0.020−0.019 | 0.066−0.066 | 0.012 | |
| | I | V-CsI | 0.00 | 0.00−0.00 | 0.087 | 0.018−0.017 | 0.066−0.066 | 0.012 | |
| CO molecule | | | | | | | | | |
| Charged Vacancy | Cl | V-CsCl | 0.00 | 0.001 | 0.018 | 0.001 | 0.644 | | |
| | Br | V-CsBr | 0.00 | 0.00 | 0.034 | 0.001 | 0.610 | | |
| | I | V-CsI | 0.00 | 0.00 | 0.033 | 0.00 | 0.626 | | |
| Neutral Vacancy | Cl | V-CsCl | 0.00 | 0.00 | 0.052 | 0.030 | 0.113 | | |
| | Br | V-CsBr | 0.00 | 0.00 | 0.043 | 0.028 | 0.102 | | |
| | I | V-CsI | 0.00 | 0.00 | 0.044 | 0.025 | 0.089 | | |
| $O_2$ molecule | | | | | | | | | |
| Charged Vacancy | Cl | V-CsCl | | 0.00−0.001 | | 0.001−0.001 | | 0.400 | |
| | Br | V-CsBr | | 0.00−0.00 | | 0.00−0.001 | | 0.393 | |
| | I | V-CsI | | 0.00−0.00 | | 0.002−0.001 | | 0.397 | |
| Neutral vacancy | Cl | V-CsCl | | 0.002−0.002 | | 0.022−0.026 | | 0.184 | |
| | Br | V-CsBr | | 0.010−0.009 | | 0.024−0.014 | | 0.182 | |
| | I | V-CsI | | 0.011−0.014 | | 0.029−0.016 | | 0.185 | |
| $H_2O$ molecule | | | | | | | | | |
| Charged vacancy | Cl | V-CsCl | | 0.015 | | 0.019 | | | 0.249−0.274 |
| | Br | V-CsBr | | 0.007 | | 0.013 | | | 0.248−0.260 |
| | I | V-CsI | | 0.004 | | 0.027 | | | 0.214−0.214 |
| Neutral Vacancy | Cl | V-CsCl | | 0.001 | | 0.034 | | | 0.214−0.214 |
| | Br | V-CsBr | | 0.004 | | 0.042 | | | 0.259−0.259 |
| | I | V-CsI | | 0.003 | | 0.030 | | | 0.202−0.202 |

TABLE 4.6: Similar to table 4.5, for $PbX_2$ terminated structure.

| | X | Cs−O | C−Pb | O−Pb | O−C | O−O | O−H |
|---|---|---|---|---|---|---|---|
| $CO_2$ molecule | | | | | | | |
| Charged Vacancy | Cl | 0.00−0.00 | 0.00 | 0.001−0.001 | 0.495−0.451 | 0.080 | |
| | Br | 0.00−0.00 | 0.00 | 0.001−0.016 | 0.490−0.447 | 0.082 | |
| | I | 0.00−0.00 | 0.00 | 0.004−0.006 | 0.492−0.492 | 0.090 | |
| Neutral Vacancy | Cl | 0.00−0.00 | 0.084 | 0.015−0.016 | 0.067−0.067 | 0.010 | |
| | Br | 0.00−0.00 | 0.081 | 0.008−0.014 | 0.063−0.057 | 0.009 | |
| | I | 0.00−0.00 | 0.001 | 0.004−0.004 | 0.063−0.063 | 0.084 | |
| CO molecule | | | | | | | |
| Charged Vacancy | Cl | 0.00 | 0.00 | 0.014 | 0.005 | 0.647 | |
| | Br | 0.00 | 0.00 | 0.015 | 0.002 | 0.647 | |
| | I | 0.001 | 0.00 | 0.007 | 0.004 | 0.639 | |
| Neutral Vacancy | Cl | 0.00 | 0.00 | 0.060 | 0.022 | 0.115 | |
| | Br | 0.00 | 0.00 | 0.052 | 0.021 | 0.106 | |
| | I | 0.00 | 0.00 | 0.042 | 0.023 | 0.089 | |
| $O_2$ molecule | | | | | | | |
| Charged Vacancy | Cl | | 0.00−0.001 | | 0.001−0.001 | 0.410 | |
| | Br | | 0.00−0.00 | | 0.00−0.001 | 0.397 | |
| | I | | 0.00−0.00 | | 0.000−0.001 | 0.393 | |
| Neutral vacancy | Cl | | 0.001−0.001 | | 0.022−0.026 | 0.182 | |
| | Br | | 0.010−0.009 | | 0.024−0.014 | 0.182 | |
| | I | | 0.010−0.012 | | 0.024−0.014 | 0.187 | |
| $H_2O$ molecule | | | | | | | |
| Charged vacancy | Cl | | 0.003 | | 0.032 | | 0.250−0.268 |
| | Br | | 0.013 | | 0.034 | | 0.263−0.263 |
| | I | | 0.046 | | 0.003 | | 0.263−0.263 |
| Neutral Vacancy | Cl | | 0.00 | | 0.041 | | 0.220−0.220 |
| | Br | | 0.001 | | 0.030 | | 0.250−0.250 |
| | I | | 0.003 | | 0.028 | | 0.206−0.206 |

TABLE 4.7: interatomic distances (indicated in Figure 4.10, in Å) and adsorption energies $E_{\text{ads}}$ (in eV) for CO and $CO_2$ adsorption $PbX_2$ surfaces with charged and neutral vacancy.

| | | CO | | | $CO_2$ | | |
|---|---|---|---|---|---|---|---|
| | distance | X = Cl | X = Br | X =I | X = Cl | X = Br | X = I |
| Charged vacancy | Pb−C | | | | 3.96 | | 4.21 |
| | O−Cs$_{-1}$ | | | | 4.31 | 4.41 | 4.28 |
| | C−Cs$_{-1}$ | 4.29 | 4.41 | 3.38 | 4.44 | 4.57 | 4.54 |
| | Pb−O | 3.81 | 4.14 | 3.60 | 3.30 | 3.47−4.91 | 3.62 |
| | Pb−Pb | 5.89 | 6.23 | 6.86 | 5.84 | 6.31 | 6.70 |
| | $E_{\text{ads}}$ | −0.21 | −0.34 | −0.35 | −0.24 | −0.27 | −0.38 |
| Neutral Vacancy | Pb−C | | | | 2.62 | 2.62 | 2.71 |
| | O−Cs$_{-1}$ | | | | 3.36 | 3.44 | 3.25 |
| | C−Cs$_{-1}$ | 3.85 | 3.93 | 3.38 | | | |
| | Pb−O | 3.32 | 3.35−3.41 | 3.74−4.01 | 3.21 | 2.65 | 3.25 |
| | Pb−Pb | 5.27 | 5.28 | 7.57 | 5.74 | 5.74 | 5.92 |
| | $E_{\text{ads}}$ | −0.51 | −0.62 | −0.40 | −0.68 | −0.46 | −0.51 |

from CO lie over one of the Cs atoms from the CsX layer. The schematics of different molecules are shown in Figures 4.9 and 4.10. $O_2$ rests in a tilted position between two Pb atoms. $H_2O$ moves towards a Cs atom of the underlying CsX layer while staying at the level of the upper $PbX_2$ layer. CO and $CO_2$ align themselves in a tilted vertical orientation between the two Pb atoms.

In case of neutral vacancy, $O_2$ and CO show similar configuration as in the case of charged vacancy while $H_2O$ and $CO_2$ go towards the Pb atom. In the case of $CO_2$, the bending of the molecule occurs such that C from $CO_2$ moves towards the Pb atom with the unpaired electron and the two O atoms hang between two Cs from the CsX layer forming an angle between C and O atoms. The CO molecule hangs in a tilted vertical orientation between the two Pb atoms such that C from CO is close to the Cs atom from the CsX layer.

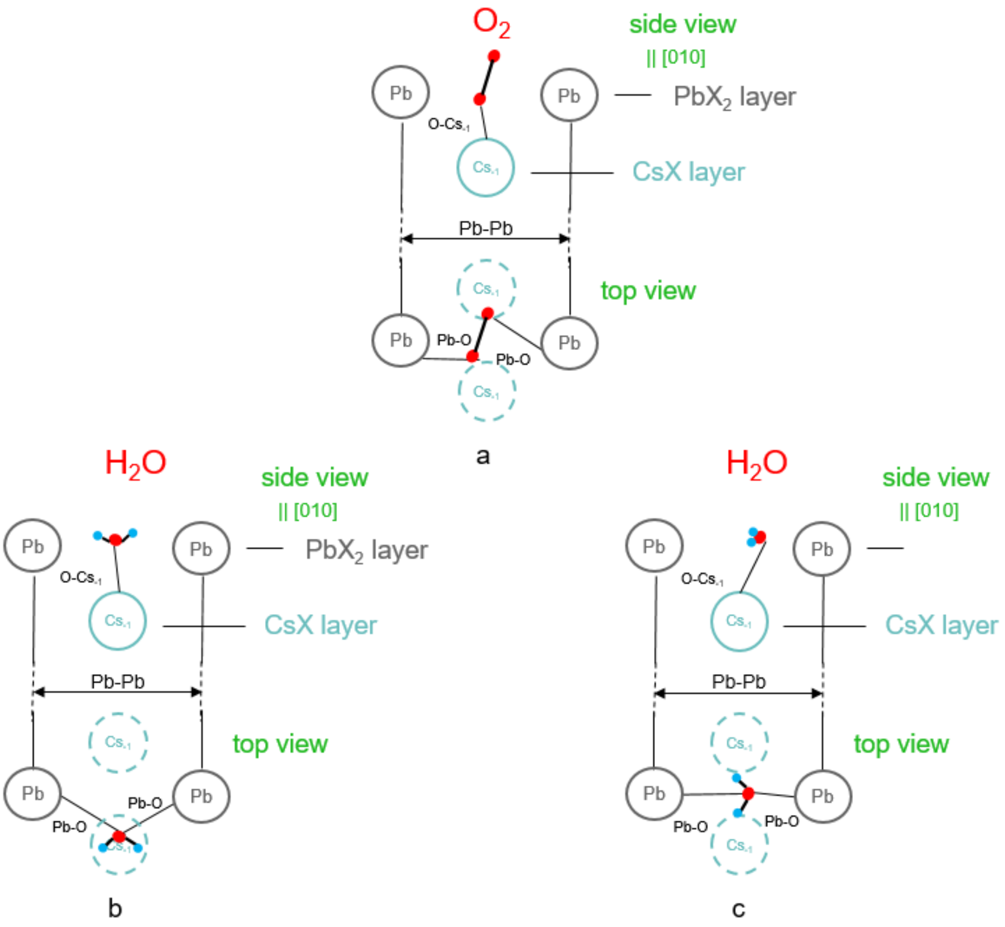

FIGURE 4.9: Schemes of docking of (a) $O_2$, for the both cases of charged and neutral vacancy, and (b, c) of $H_2O$, for the cases of charged and neutral vacancy, respectively, at $PbX_2$ surfaces of $CsPbX_3$ in [010] projections, along with, in each case, the $[00\bar{1}]$ projection. $X_{-1}$ is in the subsurface layer (CsX). The values of interatomic distances indicated are specified in Table 4.8. Dashed circles indicate atoms positioned behind (in the side view) or below (in the top view) of the other atoms shown.

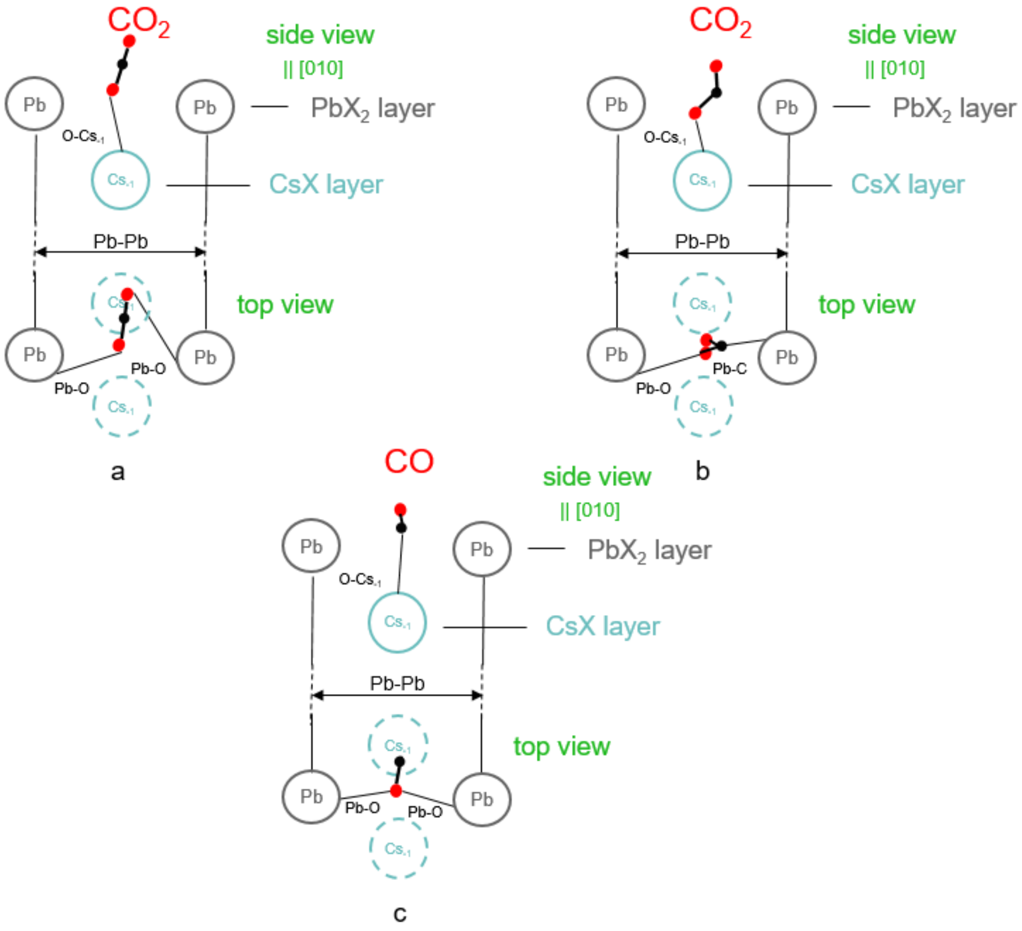

FIGURE 4.10: Schemes of docking for the $CO_2$ (a – charged vacancy, b – neutral vacancy) and CO (c – applies to both charged and neutral vacancy cases) on the $PbX_2$ terminated surface. Interatomic distances are given in Table 4.7.

TABLE 4.8: Geometry and adsorption energies ($E_{\text{ads.}}$ in eV) of $O_2$ and $H_2O$ on $PbX_2$ surfaces with charged and neutral vacancy. The interatomic distances (indicated according to Figure 4.9) are in Å.

| | | $O_2$ | | | $H_2O$ | | |
|---|---|---|---|---|---|---|---|
| | distance | X = Cl | X = Br | X =I | X = Cl | X = Br | X = I |
| Charged vacancy | | | | | | | |
| | $O-Cs_{-1}$ | 4.46 | 4.35 | 3.54 | 3.30 | 3.25 | 2.47 |
| | Pb−O | 3.41 | 3.54 | 3.75 | 3.35 | 3.63 | 3.96 |
| | Pb−Pb | 5.90 | 6.43 | 6.48 | 5.77 | 6.27 | 6.84 |
| | $E_{\text{ads}}$ | −0.11 | −0.12 | −0.17 | −0.51 | −0.62 | −0.80 |
| Neutral Vacancy | | | | | | | |
| | $O-Cs_{-1}$ | 3.37 | 3.30 | 3.25 | 5.05 | 3.25 | 3.16 |
| | Pb−O | 2.47−2.56 | 2.50−2.54 | 2.53−2.62 | 2.74−5.04 | 2.69−3.71 | 3.03−4.17 |
| | Pb−Pb | 5.57 | 5.61 | 5.77 | 5.82 | 5.96 | 6.01 |
| | $E_{\text{ads}}$ | −2.16 | −1.96 | −2.55 | −0.59 | −0.63 | −1.01 |

TABLE 4.9: Adsorption energies (in eV) for the perfect and defective (with vacancy) surface.

| | Perovskite | molecule | Perfect surface | Surface with Vacancy | |
|---|---|---|---|---|---|
| | | | | Charged | Neutral |
| CsX termination | $CsPbCl_3$ | $CO_2$ | −0.36 | −0.39 | −0.98 |
| | | CO | −0.28 | −0.25 | −0.69 |
| | | $O_2$ | −0.10 | −0.09 | −2.53 |
| | $CsPbBr_3$ | $CO_2$ | −0.40 | −0.68 | −0.90 |
| | | CO | −0.29 | −0.81 | −0.68 |
| | | $O_2$ | −0.11 | −0.10 | −2.32 |
| | $CsPbI_3$ | $CO_2$ | −0.54 | −0.39 | −0.90 |
| | | CO | −0.35 | −0.35 | −0.85 |
| | | $O_2$ | −0.20 | −0.21 | −2.43 |
| $PbX_2$ termination | $CsPbCl_3$ | $CO_2$ | −0.18 | −0.24 | −0.68 |
| | | CO | −0.12 | −0.21 | −0.51 |
| | | $O_2$ | −0.03 | −0.11 | −2.16 |
| | $CsPbBr_3$ | $CO_2$ | −0.15 | −0.27 | −0.46 |
| | | CO | −0.17 | −0.34 | −0.62 |
| | | $O_2$ | −0.05 | −0.12 | −1.96 |
| | $CsPbI_3$ | $CO_2$ | −0.11 | −0.38 | −0.51 |
| | | CO | −0.16 | −0.35 | −0.40 |
| | | $O_2$ | −0.02 | −0.17 | −2.55 |

For the surface with vacancies, CsX terminated surfaces with neutral vacancy show higher adsorption energy than the $PbX_2$ terminated structures for all the molecules. Oxygen has the highest adsorption energy for surface with neutral vacancy irrespective of the surface termination, while in what concerns the interaction with charged vacancies, $H_2O$ has the highest adsorption energy, whatever be the surface termination.

Summarising the findings on perfect surface and surface with a vacancy for $CsPbX_3$ compounds (see Table 4.9), it can be seen that upon addition of molecules at the surfaces with charged halide vacancy defect, there is no significant increase in the adsorption energy of molecules with CsX terminated structures. This implies that the molecules on the perfect surface and surface with charged vacancy weakly interact with the surface, and the interaction can be regarded as physisorption.

For $PbX_2$ terminated structures with charged vacancy, the increase in the adsorption energy of molecules is up to 80–90% in comparison to that of the perfect surface. The overlap occupation values in Table 4.6 indicate the charge transfer between the surface and molecule (Pb–O) is higher than that of the CsX terminated structure. This suggests that the energetics of molecules on the $PbX_2$ terminated surface with a charged vacancy is enhanced in comparison to that of the molecule on the perfect surface.

For the case of surfaces with neutral vacancies, the adsorption energies of molecules show a significant increase as compared to that of surfaces with charged vacancy. The increase in adsorption energy is attributed to the fact that charge transfer occurs between the molecules and the surface as suggested by the Mulliken overlap occupation analysis (see Table 4.6 and 4.5). The interaction of molecule and surface, in this case, can be regarded as chemisorption.

## 4.4 Electronic structure resulting from the adsorption

### 4.4.1 Perfect $CsPbX_3$ surface

The previously discussed total energy trends come about via tiny modifications of the electronic structure of slabs and molecules in the process of adsorption. Figure 4.11 presents the total density of states (DOS) of the upper valence bands and lower conduction bands of the free and adsorbed whole perfect slabs of $CsPbI_3$ for both types of terminations. It summarises the general trend found for each system, and an immediate comparison can be made with recent simulations of $CO_2$ and CO on $CsPbBr_3$ [Tang et al., 2019], as well as of $CO_2$ and $O_2$ on $CsPbI_3$ [Jiang et al., 2018].

The introduction of the molecule on the perfect surface has no significant impact on the electronic structure of the surfaces, whatever the perovskites, types of surfaces and molecules. Neither there is any change in the state at the highest occupied and lowest unoccupied bands: the top of the valence band and the bottom of the conduction band is mainly made of X-$p$ and Cs/Pb-$s$ orbitals, respectively, without any noticeable change in the density of states concerning the free surfaces.

Bonding and antibonding states in $CO_2$ and CO have moved apart by $\simeq \pm 5$ eV from the reference energy level (bottom of the valence band). The occupied state falls into the gap between the caesium and iodine $5p$ states. The specificity of $O_2$ is the spin of the isolated molecule due to spin polarised calculations. The energy difference between the partially occupied and unoccupied O$2p$ states in our calculation amounts to $\sim 5$ eV; the occupied level falls into the valence band. The energies of the corresponding levels will depend on the proximity of the oxygen with the lead or caesium, for the CsX-terminated and $Pb(Cl/Br)_2$-terminated surfaces $O_2$ lying at $\approx 3.5$ Å of Cs and Pb, the O-$p$ partially occupied and unoccupied states are located at 1 eV below and above the Fermi level (in the band gap), respectively; whereas, for the $PbI_2$-terminated surfaces of $CsPbI_3$, since the oxygen is at 4.3 Å of the lead, these two levels are located at 2 eV below and above the Fermi level.

No charge transfer or otherwise the creation of covalent bonds is seen between the molecule and the surface. The slight admixture of C$2p$ or O$2p$ states is noticeable.

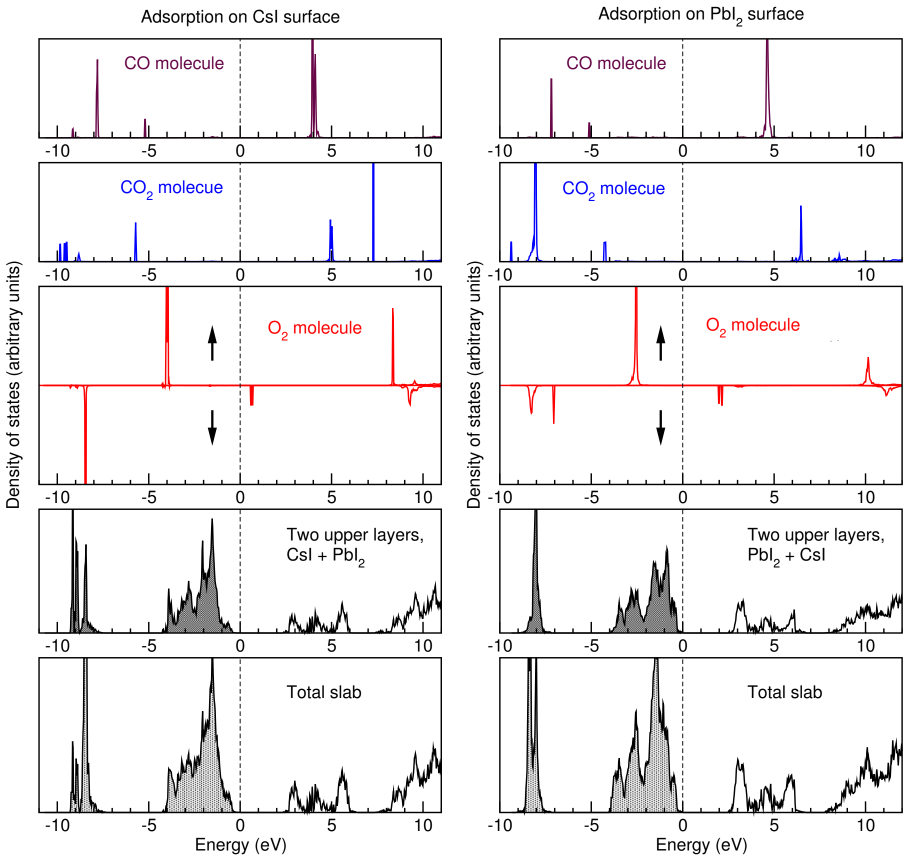

FIGURE 4.11: Densities of states of CO, $CO_2$ and $O_2$ molecules adsorbed on CsI surface (left column) and on the $PbI_2$ surface (right column) of $CsPbI_3$. The energies are given concerning the valence band top; the scaling of DOS is chosen out of convenience and unrelated in different plots. The bottom panels show the DOS of the whole corresponding slab (11 layers), the next-to-bottom panel – the cumulate DOS of the two upper atom layers. See text for details.

Therefore, the "observed" type of behaviour of all the molecules studied at the $CsPbX_3$ surfaces can be identified as physisorption.

## 4.4.2 $CsPbX_3$ surfaces with vacancies

### 4.4.2.1 Charged Vacancy

Bandgap values witness no significant change upon creation of charged vacancy and also with the addition of molecules, like this is the case with perfect surface as well. DOS of surface (defective) with molecule and the surface (defective) without molecule has no significant difference. The contribution of molecules to the total DOS is negligible.

### 4.4.2.2 Neutral Vacancy

The bandgap of the surface remains unaffected upon the creation of neutral vacancies and the introduction of molecules on the surfaces with neutral vacancies. On adsorption of a $H_2O$ molecule, the DOS of the surface with neutral vacancy does not change much. Under adsorption of $O_2$, however, the shift in the total DOS can be seen in Figure 4.12. This shift indicates the charge transfer between the $O_2$ and the Pb atom. The shift is by $\simeq 1.2$ eV for CsI termination and $\simeq 1.5$ eV for $PbI_2$ termination. In the case of $CO_2$, as discussed before, the molecule loses its linearity because of the charge transfer between the molecule and the neighbouring Pb atom. The shift in the DOS (see Figure 4.13) implies that the charges are redistributed among the molecule and the Pb atom.

The introduction of molecules on the surfaces of $CsPbX_3$ suggests that the damaging effect on the perfect surface is lower than at the surface with vacancy defects, particularly with neutral vacancy, which seems to be a rather hypothetical case. However, the issue of neutral vacancy cannot be neglected as there is a possibility that charged vacancy can become neutral.

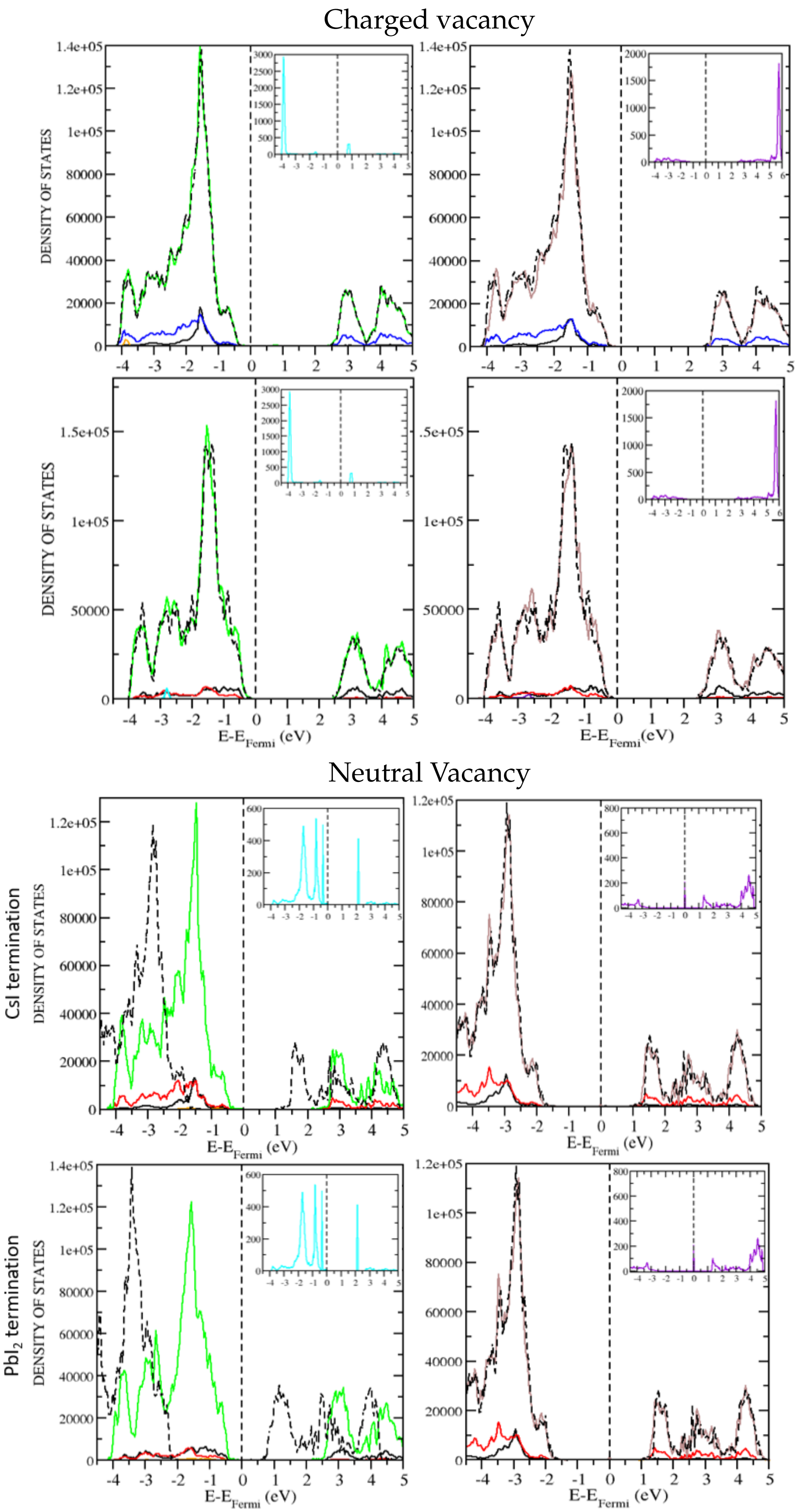

FIGURE 4.12: Total DOS of $O_2$ (left panel) and $H_2O$ (right panel) adsorbed on the CsI and $PbI_2$ terminated surfaces of $CsPbI_3$. The dashed line represents the total DOS of free surfaces. Black and red lines represent the DOS of the first and second layers, respectively. Inset shows the DOS of the corresponding molecule on the respective surface.

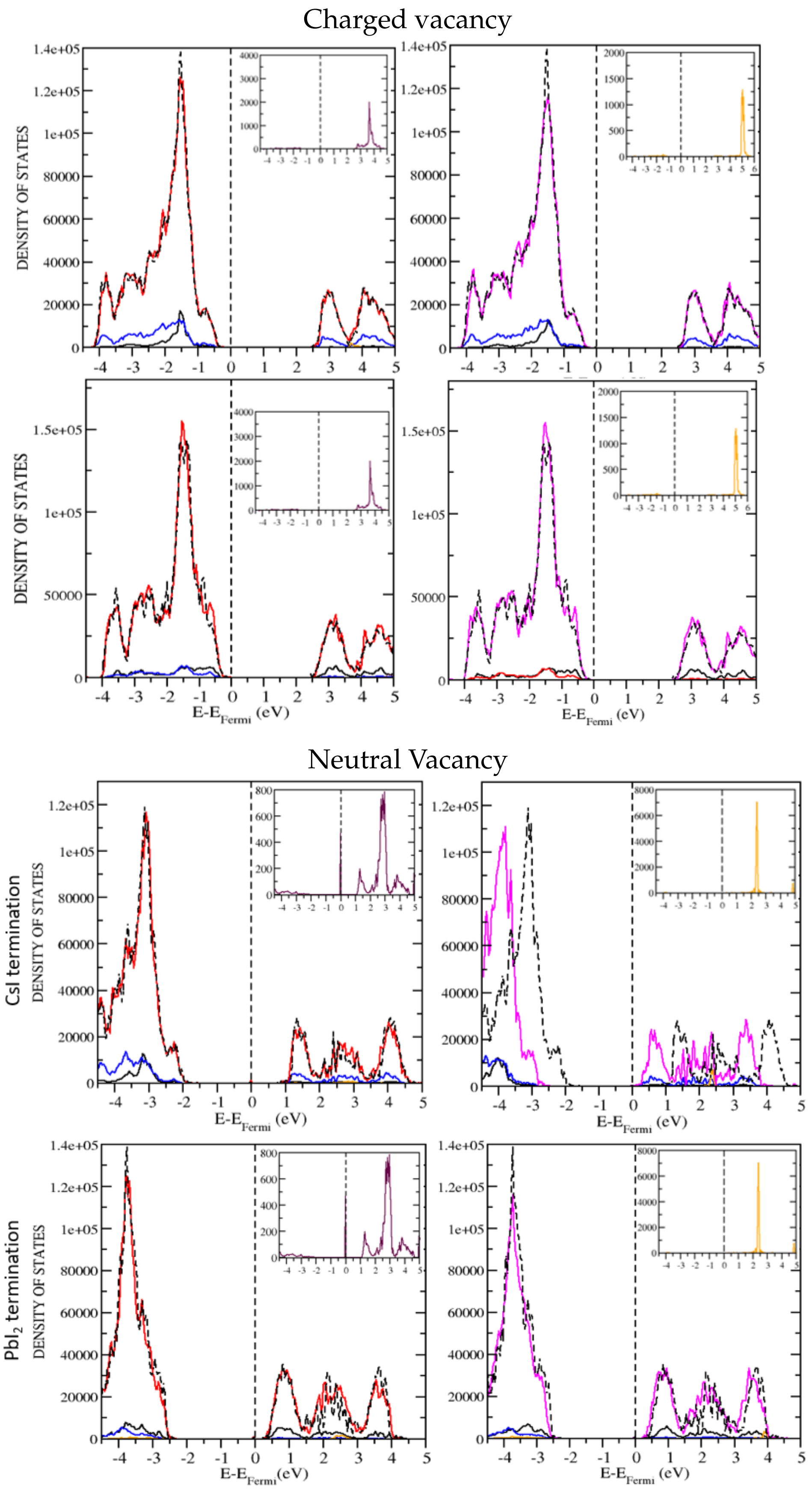

FIGURE 4.13: Total DOS of CO (left panel) and $CO_2$ (right panel) adsorbed on the CsI and $PbI_2$ terminated surfaces of $CsPbI_3$. The dashed line represents the total DOS of free surfaces. The black and blue line represents the DOS of the first and second layer, respectively. Inset shows the DOS of the corresponding molecule on the respective surface.

# Chapter 5

# Adsorption of oxygen and water on organic halide perovskite: MAPI

Methylammonium lead iodide (MAPI) is an organic perovskite widely used in PV. This chapter analyzes the degradation issue of MAPI under the influence of $O_2$ and $H_2O$ adsorbed on different surface types (001) and (110). The idea is to simulate the surface of MAPI exposed to ambient conditions.

Using the supercell of size 3×3 (like for $CsPbX_3$ surface) could be very demanding for the case of MAPI. 2×2 supercell of MAPI is equivalent to the size (in terms of length and breadth) of 3×3 $CsPbX_3$ supercell. In the case of MAPI, 2×2 supercell size, sufficiently large to separate the (periodic) adsorbed molecules, was used. The in-plane relaxation patterns of a 2×2 supercell are different from those of $CsPbX_3$ surfaces because of the presence of the larger-than-Cs size organic cation and different imposed symmetry constraints due to the choice of the size of the supercell. The two surfaces used, (001) and (110), offer two types of termination: (MA)I and $PbI_2$. The topmost layer of (110) surface have "kinks" and "steps" for surface with $PbI_2$ termination. The "kink" sites are most likely to be attacked by the molecules.

Unlike CsX terminated $CsPbX_3$ surface, (MA)I terminated surfaces do not provide multiple sites for adsorption due to the choice of the size of supercell. The choice of probable adsorption sites for molecules on these surfaces is done by literature research [Leijtens et al., 2017]. For the (MA)I termination, since the organic molecule (MA=$CH_3NH_3$) is easily attacked by $O_2$ and $H_2O$, the molecules are introduced over the organic cations. In the case of $PbI_2$ termination, molecules are placed over the Pb atom, which marks a kink site on the (110) surface, similar to the case for surfaces of

Cs-based perovskites.

## 5.1 Adsorption of $O_2$

For (110) and (001) surfaces with (MA)I termination, the MA molecules ($CH_3NH_3$) within the uppermost layer are oriented so that the carbon atom within the N–C bond points upwards. Oxygen is introduced over the MA molecule in a vertical orientation (similar to how it was tried in the case of inorganic halide perovskites) for (001) and (110) surfaces with MA orientation and over Pb for surfaces with $PbI_2$ termination.

For (110) surface with (MA)I termination, $O_2$ hangs over the MA molecule such that the C–O distance is around 3.5 Å, and from the nearest H the distance to $O_2$ is around 3 Å, as shown in Figure 5.1 (MAI termination, b). For $PbI_2$ termination, $O_2$ hangs over Pb (kink site) at a distance of around $\sim$3.5 Å in a tilted vertical orientation (see Figure 5.1, $PbI_2$ termination, b).

For (001) surface with (MA)I termination, the relaxed $O_2$ molecule ends up in tilted vertical orientation between the two I atoms and two MA atoms of (MA)I layer, at a distance of $\sim$4 Å as shown in Figure 5.2, (MA)I termination, the closest O–H distance between the $O_2$ and the MA molecules being $\simeq$3 Å (see Figure 5.2). There is a possibility that $O_2$ might dissociate and can form complexes with the organic molecule. In a dissociated state, the oxygen atom will lose its magnetic moment while interacting with the charges flowing within the solar cell. So, the dissociation of $O_2$ is simulated in a non-spin polarized manner (a priori $O_2$ ought to be treated spin-polarized and split into two atoms with magnetic moments). To simulate the reaction 5.1, one of the O atoms forming the $O_2$ molecule is placed near the Pb atom, and the other – close to a dissociated H atom of one of the MA molecules. The system is allowed to relax; the final configuration of the dissociated $O_2$ molecule is shown in Figure 5.3 a. The adsorption energy of $O_2$ undergoing a dissociation in the process is higher (stronger; $E_{ads}$ $-1$ eV) than that of a molecule remaining (and being adsorbed) intact ($E_{ads}$ $-0.03$ eV).

$$\mathrm{CH_3NH_3PbI_3 + O_2 \longrightarrow CH_2(OH)NH_3O^{+}I^{-}PbI_2} \quad . \tag{5.1}$$

At the (001) surface with $PbI_2$ termination, the $O_2$ molecule is docked in a tilted vertical orientation over the Pb atom, at a closest oxygen being at a distance of 3.52 Å (see Figure 5.3 a).

The adsorption energy of $O_2$ is roughly the same for all the MAPI surfaces (see Table 5.1) irrespective of the cutting plane orientation and the termination. Compared to the perfect and defective $CsPbX_3$ surfaces, the adsorption energy is almost three times lower (weaker).

## 5.2 Adsorption of $H_2O$

For (110) surface with (MA)I termination, $H_2O$ was introduced over the MA molecule such that O atom of $H_2O$ was pointing towards the C of MA. In the final configuration, as shown in Figure 5.1, $H_2O$ drifts towards the N part of the MA molecule. $H_2O$ hangs at a distance of ~1.5 Å from the H linked to N part of MA molecule, such that $H_2O$ is in between the the two iodine atoms situated on the (110) "ridge". For (110) surface

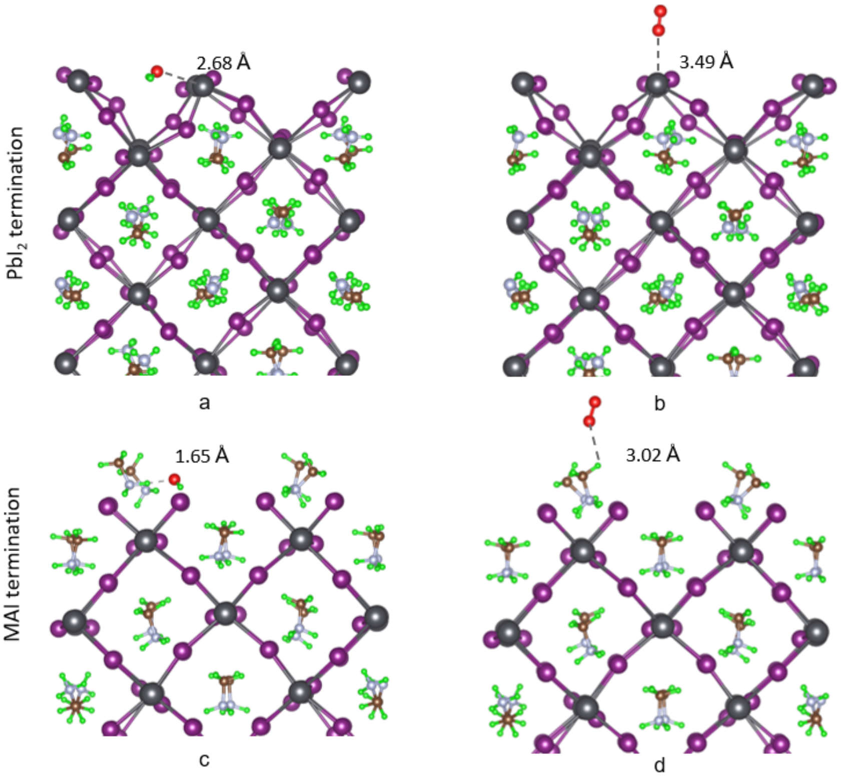

FIGURE 5.1: Final configurations of $O_2$ (b, d) and $H_2O$ (a, c) on MAPI (110) surface with $PbI_2$ (a, b) and (MA)I terminations (c, d).

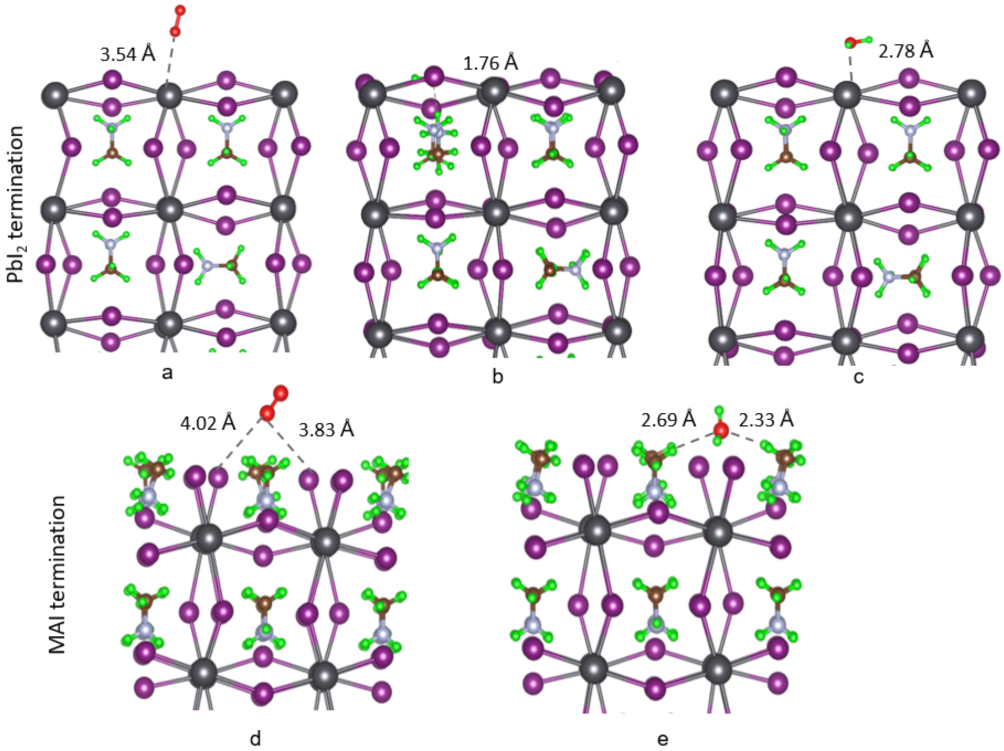

FIGURE 5.2: Final configuration of $O_2$ (a, d) and $H_2O$ (b, c and e) on MAPI (001) surface with $PbI_2$ (a, b, c) and (MA)I terminations (d, e).

TABLE 5.1: Adsorption Energy (in eV) calculated for the systems of $O_2$ and $H_2O$ molecules on the MAPI surfaces (110) and (001) with MAI and $PbI_2$ termination. $O_2$* and $H_2O$* are in the dissociated state. See text for details.

| Molecule | (110) surface | | (001) surface | |
|---|---|---|---|---|
| | MAI | $PbI_2$ | MAI | $PbI_2$ |
| $H_2O$ | −0.67 | −0.98 | −0.59 | −0.83 |
| $O_2$ | −0.03 | −0.03 | −0.04 | −0.04 |
| $O_2$* | | | −1.02 | |
| $H_2O$* | | | +1.61 | |

with $PbI_2$ termination, $H_2O$ is introduced over Pb such that the O atom from $H_2O$ is pointing towards Pb. In the final configuration, the H2O molecule comes to rest in between the "ridges" such that the O atom of $H_2O$ is at a distance of ∼2.68 Å, and the two H atoms are pointing down (see Figure 5.1 a).

For (001) (MA)I termination, again $H_2O$ is introduced over the MA molecule, and upon the full relaxation the $H_2O$ molecule finds its place between the two iodine

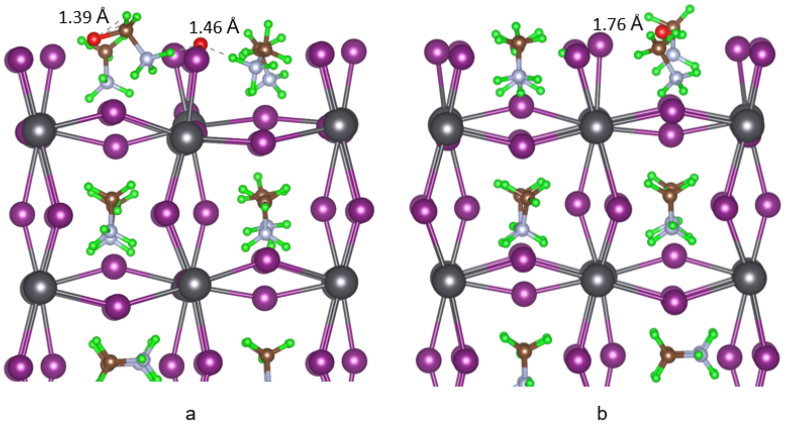

FIGURE 5.3: Relaxed configurations of dissociated $O_2$ (a) and $H_2O$ (b) on MAPI (001) surface with (MA)I termination.

atoms. The neighbouring MA molecule inclines with its $NH_3$ end towards the water molecule. The distance between the proton of the $H_2O$ molecule and H of the MA molecule is ~1.5 Å.

A possibility exists that $H_2O$ would dissociate into $H^+$ and $\mathrm{OH}^{\breve{}}$ and, in its dissociated form, would interact with perovskite. In its relaxed position, OH nearly maps onto the corresponding atoms of $H_2O$ in the absence of dissociation, and the proton finds its place close to one of the nearest-neighbour iodine atoms. The dissociated atoms (see Figure 5.3 b) arrange themselves such that the OH fragment borrows the H atoms from neighbouring MA molecule. The H atom goes closer towards the I atom, to a distance of ~1.6 Å, forming the ionic bond as confirmed by the Mulliken population analysis according to which the overlap occupation value (estimated partial atomic charge) between the H and I is 0.238 indicating the transfer of charges between H and I. ((For comparison, overlap occupation value between H and O in $H_2O$ is around 0.5). The adsorption energy of $H_2O$ in the dissociated state is around 1.62 eV, which is positive, indicating the adsorption in the dissociated state is not feasible.

$$\mathrm{CH_3NH_3PbI_3} + \mathrm{H^+OH^-} \longrightarrow \underset{\text{complex}}{\mathrm{CH_3NH_3PbI_3HOH}} \quad . \tag{5.2}$$

On the (001) surface with $PbI_2$ termination, $H_2O$ stabilises over the Pb, at a distance of 2.6 Å.

As another possibility, the $H_2O$ molecule can be stabilised over the MA molecule of the MA layer (the second one from the top). In the final configuration, $H_2O$ molecule ends up at the top of the cuboid formed by PbI units, forming a hydrogen bond of length 1.76 Å with $NH_3$ side of the MA molecule (see Figure 5.2b). The adsorption energy has a higher (absolute) value ($-0.89$ eV) than in other configurations (with $H_2O$ stabilised over the Pb atom of the uppermost $PbI_2$ layer).

The adsorption energies shown in Table 5.1 reveal higher adsorption energy of $H_2O$ on the (110) surface than on the (001) one. On the contrary, the adsorption energies of $O_2$ on these two surfaces are comparable. For both types of surface orientation, the adsorption of $H_2O$ is stronger in case of $PbI_2$ terminations than with (MA)I ones. However, in what regards the $O_2$ adsorption, both the (MA)I and $PbI_2$ terminations are energetically comparable for both types of surfaces. The adsorption energies reveal that the $O_2$ would more efficiently attack the perovskite in dissociated state. In the case of $H_2O$, non-dissociated $H_2O$ is more likely to attack the perovskite than the dissociated $H_2O$ (in the form H–OH). However, it is possible that water in the form of hydroxyl ion ($H_3O^+$) is more likely to interact with organic perovskite than $H_2O$ molecule. Further studies are needed to provide a firm conclusion regarding the interaction of water in the dissociated and undissociated state.

## 5.3 Electronic structure resulting from adsorption

For the MAPI, the density of states (DOS) structure is created for the (001) surface with (MA)I and $PbI_2$ termination. In Figure 5.4, for MAI termination, the total DOS of the pure surface and surface with $H_2O$ and $O_2$ are similar, indicating that the molecular interaction on the surface is not significant. In case of $O_2$ adsorbed on the $PbI_2$-terminated surface, one sees a little spike over the dominating DOS of the slab. Situated around $\simeq 1.4$ eV, this spike reveals a minority-spin level of oxygen around reveals a minority-spin level of oxygen which falls into the bandgap.

However, when the molecules are introduced in the dissociated form at the MAPI surface, the total DOS is shifted by $\simeq 0.2$ eV (see Figure 5.5), indicating the bond formation with dissociated species and the surface.

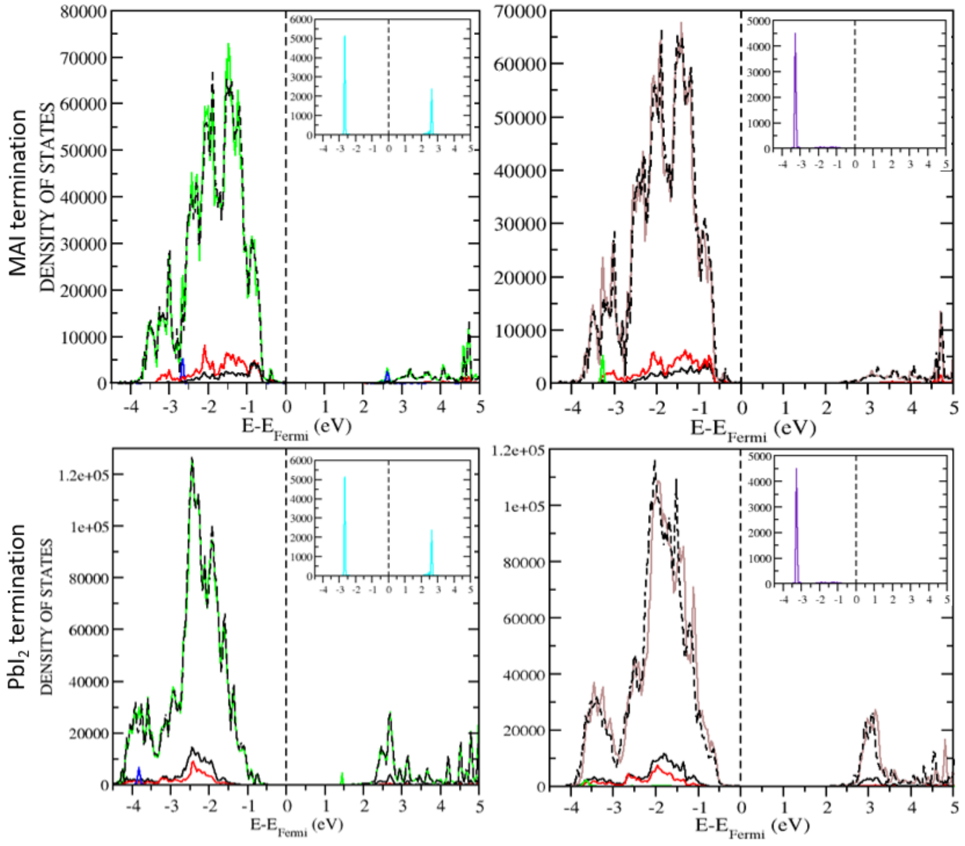

FIGURE 5.4: Densities of states of MAPI (001) surface with adsorbed $O_2$ (in the left panel) and $H_2O$ (on the right panel). Dashed lines indicate the total DOS of the whole slab without molecule. Black and red lines indicate the DOS of the first and the second layer, respectively. The inset shows the DOS of the corresponding molecule on that surface.

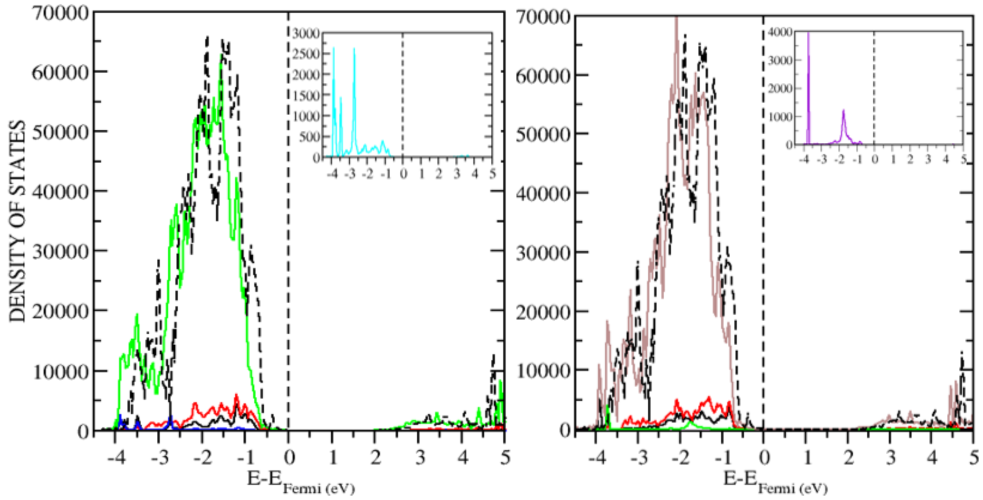

FIGURE 5.5: Densities of states of MAPI (001) surface with adsorbed $O_2$ (in the left panel) and $H_2O$ (on the right panel) in the dissociated state. Similar to figure 5.4. See text for details.

When the inorganic cation Cs in $CsPbX_3$ is replaced by (MA) cation, the interaction (change in adsorption energy) of oxygen in the undissociated state did not bring a tremendous change . But when $O_2$ is introduced in the dissociated state on top of (MA)PI, the adsorption energy is higher as compared to that of the undissociated state.

# Conclusions

This work focused on studying the bulk and surfaces of perovskites, under an angle of their degradation in ambient conditions. To this end, the interaction of molecules present in the air such as $CO_2$, CO, $O_2$ and $H_2O$ with the surfaces of cæsium and methylammonium–lead halides perovskites surfaces have been investigated at the first-principles level, aimed to understand and characterize the degradation in the performance of these perovskites for photovoltaic applications. A systematic study of the effects of molecules' adsorption on the electronic, structural and thermodynamic properties of $CsPbX_3$ (X = Cl, Br and I) and MAPI has been performed.

The calculations have been realized using a hybrid exchange-correlation functional combining Hartree-Fock exchange with PBEsol (for $CsPbX_3$ type perovskite) and PBE (for MAPI and FAPI) exchange-correlation, optimized to yield a qualitatively correct and quantitatively accurate description of the structural, electronic and dynamic properties, in agreement with experiment.

The simulation of clean surfaces (of perovskite slabs, with two different terminations), done as a preliminary step in the study of adsorption, resulted in conclusions that might be of their own interest, concerning the relaxation at the surface and the discrimination between possible adsorption sites, which revealed a manifestation of inherent dynamical instabilities frozen at the surface, within the cubic perovskite phase. Such discrimination (creation of the sites of markedly different morphology) is much more pronounced at the CsX surface than at the $PbX_2$ one, the latter being more "regular" despite its considerable "warping".
For the surfaces of FAPI, the orientation of the FA molecule plays an essential role in defining the surface stability; further studies are needed in this regard.

The inclusion of vacancies at the perfect surfaces does not significantly change the relaxation pattern.

Regarding the energies and comparing the surfaces, $CO_2$ exhibits stronger adsorption on the CsX-terminated slabs than on the $PbX_2$-terminated ones, whereas for CO and $O_2$, the tendencies are comparable for both types of termination. Comparing the molecules on the CsX-terminated surfaces, $CO_2$ has more stronger interaction to the surface than CO and $O_2$, which latter reveals the least appreciable adsorption energy among all molecules studied on complete (free of vacancies) surfaces. The adsorption energies of $O_2$ are in fact below the threshold of reasonably expected accuracy.

In case the surface possesses a charged halogen vacancy, the interaction of molecules with it was not substantially enhanced compared to the case of the perfect surface. However, for the surface with neutral vacancies, the interaction of $CO_2$ and $H_2O$ shows a considerable increase compared to that of the perfect surface. For the surfaces with charged vacancy, $H_2O$ is more prominent to attack the surface, while for the surfaces with neutral vacancy, $O_2$ is more likely to attack than other molecules used in this study.

For MAPI, $H_2O$ is more likely to interact with the surface than oxygen, revealing $PbI_2$ termination as the surface with the highest interaction in terms of adsorption energy. MAPI surface is more likely to be attacked by oxygen in the dissociated form (O-O). At the same time, for water molecules, the non-dissociated molecule is more likely to attack than the dissociated form ($H^+$ and $OH^-$).

The presence of molecules does not significantly impact the electronic structure of the perfect $CsPbX_3$ surfaces and surfaces with charged vacancies, whatever the perovskites, types of surfaces and molecules.

The analysis of the characteristics of adsorption (moderate values of adsorption energies, a relative absence of chemical bonding between molecules and the slabs) permits us to identify their interaction as physisorption for the case of perfect surfaces ($CsPbX_3$ and MAPI) and surfaces ($CsPbX_3$) with charged vacancy. However, for the surface with neutral vacancy, we can speak of chemisorption with more substantial confidence, at least in case adsorbed $O_2$ and $CO_2$ occurs.

A practical consequence from this consideration is that CO and $O_2$ (and, in fact,

$CO_2$ as well) are not likely to stick to the perovskite surface to produce any damaging effect to the perfect $CsPbX_3$ surface. However, $CsPbX_3$ surface with a neutral vacancy can bring damaging effects by the attack of $O_2$ and $CO_2$. While for the case of MAPI, $O_2$ is more prominent to attack in the dissociated state while $H_2O$ in the dissociated state ($H^+$ and $OH^-$) is less likely to attack as compared to the non-dissociated state. However, more configurations of dissociation of $H_2O$ are needed to be tested to understand the attack of a water molecule on perovskites in a dissociated state. In this work, the subsequent studies must explore the combined action of molecules and temperature.

# Bibliography

Nrel. https://www.nrel.gov/pv/cell-efficiency.html. Accessed: 2021-01-30.

Variational basis sets are available at the following web site http://www.crystal.unito.it/basis-sets.php.

Abate, A., Leijtens, T., Pathak, S., Teuscher, J., Avolio, R., Errico, M. E., Kirkpatrik, J., Ball, J. M., Docampo, P., McPherson, I., and Snaith, H. J. Lithium salts as redox active p-type dopants for organic semiconductors and their impact in solid-state dye-sensitized solar cells. *Phys. Chem. Chem. Phys.*, 15:2572–2579, 2013. doi: 10.1039/C2CP44397J. URL http://dx.doi.org/10.1039/C2CP44397J.

Abdelmageed, G., Sully, H. R., Bonabi Naghadeh, S., El-Hag Ali, A., Carter, S. A., and Zhang, J. Z. Improved stability of organometal halide perovskite films and solar cells toward humidity via surface passivation with oleic acid. *ACS Applied Energy Materials*, 1(2):387–392, 2018. doi: 10.1021/acsaem.7b00069. URL https://doi.org/10.1021/acsaem.7b00069.

Adamo, C., Scuseria, G. E., and Barone, V. Accurate excitation energies from time-dependent density functional theory: Assessing the PBE0 model. *The Journal of Chemical Physics*, 111(7):2889–2899, 1999. doi: 10.1063/1.479571. URL https://doi.org/10.1063/1.479571.

Akhtar, J., Aamir, M., and Sher, M. Chapter 2 - organometal lead halide perovskite. In Thomas, S. and Thankappan, A., editors, *Perovskite Photovoltaics*, pages 25–42. Academic Press, 2018. ISBN 978-0-12-812915-9. doi: https://doi.org/10.1016/B978-0-12-812915-9.00002-2. URL https://www.sciencedirect.com/science/article/pii/B9780128129159000022.

Anaraki, E. H., Kermanpur, A., Steier, L., Domanski, K., Matsui, T., Tress, W., Saliba, M., Abate, A., Grätzel, M., Hagfeldt, A., and Correa-Baena, J.-P. Highly efficient and stable planar perovskite solar cells by solution-processed tin oxide. *Energy Environ. Sci.*, 9:3128–3134, 2016. doi: 10.1039/C6EE02390H. URL `http://dx.doi.org/10.1039/C6EE02390H`.

Andrae, D., Häußermann, U., Dolg, M., Stoll, H., and Preuß, H. Energy-adjusted *ab initio* pseudopotentials for the second and third row transition elements. *Theoretica chimica acta*, 77(2):123–141, Mar 1990. ISSN 1432-2234. doi: 10.1007/BF01114537. URL `https://doi.org/10.1007/BF01114537`.

Apra, E., Causa, M., Prencipe, M., Dovesi, R., and Saunders, V. On the structural properties of NaCl. an ab initio study of the B1-B2 phase transition. *J. Phys. Condens. Matter*, 5:2969 – 2976, 1993. URL `https://doi.org/10.1088/0953-8984/5/18/019`.

Aristidou, N., Eames, C., Sanchez-Molina, I., Bu, X., Kosco, J., Islam, M. S., and Haque, S. A. Fast oxygen diffusion and iodide defects mediate oxygen-induced degradation of perovskite solar cells. *Nature Communications*, 8(1):15218, May 2017. ISSN 2041-1723. doi: 10.1038/ncomms15218. URL `https://doi.org/10.1038/ncomms15218`.

Azpiroz, J. M., Mosconi, E., Bisquert, J., and De Angelis, F. Defect migration in methylammonium lead iodide and its role in perovskite solar cell operation. *Energy Environ. Sci.*, 8:2118–2127, 2015. doi: 10.1039/C5EE01265A. URL `http://dx.doi.org/10.1039/C5EE01265A`.

Ball, J. M. and Petrozza, A. Defects in perovskite-halides and their effects in solar cells. *Nature Energy*, 1(11):16149, Oct 2016. ISSN 2058-7546. doi: 10.1038/nenergy.2016.149. URL `https://doi.org/10.1038/nenergy.2016.149`.

Baranek, P. *Private communication*, 2019.

Becke, A. D. A new mixing of Hartree–Fock and local density-functional theories. *The Journal of Chemical Physics*, 98(2):1372–1377, 1993. doi: 10.1063/1.464304. URL `https://doi.org/10.1063/1.464304`.

Becke, A. D. Perspective: Fifty years of density-functional theory in chemical physics. *The Journal of Chemical Physics*, 140(18):18A301, 2014. doi: 10.1063/1.4869598. URL `https://doi.org/10.1063/1.4869598`.

Besalú, E. and Carbó-Dorca, R. The general Gaussian product theorem. *Journal of Mathematical Chemistry*, 49(8):1769–1784, Sep 2011. ISSN 1572-8897. doi: 10.1007/s10910-011-9857-9. URL `https://doi.org/10.1007/s10910-011-9857-9`.

Born, M. and Oppenheimer, R. Zur Quantentheorie der Molekeln. *Annalen der Physik*, 389(20):457–484, 1927. doi: https://doi.org/10.1002/andp.19273892002. URL `https://onlinelibrary.wiley.com/doi/abs/10.1002/andp.19273892002`.

Boys, S. and Bernardi, F. The calculation of small molecular interactions by the differences of separate total energies. Some procedures with reduced errors. *Molecular Physics*, 19(4):553–566, 1970. doi: 10.1080/00268977000101561. URL `https://doi.org/10.1080/00268977000101561`.

Brandt, R. E., Stevanovi, V., Ginley, D. S., and Buonassisi, T. Identifying defect-tolerant semiconductors with high minority-carrier lifetimes: beyond hybrid lead halide perovskites. *MRS Communications*, 5(2):265–275, 2015. doi: 10.1557/mrc.2015.26.

Brivio, F., Frost, J., Skelton, J., Jackson, A., Weber, O., Weller, M., Goñi, A., Leguy, A., Barnes, P., and Walsh, A. Lattice dynamics and vibrational spectra of the orthorhombic, tetragonal and cubic phases of methylammonium lead iodide. *Physical Review B*, 92:144308, 10 2015. doi: 10.1103/PhysRevB.92.144308.

Bryant, D., Aristidou, N., Pont, S., Sanchez-Molina, I., Chotchunangatchaval, T., Wheeler, S., Durrant, J. R., and Haque, S. A. Light and oxygen induced degradation limits the operational stability of methylammonium lead triiodide perovskite solar cells. *Energy Environ. Sci.*, 9:1655–1660, 2016. doi: 10.1039/C6EE00409A. URL http://dx.doi.org/10.1039/C6EE00409A.

Bush, K. A., Palmstrom, A. F., Yu, Z. J., Boccard, M., Cheacharoen, R., Mailoa, J. P., McMeekin, D. P., Hoye, R. L. Z., Bailie, C. D., Leijtens, T., Peters, I. M., Minichetti, M. C., Rolston, N., Prasanna, R., Sofia, S., Harwood, D., Ma, W., Moghadam, F., Snaith, H. J., Buonassisi, T., Holman, Z. C., Bent, S. F., and McGehee, M. D. 23.6%-efficient monolithic perovskite/silicon tandem solar cells with improved stability. *Nature Energy*, 2(4):17009, Feb 2017. ISSN 2058-7546. doi: 10.1038/nenergy.2017.9. URL https://doi.org/10.1038/nenergy.2017.9.

Bussmann-Holder, A., Büttner, H., and Bishop, A. R. Stabilization of ferroelectricity in quantum paraelectrics by isotopic substitution. *Journal of Physics: Condensed Matter*, 12(6):L115–L120, jan 2000. doi: 10.1088/0953-8984/12/6/108. URL https://doi.org/10.1088/0953-8984/12/6/108.

Caddeo, C., Saba, M. I., Meloni, S., Filippetti, A., and Mattoni, A. Collective molecular mechanisms in the $CH_3NH_3PbI_3$ dissolution by liquid water. *ACS Nano*, 11(9):9183–9190, 2017. doi: 10.1021/acsnano.7b04116. URL https://doi.org/10.1021/acsnano.7b04116. PMID: 28783296.

Capitani, J. F., Nalewajski, R. F., and Parr, R. G. Non-Born–Oppenheimer density functional theory of molecular systems. *The Journal of Chemical Physics*, 76(1):568–573, 1982. doi: 10.1063/1.442703. URL https://doi.org/10.1063/1.442703.

Cappel, U. B., Daeneke, T., and Bach, U. Oxygen-induced doping of spiro-meotad in solid-state dye-sensitized solar cells and its impact on device performance. *Nano Letters*, 12(9):4925–4931, 2012. doi: 10.1021/nl302509q. URL https://doi.org/10.1021/nl302509q. PMID: 22913390.

Carignano, M. A., Saeed, Y., Aravindh, S. A., Roqan, I. S., Even, J., and Katan, C. A close examination of the structure and dynamics of $HC(NH_2)_2PbI_3$ by MD simulations and group theory. *Phys. Chem. Chem. Phys.*, 18:27109–27118, 2016. doi: 10.1039/C6CP02917E. URL http://dx.doi.org/10.1039/C6CP02917E.

Christians, J. A., Miranda Herrera, P. A., and Kamat, P. V. Transformation of the excited state and photovoltaic efficiency of $CH_3NH_3PbI_3$ perovskite upon controlled exposure to humidified air. *Journal of the American Chemical Society*, 137(4):1530–1538, 2015. doi: 10.1021/ja511132a. URL https://doi.org/10.1021/ja511132a. PMID: 25590693.

Corkish, R. Solar cells. In Cleveland, C. J., editor, *Encyclopedia of Energy*, pages 545–557. Elsevier, New York, 2004. ISBN 978-0-12-176480-7. doi: https://doi.org/10.1016/B0-12-176480-X/00328-4. URL https://www.sciencedirect.com/science/article/pii/B012176480X003284.

Dittrich, T., Lang, F., Shargaieva, O., Rappich, J., Nickel, N. H., Unger, E., and Rech, B. Diffusion length of photo-generated charge carriers in layers and powders of $CH_3NH_3PbI_3$ perovskite. *Applied Physics Letters*, 109(7):073901, 2016. doi: 10.1063/1.4960641. URL https://doi.org/10.1063/1.4960641.

Dolg, M. Chapter 14 - relativistic effective core potentials. In Schwerdtfeger, P., editor, *Relativistic Electronic Structure Theory*, volume 11 of *Theoretical and Computational Chemistry*, pages 793–862. Elsevier, 2002. doi: https://doi.org/10.1016/S1380-7323(02)80040-1. URL https://www.sciencedirect.com/science/article/pii/S1380732302800401.

Dovesi, R., Pisani, C., Roetti, C., Causa, M., and Saunders, V. CRYSTAL88, an ab initio all-electron LCAO-Hartree-Fock program for periodic systems. *QCPE Pgm*, (577), 1988.

Dovesi, R., Causa, M., Orlando, R., Roetti, C., and Saunders, V. R. *Ab initio* approach to molecular crystals: A periodic hartree–fock study of crystalline urea. *J. Chem. Phys.*, 92:7402, 1990.

Dovesi, R., Saunders, V. R., Roetti, C., Orlando, R., Zicovich-Wilson, C. M., Pascale, F., Civalleri, B., Doll, K., Harrison, N. M., Bush, I. J., D'Arco, P., Llunell, M., Causà, M., Noël, Y., Maschio, L., Erba, A., Rerat, M., and Casassa, S. *CRYSTAL17 User's Manual (University of Torino, Torino, 2017).* University of Torino, Torino,, 2017.

Dovesi, R., Erba, A., Orlando, R., Zicovich-Wilson, C. M., Civalleri, B., Maschio, L., Rérat, M., Casassa, S., Baima, J., Salustro, S., and Kirtman, B. Quantum-mechanical condensed matter simulations with CRYSTAL. *WIREs Computational Molecular Science*, 8(4):e1360, 2018. doi: 10.1002/wcms.1360. URL `https://onlinelibrary.wiley.com/doi/abs/10.1002/wcms.1360`.

Du, M. H. Efficient carrier transport in halide perovskites: theoretical perspectives. *J. Mater. Chem. A*, 2:9091–9098, 2014. doi: 10.1039/C4TA01198H. URL `http://dx.doi.org/10.1039/C4TA01198H`.

Du, Q. G., Shen, G., and John, S. Light-trapping in perovskite solar cells. *AIP Advances*, 6(6):065002, 2016. doi: 10.1063/1.4953336. URL `https://doi.org/10.1063/1.4953336`.

Durand, P. and Barthelat, J.-C. A theoretical method to determine atomic pseudopotentials for electronic structure calculations of molecules and solids. *Theoretica chimica acta*, 38(4):283–302, Dec 1975. ISSN 1432-2234. doi: 10.1007/BF00963468. URL `https://doi.org/10.1007/BF00963468`.

Eames, C., Frost, J. M., Barnes, P. R. F., O'Regan, B. C., Walsh, A., and Islam, M. S. Ionic transport in hybrid lead iodide perovskite solar cells. *Nature Communications*, 6(1):7497, Jun 2015. ISSN 2041-1723. doi: 10.1038/ncomms8497. URL `https://doi.org/10.1038/ncomms8497`.

Ebenhoch, B., Thomson, S. A., Genevičius, K., Juška, G., and Samuel, I. D. Charge carrier mobility of the organic photovoltaic materials PTB7 and $PC_{71}BM$ and its influence on device performance. *Organic Electronics*, 22:62–68, 2015. ISSN 1566-1199. doi: https://doi.org/10.1016/j.orgel.2015.03.013. URL `https://www.sciencedirect.com/science/article/pii/S1566119915001044`.

Eglitis, R. I. and Vanderbilt, D. Ab initio calculations of $BaTiO_3$ and $PbTiO_3$ (001) and (011) surface structures. *Phys. Rev. B*, 76:155439, Oct 2007. doi: 10.1103/PhysRevB.76.155439. URL `https://link.aps.org/doi/10.1103/PhysRevB.76.155439`.

Eperon, G. E., Stranks, S. D., Menelaou, C., Johnston, M. B., Herz, L. M., and Snaith, H. J. Formamidinium lead trihalide: a broadly tunable perovskite for efficient planar heterojunction solar cells. *Energy Environ. Sci.*, 7:982–988, 2014. doi: 10.1039/C3EE43822H. URL `http://dx.doi.org/10.1039/C3EE43822H`.

Eperon, G. E., Paternò, G. M., Sutton, R. J., Zampetti, A., Haghighirad, A. A., Cacialli, F., and Snaith, H. J. Inorganic caesium lead iodide perovskite solar cells. *J. Mater. Chem. A*, 3:19688–19695, 2015. doi: 10.1039/C5TA06398A. URL `http://dx.doi.org/10.1039/C5TA06398A`.

Ernzerhof, M. and Scuseria, G. E. Assessment of the Perdew–Burke–Ernzerhof exchange-correlation functional. *The Journal of Chemical Physics*, 110(11):5029–5036, 1999. doi: 10.1063/1.478401. URL `https://doi.org/10.1063/1.478401`.

Fermi, E. Un metodo statistico per la determinazione di alcune priopriet à dell'atomo. *Rendiconti Academia Dei Lincei*, 6:602–607, 1927.

Fischer, M. *Environmental Biology*, chapter 11. Open Oregon Educational Resources, 1999. ISBN 978-1-63635-036-3. doi: 10.1002/9780470166499.ch1. URL `https://openoregon.pressbooks.pub/envirobiology/`.

Fock, V. Näherungsmethode zur Lösung des quantenmechanischen Mehrkörperproblems. *Zeitschrift für Physik*, 61(1):126–148, Jan 1930. ISSN 0044-3328. doi: 10.1007/BF01340294. URL `https://doi.org/10.1007/BF01340294`.

Goldschmidt, V. M. Die Gesetze der Krystallochemie. *Naturwissenschaften*, 14(21):477–485, May 1926. ISSN 1432-1904. doi: 10.1007/BF01507527. URL `https://doi.org/10.1007/BF01507527`.

Grancini, G., Roldán-Carmona, C., Zimmermann, I., Mosconi, E., Lee, X., Martineau, D., Narbey, S., Oswald, F., De Angelis, F., Graetzel, M., and Nazeeruddin, M. K. One-year stable perovskite solar cells by 2d/3d interface engineering. *Nature Communications*, 8(1):15684, Jun 2017. ISSN 2041-1723. doi: 10.1038/ncomms15684. URL `https://doi.org/10.1038/ncomms15684`.

Groß, A. *Electronic Structure Methods and Total Energies*, pages 21–58. Springer Berlin Heidelberg, Berlin, Heidelberg, 2009. ISBN 978-3-540-68969-0. doi: 10.1007/978-3-540-68969-0_3. URL `https://doi.org/10.1007/978-3-540-68969-0_3`.

Guarnieri, M. More light on information [historical]. *IEEE Industrial Electronics Magazine*, 9(4):58–61, 2015. doi: 10.1109/MIE.2015.2485182.

Habisreutinger, S. N., Leijtens, T., Eperon, G. E., Stranks, S. D., Nicholas, R. J., and Snaith, H. J. Carbon nanotube/polymer composites as a highly stable hole collection layer in perovskite solar cells. *Nano Letters*, 14(10):5561–5568, 2014. doi: 10.1021/nl501982b. URL `https://doi.org/10.1021/nl501982b`. PMID: 25226226.

Han, Y., Meyer, S., Dkhissi, Y., Weber, K., Pringle, J. M., Bach, U., Spiccia, L., and Cheng, Y.-B. Degradation observations of encapsulated planar $CH_3NH_3PbI_3$ perovskite solar cells at high temperatures and humidity. *J. Mater. Chem. A*, 3:8139–8147, 2015. doi: 10.1039/C5TA00358J. URL `http://dx.doi.org/10.1039/C5TA00358J`.

Hartree, D. R. The wave mechanics of an atom with a non-coulomb central field. part i. theory and methods. *Mathematical Proceedings of the Cambridge Philosophical Society*, 24(1):89–110, 1928. doi: 10.1017/S0305004100011919.

Hay, P. J. and Wadt, W. R. Ab initio effective core potentials for molecular calculations. Potentials for transition metal atoms Sc to Hg. *J. Chem. Phys.*, 82:270, 1985a.

Hay, P. J. and Wadt, W. R. Ab initio effective core potentials for molecular calculations. Potentials for main group elements Na to Bi. *J. Chem. Phys.*, 82:284, 1985b.

Hay, P. J. and Wadt, W. R. Ab initio effective core potentials for molecular calculations. Potentials for K to Au including the outermost orbitals. *J. Chem. Phys.*, 82:299, 1985c.

Hay, P. J. and Wadt, W. R. Ab initio effective core potentials for molecular calculations. Potentials for the transition metal atoms Sc to Hg. *The Journal of Chemical Physics*, 82(1):270–283, 1985d. doi: 10.1063/1.448799. URL `https://doi.org/10.1063/1.448799`.

Heo, J. H., Im, S. H., Noh, J. H., Mandal, T. N., Lim, C.-S., Chang, J. A., Lee, Y. H., Kim, H.-j., Sarkar, A., Nazeeruddin, M. K., Grätzel, M., and Seok, S. I. Efficient inorganic-organic hybrid heterojunction solar cells containing perovskite compound and polymeric hole conductors. *Nature Photonics*, 7(6):486–491, Jun 2013. ISSN 1749-4893. doi: 10.1038/nphoton.2013.80. URL `https://doi.org/10.1038/nphoton.2013.80`.

Hestenes, M. and Stiefel, E. Methods of conjugate gradients for solving linear systems. *J. Res. Natl. Bur. Stand.*, 49:409–436, 1952.

Heyd, J., Scuseria, G. E., and Ernzerhof, M. Hybrid functionals based on a screened Coulomb potential. *The Journal of Chemical Physics*, 118(18):8207–8215, 2003. doi: 10.1063/1.1564060. URL `https://doi.org/10.1063/1.1564060`.

Hohenberg, P. and Kohn, W. Inhomogeneous electron gas. *Phys. Rev.*, 136:B864–B871, Nov 1964. doi: 10.1103/PhysRev.136.B864. URL `https://link.aps.org/doi/10.1103/PhysRev.136.B864`.

Huang, W., Manser, J. S., Kamat, P. V., and Ptasinska, S. Evolution of chemical composition, morphology, and photovoltaic efficiency of $CH_3NH_3PbI_3$ perovskite under ambient conditions. *Chemistry of Materials*, 28(1):303–311, 2016. doi: 10.1021/acs.chemmater.5b04122. URL `https://doi.org/10.1021/acs.chemmater.5b04122`.

Jain, A., Ong, S. P., Hautier, G., Chen, W., Richards, W. D., Dacek, S., Cholia, S., Gunter, D., Skinner, D., Ceder, G., and Persson, K. a. Commentary: The Materials Project: A materials genome approach to accelerating materials innovation. *APL Materials*, 1(1):011002, 2013. ISSN 2166532X. doi: 10.1063/1.4812323. URL `https://doi.org/10.1063/1.4812323`.

Janak, J. F. Proof that $\frac{\partial e}{\partial n_i} = \epsilon$ in density-functional theory. *Phys. Rev. B*, 18:7165–7168, Dec 1978. doi: 10.1103/PhysRevB.18.7165. URL `https://link.aps.org/doi/10.1103/PhysRevB.18.7165`.

Janesko, B. G. Replacing hybrid density functional theory: motivation and recent advances. *Chem. Soc. Rev.*, 50:8470–8495, 2021. doi: 10.1039/D0CS01074J. URL http://dx.doi.org/10.1039/D0CS01074J.

Jiang, C., Wang, Y., Zhou, R., Wang, H., and Chen, Q. Air molecules in $XPbI_3$ (X=MA, FA, Cs) perovskites: A degradation mechanism based on first-principles. *Journal of Applied Physics*, 124:085105, 2018.

Jiang, Q., Rebollar, D., Gong, J., Piacentino, E. L., Zheng, C., and Xu, T. Pseudohalide-induced moisture tolerance in perovskite $CH_3NH_3Pb(SCN)_2I$ thin films. *Angewandte Chemie International Edition*, 54(26):7617–7620, 2015. doi: 10.1002/anie.201503038. URL https://onlinelibrary.wiley.com/doi/abs/10.1002/anie.201503038.

Jones, R. O. Density functional theory: Its origins, rise to prominence, and future. *Rev. Mod. Phys.*, 87:897–923, Aug 2015. doi: 10.1103/RevModPhys.87.897. URL https://link.aps.org/doi/10.1103/RevModPhys.87.897.

Jong, U.-G., Yu, C.-J., Ri, G.-C., McMahon, A. P., Harrison, N. M., Barnes, P. R. F., and Walsh, A. Influence of water intercalation and hydration on chemical decomposition and ion transport in methylammonium lead halide perovskites. *J. Mater. Chem. A*, 6:1067–1074, 2018. doi: 10.1039/C7TA09112E. URL http://dx.doi.org/10.1039/C7TA09112E.

Juarez-Perez, E. J., Hawash, Z., Raga, S. R., Ono, L. K., and Qi, Y. Thermal degradation of $CH_3NH_3PbI{+}3$ perovskite into $NH_3$ and $CH_3I$ gases observed by coupled thermogravimetry–mass spectrometry analysis. *Energy Environ. Sci.*, 9:3406–3410, 2016. doi: 10.1039/C6EE02016J. URL http://dx.doi.org/10.1039/C6EE02016J.

Kajal, P., Ghosh, K., and Powar, S. *Manufacturing Techniques of Perovskite Solar Cells*, pages 341–364. 01 2018. ISBN 978-981-10-7205-5. doi: 10.1007/978-981-10-7206-2_16.

Kim, G.-W., Kang, G., Kim, J., Lee, G.-Y., Kim, H. I., Pyeon, L., Lee, J., and Park, T. Dopant-free polymeric hole transport materials for highly efficient and stable perovskite solar cells. *Energy Environ. Sci.*, 9:2326–2333, 2016. doi: 10.1039/C6EE00709K. URL `http://dx.doi.org/10.1039/C6EE00709K`.

Kim, G.-W., Kang, G., Malekshahi Byranvand, M., Lee, G.-Y., and Park, T. Gradated mixed hole transport layer in a perovskite solar cell: Improving moisture stability and efficiency. *ACS Applied Materials & Interfaces*, 9(33):27720–27726, 2017. doi: 10.1021/acsami.7b07071. URL `https://doi.org/10.1021/acsami.7b07071`. PMID: 28762266.

Kim, H., Lee, J., Kim, B., Byun, H. R., Kim, S. H., Oh, H. M., Baik, S., and Jeong, M. S. Enhanced stability of $MAPbI_3$ perovskite solar cells using poly(p-chloro-xylylene) encapsulation. *Scientific Reports*, 9(1):15461, Oct 2019. ISSN 2045-2322. doi: 10.1038/s41598-019-51945-9. URL `https://doi.org/10.1038/s41598-019-51945-9`.

Kim, J., Lee, S.-H., Lee, J. H., and Hong, K.-H. The role of intrinsic defects in methylammonium lead iodide perovskite. *The Journal of Physical Chemistry Letters*, 5(8): 1312–1317, 2014. doi: 10.1021/jz500370k. URL `https://doi.org/10.1021/jz500370k`. PMID: 26269973.

Kohn, W. Nobel lecture: Electronic structure of matter—wave functions and density functionals. *Rev. Mod. Phys.*, 71:1253–1266, Oct 1999. doi: 10.1103/RevModPhys.71.1253. URL `https://link.aps.org/doi/10.1103/RevModPhys.71.1253`.

Kohn, W. and Sham, L. J. Self-consistent equations including exchange and correlation effects. *Phys. Rev.*, 140:A1133–A1138, Nov 1965. doi: 10.1103/PhysRev.140.A1133. URL `https://link.aps.org/doi/10.1103/PhysRev.140.A1133`.

Kojima, A., Teshima, K., Shirai, Y., and Miyasaka, T. Organometal halide perovskites as visible-light sensitizers for photovoltaic cells. *Journal of the American Chemical Society*, 131(17):6050–6051, 2009. doi: 10.1021/ja809598r. URL `https://doi.org/10.1021/ja809598r`. PMID: 19366264.

Kolafa, J. and Perram, J. W. Cutoff errors in the Ewald summation formulae for point charge systems. *Molecular Simulation*, 9(5):351–368, 1992. doi: 10.1080/08927029208049126. URL `https://doi.org/10.1080/08927029208049126`.

Koopmans, T. Über die Zuordnung von Wellenfunktionen und Eigenwerten zu den Einzelnen Elektronen Eines Atoms. *Physica*, 1(1):104 – 113, 1934. ISSN 0031-8914. doi: https://doi.org/10.1016/S0031-8914(34)90011-2. URL `http://www.sciencedirect.com/science/article/pii/S0031891434900112`.

Koushik, D., Verhees, W. J. H., Kuang, Y., Veenstra, S., Zhang, D., Verheijen, M. A., Creatore, M., and Schropp, R. E. I. High-efficiency humidity-stable planar perovskite solar cells based on atomic layer architecture. *Energy Environ. Sci.*, 10:91–100, 2017. doi: 10.1039/C6EE02687G. URL `http://dx.doi.org/10.1039/C6EE02687G`.

Lafond, F. *Hybrid functionals approach for the study of the properties of complex materials for photovoltaic applications*. PhD thesis, 2019. URL `http://www.theses.fr/2019LORR0308`. These de doctorat dirigée par Postnikov, Andreï Physique University de Lorraine 2019.

Lai, M., Kong, Q., Bischak, C. G., Yu, Y., Dou, L., Eaton, S. W., Ginsberg, N. S., and Yang, P. Structural, optical, and electrical properties of phase-controlled cesium lead iodide nanowires. *Nano Research*, 10:1107–1114, Apr 2017. doi: 10.1007/s12274-016-1415-0. URL `https://doi.org/10.1007/s12274-016-1415-0`.

Lan, C., Zhou, Z., Wei, R., and Ho, J. C. Two-dimensional perovskite materials: From synthesis to energy-related applications. *Materials Today Energy*, 11:61–82, 2019. ISSN 2468-6069. doi: https://doi.org/10.1016/j.mtener.2018.10.008. URL `https://www.sciencedirect.com/science/article/pii/S2468606918302399`.

Leblanc, A., Mercier, N., Allain, M., Dittmer, J., Pauporté, T., Fernandez, V., Boucher, F., Kepenekian, M., and Katan, C. Enhanced stability and band gap tuning of $\alpha$-$[HC(NH_2)_2]PbI_3$ hybrid perovskite by large cation integration. *ACS Applied Materials & Interfaces*, 11(23):20743–20751, 2019. doi: 10.1021/acsami.9b00210. URL `https://doi.org/10.1021/acsami.9b00210`.

Leguy, A. M. A., Frost, J. M., McMahon, A. P., Sakai, V. G., Kockelmann, W., Law, C., Li, X., Foglia, F., Walsh, A., O'Regan, B. C., Nelson, J., Cabral, J. T., and Barnes, P. R. F. The dynamics of methylammonium ions in hybrid organic–inorganic perovskite solar cells. *Nature Communications*, 6(1):7124, May 2015. ISSN 2041-1723. doi: 10.1038/ncomms8124. URL `https://doi.org/10.1038/ncomms8124`.

Lei, Y., Xu, Y., Wang, M., Zhu, G., and Jin, Z. Origin, influence, and countermeasures of defects in perovskite solar cells. *Small*, 17(26):2005495, 2021. doi: https://doi.org/10.1002/smll.202005495. URL `https://onlinelibrary.wiley.com/doi/abs/10.1002/smll.202005495`.

Leijtens, T., Eperon, G. E., Pathak, S., Abate, A., Lee, M. M., and Snaith, H. J. Overcoming ultraviolet light instability of sensitized $TiO_2$ with meso-superstructured organometal tri-halide perovskite solar cells. *Nature Communications*, 4(1):2885, Dec 2013. ISSN 2041-1723. doi: 10.1038/ncomms3885. URL `https://doi.org/10.1038/ncomms3885`.

Leijtens, T., Bush, K., Cheacharoen, R., Beal, R., Bowring, A., and McGehee, M. D. Towards enabling stable lead halide perovskite solar cells; interplay between structural, environmental, and thermal stability. *J. Mater. Chem. A*, 5:11483–11500, 2017. doi: 10.1039/C7TA00434F. URL `http://dx.doi.org/10.1039/C7TA00434F`.

Li, Q., Chen, Z., Tranca, I., Gaastra-Nedea, S., Smeulders, D., and Tao, S. Compositional effect on water adsorption on metal halide perovskites. *Applied Surface Science*, 538:148058, 2021. ISSN 0169-4332. doi: https://doi.org/10.1016/j.apsusc.2020.148058. URL `https://www.sciencedirect.com/science/article/pii/S0169433220328154`.

Li, W., Zhang, W., Van Reenen, S., Sutton, R. J., Fan, J., Haghighirad, A. A., Johnston, M. B., Wang, L., and Snaith, H. J. Enhanced uv-light stability of planar heterojunction perovskite solar cells with caesium bromide interface modification. *Energy Environ. Sci.*, 9:490–498, 2016a. doi: 10.1039/C5EE03522H. URL `http://dx.doi.org/10.1039/C5EE03522H`.

Li, Y., Xu, X., Wang, C., Ecker, B., Yang, J., Huang, J., and Gao, Y. Light-induced degradation of $CH_3NH_3PbI_3$ hybrid perovskite thin film. *The Journal of Physical Chemistry C*, 121(7):3904–3910, 2017. doi: 10.1021/acs.jpcc.6b11853. URL `https://doi.org/10.1021/acs.jpcc.6b11853`.

Li, Z., Yang, M., Park, J.-S., Wei, S.-H., Berry, J. J., and Zhu, K. Stabilizing perovskite structures by tuning tolerance factor: Formation of formamidinium and cesium lead iodide solid-state alloys. *Chemistry of Materials*, 28(1):284–292, 2016b. doi: 10.1021/acs.chemmater.5b04107. URL `https://doi.org/10.1021/acs.chemmater.5b04107`.

Li, Z., Ji, J., Zhang, C., Hou, Q., and Jin, P. First-principles study on the oxygen–light-induced iodide vacancy formation in $FASnI_3$ perovskite. *The Journal of Physical Chemistry C*, 124(26):14147–14157, 2020. doi: 10.1021/acs.jpcc.0c01252. URL `https://doi.org/10.1021/acs.jpcc.0c01252`.

Liu, N., Wang, L., Xu, F., Wu, J., Song, T., and Chen, Q. Recent progress in developing monolithic perovskite/si tandem solar cells. *Frontiers in Chemistry*, 8:1120, 2020. ISSN 2296-2646. doi: 10.3389/fchem.2020.603375. URL `https://www.frontiersin.org/article/10.3389/fchem.2020.603375`.

Liu, Z., Peters, J. A., Stoumpos, C. C., Sebastian, M., Wessels, B. W., Im, J., Freeman, A. J., and Kanatzidis, M. G. Heavy metal ternary halides for room-temperature x-ray and gamma-ray detection. In Fiederle, M., Burger, A., Franks, L., and James, R. B., editors, *Hard X-Ray, Gamma-Ray, and Neutron Detector Physics XV*, volume 8852, pages 17 – 23. International Society for Optics and Photonics, SPIE, 2013. doi: 10.1117/12.2022877. URL `https://doi.org/10.1117/12.2022877`.

Ma, F., Li, J., Li, W., Lin, N., Wang, L., and Qiao, J. Stable alpha/delta phase junction of formamidinium lead iodide perovskites for enhanced near-infrared emission. *Chem. Sci.*, 8:800–805, 2017. doi: 10.1039/C6SC03542F. URL `http://dx.doi.org/10.1039/C6SC03542F`.

Maheshwari, S., Fridriksson, M. B., Seal, S., Meyer, J., and Grozema, F. C. The relation between rotational dynamics of the organic cation and phase transitions in hybrid halide perovskites. *The Journal of Physical Chemistry C*, 123(23):14652–14661, 2019. doi: 10.1021/acs.jpcc.9b02736. URL https://doi.org/10.1021/acs.jpcc.9b02736.

Martin, R. M. *Pseudopotentials*, pages 204–232. Cambridge University Press, 2004. doi: 10.1017/CBO9780511805769.013.

Matthews, R. W. Photo-oxidation of organic material in aqueous suspensions of titanium dioxide. *Water Research*, 20(5):569 – 578, 1986. ISSN 0043-1354. doi: https://doi.org/10.1016/0043-1354(86)90020-5. URL http://www.sciencedirect.com/science/article/pii/0043135486900205.

Mayerhöfer, T. and Popp, J. Beer's law derived from electromagnetic theory. *Spectrochimica Acta Part A: Molecular and Biomolecular Spectroscopy*, 215, 02 2019. doi: 10.1016/j.saa.2019.02.103.

Meggiolaro, D., Mosconi, E., and De Angelis, F. Mechanism of reversible trap passivation by molecular oxygen in lead-halide perovskites. *ACS Energy Letters*, 2(12): 2794–2798, 2017. doi: 10.1021/acsenergylett.7b00955. URL https://doi.org/10.1021/acsenergylett.7b00955.

Meloni, S., Palermo, G., Ashari-Astani, N., Grätzel, M., and Rothlisberger, U. Valence and conduction band tuning in halide perovskites for solar cell applications. *J. Mater. Chem. A*, 4:15997–16002, 2016. doi: 10.1039/C6TA04949D. URL http://dx.doi.org/10.1039/C6TA04949D.

Metz, B., Stoll, H., and Dolg, M. Small-core multiconfiguration-Dirac-Hartree-Fock-adjusted pseudopotentials for post-*d* main group elements: Application to PbH and PbO. *Journal of Chemical Physics*, 113(7):2563–2569, 2000. doi: 10.1063/1.1305880.

Møller, C. K. Crystal structure and photoconductivity of cæsium plumbohalides. *Nature*, 182:1436, Nov 1958. doi: 10.1038/1821436a0. URL https://doi.org/10.1038/1821436a0.

Moller, C. Crystal structure and photoconductivity of cesium plumbohalides. *Nature (London)*, 182:1436–1436, 1958.

Monkhorst, H. J. and Pack, J. D. Special points for Brillouin-zone integrations. *Phys. Rev. B*, 13:5188–5192, Jun 1976. doi: 10.1103/PhysRevB.13.5188. URL `http://link.aps.org/doi/10.1103/PhysRevB.13.5188`.

Moreira, R. L. and Dias, A. Comment on “prediction of lattice constant in cubic perovskites”. *Journal of Physics and Chemistry of Solids*, 68(8):1617 – 1622, 2007. ISSN 0022-3697. doi: https://doi.org/10.1016/j.jpcs.2007.03.050. URL `http://www.sciencedirect.com/science/article/pii/S0022369707001850`.

Murtaza, G. and Ahmad, I. First principle study of the structural and optoelectronic properties of cubic perovskites $CsPbM_3$(M = Cl, Br, I). *Physica B, Condensed Matter*, 406:3222–3229, 2011.

Natarajan, M. and Prakash, B. Phase transitions in $ABX_3$ type halides. *Phys. Stat. Sol. (a)*, 4:K167–K172, Mar 1971. doi: 10.1002/pssa.2210040331. URL `https://doi.org/10.1002/pssa.2210040331`.

Ni, M., Leung, M. K., Leung, D. Y., and Sumathy, K. A review and recent developments in photocatalytic water-splitting using $TiO_2$ for hydrogen production. *Renewable and Sustainable Energy Reviews*, 11(3):401 – 425, 2007. ISSN 1364-0321. doi: https://doi.org/10.1016/j.rser.2005.01.009. URL `http://www.sciencedirect.com/science/article/pii/S1364032105000420`.

Noh, J. H., Im, S. H., Heo, J. H., Mandal, T. N., and Seok, S. I. Chemical management for colorful, efficient, and stable inorganic–organic hybrid nanostructured solar cells. *Nano Letters*, 13(4):1764–1769, 2013. doi: 10.1021/nl400349b. URL `https://doi.org/10.1021/nl400349b`. PMID: 23517331.

Palazon, F., Pérez-del Rey, D., Dänekamp, B., Dreessen, C., Sessolo, M., Boix, P. P., and Bolink, H. J. Room-temperature cubic phase crystallization and high stability of vacuum-deposited methylammonium lead triiodide thin films for high-efficiency solar cells. *Advanced Materials*, 31(39):1902692. doi: https://doi.org/10.1002/adma.201902692. URL `https://onlinelibrary.wiley.com/doi/abs/10.1002/adma.201902692`.

Pearson, A. J., Eperon, G. E., Hopkinson, P. E., Habisreutinger, S. N., Wang, J. T.-W., Snaith, H. J., and Greenham, N. C. Oxygen degradation in mesoporous $Al_2O_3/CH_3NH_3PbI_{3-x}Cl_x$ perovskite solar cells: Kinetics and mechanisms. *Advanced Energy Materials*, 6(13):1600014, 2016. doi: 10.1002/aenm.201600014. URL https://onlinelibrary.wiley.com/doi/abs/10.1002/aenm.201600014.

Perdew, J. P., Parr, R. G., Levy, M., and Balduz, J. L. Density-functional theory for fractional particle number: Derivative discontinuities of the energy. *Phys. Rev. Lett.*, 49:1691–1694, Dec 1982. doi: 10.1103/PhysRevLett.49.1691. URL https://link.aps.org/doi/10.1103/PhysRevLett.49.1691.

Perdew, J. P., Burke, K., and Ernzerhof, M. Generalized gradient approximation made simple. *Phys. Rev. Lett.*, 77:3865–3868, Oct 1996a. doi: 10.1103/PhysRevLett.77.3865. URL https://link.aps.org/doi/10.1103/PhysRevLett.77.3865.

Perdew, J. P., Ernzerhof, M., and Burke, K. Rationale for mixing exact exchange with density functional approximations. *The Journal of Chemical Physics*, 105(22):9982–9985, 1996b. doi: 10.1063/1.472933. URL https://doi.org/10.1063/1.472933.

Perdew, J. P., Ruzsinszky, A., Csonka, G. I., Vydrov, O. A., Scuseria, G. E., Constantin, L. A., Zhou, X., and Burke, K. Restoring the density-gradient expansion for exchange in solids and surfaces. *Phys. Rev. Lett.*, 100:136406, Apr 2008a. doi: 10.1103/PhysRevLett.100.136406. URL https://link.aps.org/doi/10.1103/PhysRevLett.100.136406.

Perdew, J. P., Ruzsinszky, A., Csonka, G. I., Vydrov, O. A., Scuseria, G. E., Constantin, L. A., Zhou, X., and Burke, K. Restoring the density-gradient expansion for exchange in solids and surfaces. *Phys. Rev. Lett.*, 100:136406, Apr 2008b. doi: 10.1103/PhysRevLett.100.136406. URL https://link.aps.org/doi/10.1103/PhysRevLett.100.136406.

Peterson, K. A., Figgen, D., Goll, E., Stoll, H., and Dolg, M. Systematically convergent basis sets with relativistic pseudopotentials. ii. small-core pseudopotentials and correlation consistent basis sets for the post-d group 16–18 elements. *The Journal of Chemical Physics*, 119(21):11113–11123, 2003. doi: 10.1063/1.1622924. URL https://doi.org/10.1063/1.1622924.

Peterson, K. A., Shepler, B. C., Figgen, D., and Stoll, H. On the spectroscopic and thermochemical properties of clo, bro, io, and their anions. *The Journal of Physical Chemistry A*, 110(51):13877–13883, 2006. doi: 10.1021/jp065887l. URL https://doi.org/10.1021/jp065887l. PMID: 17181347.

Pisani, C. *The CRYSTAL code*, pages 125–137. Springer, Berlin, Heidelberg, 1996. doi: https://doi.org/10.1007/978-3-642-61478-1.

Poglitsch, A. and Weber, D. Dynamic disorder in methylammoniumtrihalogenoplumbates (II) observed by millimeter-wave spectroscopy. *The Journal of Chemical Physics*, 87(11):6373–6378, 1987. doi: 10.1063/1.453467. URL https://doi.org/10.1063/1.453467.

Protesescu, L., Yakunin, S., Bodnarchuk, M. I., Krieg, F., Caputo, R., Hendon, C. H., Yang, R. X., Walsh, A., and Kovalenko, M. V. Nanocrystals of cesium lead halide perovskites ($CsPbX_3$, X = Cl, Br, and I): Novel optoelectronic materials showing bright emission with wide color gamut. *Nano Letters*, 15:3692, Jun 2015. doi: 10.1021/nl5048779. URL https://doi.org/10.1021/nl5048779.

Quarti, C., Mosconi, E., Ball, J. M., D'Innocenzo, V., Tao, C., Pathak, S., Snaith, H. J., Petrozza, A., and De Angelis, F. Structural and optical properties of methylammonium lead iodide across the tetragonal to cubic phase transition: implications for perovskite solar cells. *Energy Environ. Sci.*, 9:155–163, 2016. doi: 10.1039/C5EE02925B. URL http://dx.doi.org/10.1039/C5EE02925B.

Scott, J. F., Palai, R., Kumar, A., Singh, M. K., Murari, N. M., Karan, N. K., and Katiyar, R. S. New phase transitions in perovskite oxides: $BiFeO_3$, $SrSnO_3$, and $pb(fe_{2/3}w_{1/3})_{1/2}ti_{1/2}o_3$. *Journal of the American Ceramic Society*, 91(6):1762–1768, 2008. doi: https://doi.org/10.1111/j.1551-2916.2008.02404.x. URL https://ceramics.onlinelibrary.wiley.com/doi/abs/10.1111/j.1551-2916.2008.02404.x.

Singh, D. J. and Nordstrom, L. *Planewaves, Pseudopotentials, and the LAPW Method*, pages XIII, 134. Springer US, 2006. ISBN 978-0-387-29684-5. doi: 10.1007/978-0-387-29684-5.

Slater, J. C. The theory of complex spectra. *Phys. Rev.*, 34:1293–1322, Nov 1929. doi: 10.1103/PhysRev.34.1293. URL `https://link.aps.org/doi/10.1103/PhysRev.34.1293`.

Snaith, H. J., Abate, A., Ball, J. M., Eperon, G. E., Leijtens, T., Noel, N. K., Stranks, S. D., Wang, J. T.-W., Wojciechowski, K., and Zhang, W. Anomalous hysteresis in perovskite solar cells. *The Journal of Physical Chemistry Letters*, 5(9):1511–1515, 2014. doi: 10.1021/jz500113x. URL `https://doi.org/10.1021/jz500113x`. PMID: 26270088.

Sophia, G., Baranek, P., Sarrazin, C., Rérat, M., and Dovesi, R. First-principles study of the mechanisms of the pressure-induced dielectric anomalies in ferroelectric perovskites. *Phase Transitions*, 86(11):1069–1084, 2013. doi: 10.1080/01411594.2012.754442. URL `http://dx.doi.org/10.1080/01411594.2012.754442`.

Stoumpos, C. C. and Kanatzidis, M. G. The renaissance of halide perovskites and their evolution as emerging semiconductors. *Accounts of Chemical Research*, 48(10):2791–2802, 2015. doi: 10.1021/acs.accounts.5b00229. URL `https://doi.org/10.1021/acs.accounts.5b00229`. PMID: 26350149.

Stoumpos, C. C., Malliakas, C. D., and Kanatzidis, M. G. Semiconducting tin and lead iodide perovskites with organic cations: Phase transitions, high mobilities, and near-infrared photoluminescent properties. *Inorganic Chemistry*, 52(15):9019–9038, 2013a. doi: 10.1021/ic401215x. URL `https://doi.org/10.1021/ic401215x`. PMID: 23834108.

Stoumpos, C. C., Malliakas, C. D., Peters, J. A., Liu, Z., Sebastian, M., Im, J., Chasapis, T. C., Wibowo, A. C., Chung, D. Y., Freeman, A. J., Wessels, B. W., and Kanatzidis, M. G. Crystal growth of the perovskite semiconductor $CsPbBr_3$: A new material for high-energy radiation detection. *Crystal Growth & Design*, 13(7):2722–2727, 2013b. doi: 10.1021/cg400645t. URL `https://doi.org/10.1021/cg400645t`.

Stranks, S. D., Eperon, G. E., Grancini, G., Menelaou, C., Alcocer, M. J. P., Leijtens, T., Herz, L. M., Petrozza, A., and Snaith, H. J. *Science*, 342(6156):341–344, 2013. ISSN 0036-8075. doi: 10.1126/science.1243982. URL `https://science.sciencemag.org/content/342/6156/341`.

Sutton, R. J., Eperon, G. E., Miranda, L., Parrott, E. S., Kamino, B. A., Patel, J. B., Hrantner, M. T., Johnston, M. B., Haghighirad, A. A., Moore, D. T., and Snaith, H. J. Bandgap-tunable cesium lead halide perovskites with high thermal stability for efficient solar cells. *Advanced Energy Materials*, 6(8):1502458, 2016. doi: https://doi.org/10.1002/aenm.201502458. URL `https://onlinelibrary.wiley.com/doi/abs/10.1002/aenm.201502458`.

Swarnkar, A., Marshall, A. R., Sanehira, E. M., Chernomordik, B. D., Moore, D. T., Christians, J. A., Chakrabarti, T., and Luther, J. M. Quantum dot-induced phase stabilization of $\alpha$-$CsPbI_3$ perovskite for high-efficiency photovoltaics. *Science*, 354 (6308):92–95, Oct 2016. ISSN 0036-8075. doi: 10.1126/science.aag2700. URL `https://science.sciencemag.org/content/354/6308/92`.

Tanaka, K., Takahashi, T., Ban, T., Kondo, T., Uchida, K., and Miura, N. *Solid State Communications*, 127:619–623, 09 2003. doi: 10.1016/S0038-1098(03)00566-0.

Tang, C., Chen, C., Xu, W., and Xu, L. Design of doped cesium lead halide pervskite as photo-catalytic $CO_2$ reduction catalyst. *Journal of Materials Chemistry A*, 7:6911–6919, 2019.

Thomas, L. H. The calculation of atomic fields. *Mathematical Proceedings of the Cambridge Philosophical Society*, 23(5):542–548, 1927. doi: 10.1017/S0305004100011683.

Trots, D. and Myagkota, S. High-temperature structural evolution of caesium and rubidium triiodoplumbates. *Journal of Physics and Chemistry of Solids*, 69:2520–2526, 2008.

Uddin, A., Upama, M. B., Yi, H., and Duan, L. Encapsulation of organic and perovskite solar cells: A review. *Coatings*, 9(2), 2019. ISSN 2079-6412. doi: 10.3390/coatings9020065. URL `https://www.mdpi.com/2079-6412/9/2/65`.

Vincent, B. R., Robertson, K. N., Cameron, T. S., and Knop, O. Alkylammonium lead halides. Part 1. isolated $PbI_6^{4-}$– ions in $(CH_3NH)_4PbI_6{\cdot}2H_2O$. *Canadian Journal of Chemistry*, 65(5):1042–1046, 1987. doi: 10.1139/v87-176. URL https://doi.org/10.1139/v87-176.

Vosko, S. H., Wilk, L., and Nusair, M. Accurate spin-dependent electron liquid correlation energies for local spin density calculations: a critical analysis. *Canadian Journal of Physics*, 58(8):1200–1211, 1980. doi: 10.1139/p80-159. URL https://doi.org/10.1139/p80-159.

Wadt, W. R. and Hay, P. J. Ab initio effective core potentials for molecular calculations. Potentials for main group elements Na to Bi. *The Journal of Chemical Physics*, 82 (1):284–298, 1985. doi: 10.1063/1.448800. URL https://doi.org/10.1063/1.448800.

Walsh, A., Scanlon, D. O., Chen, S., Gong, X. G., and Wei, S.-H. Self-regulation mechanism for charged point defects in hybrid halide perovskites. *Angewandte Chemie International Edition*, 54(6):1791–1794, 2015. doi: 10.1002/anie.201409740. URL https://onlinelibrary.wiley.com/doi/abs/10.1002/anie.201409740.

Wang, F. F. Y. and Gupta, K. P. Phase transformation in the oxides. *Metallurgical Transactions*, 4(12):2767–2779, Dec 1973. ISSN 1543-1916. doi: 10.1007/BF02644576. URL https://doi.org/10.1007/BF02644576.

Wang, Z., McMeekin, D. P., Sakai, N., van Reenen, S., Wojciechowski, K., Patel, J. B., Johnston, M. B., and Snaith, H. J. Efficient and air-stable mixed-cation lead mixed-halide perovskite solar cells with n-doped organic electron extraction layers. *Advanced Materials*, 29(5):1604186, 2017. doi: 10.1002/adma.201604186. URL https://onlinelibrary.wiley.com/doi/abs/10.1002/adma.201604186.

Weller, M. T., Weber, O. J., Frost, J. M., and Walsh, A. Cubic perovskite structure of black formamidinium lead iodide, $\alpha$-$[HC(NH_2)_2]PbI_3$, at 298 K. *The Journal of Physical Chemistry Letters*, 6(16):3209–3212, 2015. doi: 10.1021/acs.jpclett.5b01432. URL https://doi.org/10.1021/acs.jpclett.5b01432.

Whitfield, P. S., Herron, N., Guise, W. E., Page, K., Cheng, Y. Q., Milas, I., and Crawford, M. K. Structures, phase transitions and tricritical behavior of the hybrid perovskite methyl ammonium lead iodide. *Scientific Reports*, 6(1):35685, Oct 2016. ISSN 2045-2322. doi: 10.1038/srep35685. URL `https://doi.org/10.1038/srep35685`.

Yang, J., Siempelkamp, B. D., Liu, D., and Kelly, T. L. Investigation of ch3nh3pbi3 degradation rates and mechanisms in controlled humidity environments using in situ techniques. *ACS Nano*, 9(2):1955–1963, 2015a. doi: 10.1021/nn506864k. URL `https://doi.org/10.1021/nn506864k`. PMID: 25635696.

Yang, R. X., Skelton, J. M., da Silva, E. L., Frost, J. M., and Walsh, A. Spontaneous octahedral tilting in the cubic inorganic cesium halide perovskites $CsSnX_3$ and $CsPbX_3$ (X = F, Cl, Br, I). *The Journal of Physical Chemistry Letters*, 8(19):4720–4726, 2017. doi: 10.1021/acs.jpclett.7b02423. URL `https://doi.org/10.1021/acs.jpclett.7b02423`. PMID: 28903562.

Yang, T.-Y., Gregori, G., Pellet, N., Grätzel, M., and Maier, J. The significance of ion conduction in a hybrid organic–inorganic lead-iodide-based perovskite photosensitizer. *Angewandte Chemie International Edition*, 54(27):7905–7910, 2015b. doi: 10.1002/anie.201500014. URL `https://onlinelibrary.wiley.com/doi/abs/10.1002/anie.201500014`.

Yang, W. S., Noh, J. H., Jeon, N. J., Kim, Y. C., Ryu, S., Seo, J., and Seok, S. I. High-performance photovoltaic perovskite layers fabricated through intramolecular exchange. *Science*, 348(6240):1234–1237, 2015c. ISSN 0036-8075. doi: 10.1126/science.aaa9272. URL `https://science.sciencemag.org/content/348/6240/1234`.

Yin, W.-J., Shi, T., and Yan, Y. Unusual defect physics in $CH_3NH_3PbI_3$ perovskite solar cell absorber. *Applied Physics Letters*, 104(6):063903, 2014. doi: 10.1063/1.4864778. URL `https://doi.org/10.1063/1.4864778`.

Yu, D., Yang, Y.-Q., Chen, Z., Tao, Y., and Liu, Y.-F. Recent progress on thin-film encapsulation technologies for organic electronic devices. *Optics Communications*, 362:43 – 49, 2016. ISSN 0030-4018. doi: https://doi.org/10.1016/j.optcom.2015.08.021. URL `http://www.sciencedirect.com/science/article/pii/S0030401815300134`. Polymer Photonics and Its Applications.

Zekry, A. and Shaker, A. *Solar cells and arrays: Principles, analysis and design*. 02 2018.

Zhang, J., Hu, Z., Huang, L., Yue, G., Liu, J., Lu, X., Hu, Z., Shang, M., Han, L., and Zhu, Y. Bifunctional alkyl chain barriers for efficient perovskite solar cells. *Chem. Commun.*, 51:7047–7050, 2015. doi: 10.1039/C5CC00128E. URL `http://dx.doi.org/10.1039/C5CC00128E`.

Zicovich-Wilson, C. *LoptCG (Shell Procedure for Numerical Gradient Optimization)*. Instituto de Technologia Quimica, Valencia, 2006.

# Appendix

## Atomic Gaussian-type functions (GTF) basis sets description

As regards the atomic basis sets, all-electron GTFs has been used for the carbon [Dovesi et al., 1990], oxygen [Sophia et al., 2013] and chlorine [Apra et al., 1993] while the Stuttgart–Dresden fully relativistic pseudopotentials have been adopted for Br [Peterson et al., 2003], I [Peterson et al., 2006] and Pb [Metz et al., 2000], and a Hay–Wadt pseudopotential for Cs [Hay and Wadt, 1985a,b,c]. All-electron basis set has been used for Cl (a 8$s$-62111$sp$-1$d^*$ GTFs contraction) [Apra et al., 1993]. Cs atom has been described with a 31$sp$-1$d^*$ GTFs contraction developed for $CsTaO_3$ [web]. The basis sets adopted for Br, I and Pb (developed for $PbBO_3$ perovskites with B = Ti and Zr, see Sophia et al. [2013] are a 72111$sp$-7$d$-1$d^*$, a 7211$sp$-7$d$-1$d^*$ and a 6111$sp$-5$d$-1$d^*$ GTFs contractions, respectively. The exponents and coefficients of contraction of $s$, $sp$, $p$ and $d$ functions have been optimized, using energy criteria, and are given in Table A.1. Basis-sets optimizations have been carried out using the LoptCG script [Zicovich-Wilson, 2006] which performs numerical gradient optimizations based on the conjugate gradient method [Hestenes and Stiefel, 1952].

TABLE A.1: Exponents and coefficients of the contracted Gaussian basis sets adopted in the present study for C, O, Cl, Br, I, Cs and Pb. For the C, O and Cl all-electron basis sets, only the most diffuse GTFs is given (see Ref. Dovesi et al. [1990]; Sophia et al. [2013]; Apra et al. [1993]; web for a complete set of data). For the pseudopotential basis sets, Br, I and Pb GTFs contractions are used in conjunction with the Stuttgart–Dresden fully relativistic pseudopotentials [Peterson et al., 2003, 2006; Metz et al., 2000], and Cs GTFs contraction with a Hay–Wadt small-core pseudopotential [Hay and Wadt, 1985a,b,c]. For Cs and Pb, only the most diffuse GTFs are given (see Ref. [Sophia et al., 2013] for a complete set of data).

| Atom | Shell | Exponents | Coefficients | |
|---|---|---|---|---|
| | | | $s(d)$ | $p$ |
| C | $sp$ | 0.227298 | 1. | 1. |
| | $d$ | 0.694919 | 1. | |
| O | $sp$ | 0.482979 | 1. | 1. |
| | $sp$ | 0.161613 | 1. | 1. |
| | $d$ | 1.106642 | 1. | |
| Cl | $sp$ | 4.789820 | −0.272688 | −0.084582 |
| | | 2.146002 | −0.604093 | 0.183656 |
| | $sp$ | 0.959050 | 1. | 1. |
| | $sp$ | 0.416937 | 1. | 1. |
| | $sp$ | 0.151664 | 1. | 1. |
| | $d$ | 0.269351 | 1. | |
| Br | $sp$ | 721.558550 | 0.008134 | 0.000204 |
| | | 96.462987 | 0.024401 | 0.0180340 |
| | | 35.398004 | 0.141929 | −0.080949 |
| | | 19.933160 | −0.59122 | −0.111425 |
| | | 7.4223656 | 0.081007 | 0.676694 |
| | | 3.8278678 | 0.949186 | 0.639332 |
| | | 1.926981 | 0.200306 | 0.192366 |
| | $sp$ | 7.009481 | −0.957342 | −0.056926 |
| | | 3.258283 | 0.621529 | 0.821226 |
| | $sp$ | 1.805381 | 1. | 1. |
| | $sp$ | 0.488054 | 1. | 1. |
| | $sp$ | 0.151398 | 1. | 1. |
| | $d$ | 141.068183 | 0.016631 | |
| | | 58.114934 | 0.033892 | |
| | | 42.981469 | 0.087185 | |
| | | 19.209560 | 0.318069 | |
| | | 8.149961 | 0.618389 | |
| | | 3.292553 | 0.737154 | |
| | | 1.179384 | 0.377196 | |
| | $d$ | 0.215849 | 1. | |

Continued on the next page

TABLE A.1: Continuation.

| Atom | Shell | Exponents | Coefficients | |
|---|---|---|---|---|
| | | | $s(d)$ | $p$ |
| I | $sp$ | 41.213231 | −0.004401 | −0.009530 |
| | | 25.479504 | 0.036324 | 0.063600 |
| | | 13.575108 | 0.232084 | −0.135903 |
| | | 7.863024 | −0.911172 | −0.170833 |
| | | 2.776888 | 0.753281 | 0.892493 |
| | | 1.199857 | 0.448500 | 0.155090 |
| | | 0.379795 | 0.025848 | 0.070783 |
| | $sp$ | 3.364687 | 0.020613 | 0.020320 |
| | | 0.881817 | 0.882325 | 0.900521 |
| | $sp$ | 0.753913 | 1. | 1. |
| | $sp$ | 0.157636 | 1. | 1. |
| | $d$ | 62.391688 | 0.002346 | |
| | | 28.420863 | 0.002614 | |
| | | 12.360244 | −0.019163 | |
| | | 5.632079 | 0.099010 | |
| | | 3.247671 | 0.326073 | |
| | | 1.873532 | 0.363723 | |
| | | 0.830273 | 0.340973 | |
| | $d$ | 0.184114 | 1.0 | |
| Cs | $sp$ | 0.166761 | 1. | 1. |
| | $d$ | 0.35 | 1. | |
| Pb | $sp$ | 1.298223 | 1. | 1. |
| | $sp$ | 0.293988 | 1. | 1. |
| | $sp$ | 0.128864 | 1. | 1. |
| | $d$ | 0.237672 | 1. | |

# Detailed adsorption energies for the CsX-terminated surfaces

Concerning the CsX-terminated surfaces, Figure A.1 shows the two relaxation patterns, which follow the actually "observed" relaxations, obtained for X = Cl, Br and for X = I on the left and right panels, respectively (the trends have been exaggerated for better visibility). The origin of the surface unit cell in both cases is chosen so that the Cs surface atom, which is the least displaced relative to the projection of his deep-layer counterparts, resides at a corner. For these surfaces, assuming the $C_{2h}^{1}$ symmetry, one can identify 6 irreducible Cs sites; however, for the surfaces based on CsPbCl$_3$ and CsPbBr$_3$, after the atomic relaxations, one can make distinction between four Cs sites, among which the four "identical" neighbours ② shrink together towards the reference atom in the corner (① in the figure), making what we'll refer to as "star" (X=Br, Cl). The third species ③ somehow takes off from the X atom at the middle of the cell, making a loosely bound "wheel". The position $\boxed{4}$ between two "stars" and two "wheels", referred as `CsX-s4`, is a site on top of the underlying X atom, cornered

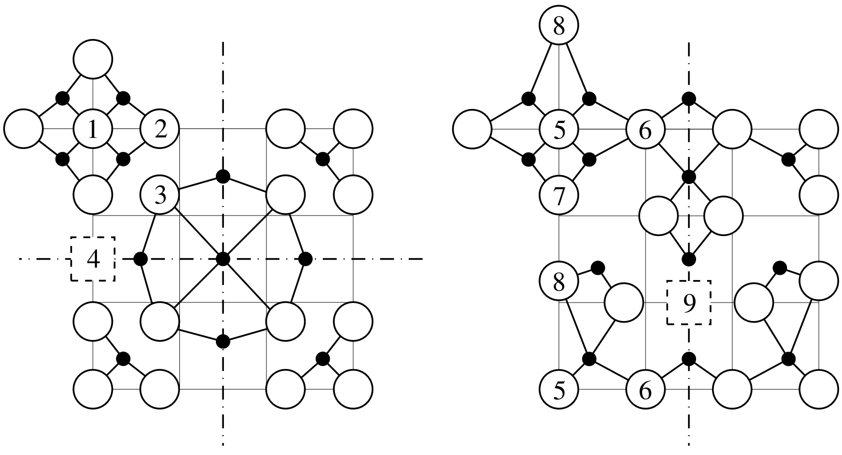

• X = Cl, Br • X = I

FIGURE A.1: Schematic view of reconstruction at the CsX surface (represented by a $3{\times}3$ supercell) with X= Cl, Br (left panel) and X=I (right panel). Only the surface layer is shown. The numbers indicate Cs with nonequivalent local environment. The dashed squares indicate in-plane adsorption positions between two Cs atoms shifted apart, on top of an X atom in the underlying PbX$_2$ plane. The numbering of sites $N = 1, 2, \ldots, 9$ introduced is translated as $N \rightarrow$ `CsX-s`$N$ for the discussion in the text.

TABLE A.2: Band gap values (in eV) for 3D crystals and different slabs, as calculated in the present work. The bulk data are given for comparison.

| | | Slabs termination | |
|---|---|---|---|
| Perovskite | Bulk | CsX | $PbX_2$ |
| $CsPbCl_3$ | 3.25 | 3.21 | 3.33 |
| $CsPbBr_3$ | 2.57 | 2.52 | 2.67 |
| $CsPbI_3$ | 2.13 | 2.10 | 2.28 |

by two Cs and two X atoms, all being shifted apart in-plane.

On the other hand, the relaxation pattern characteristics for CsI surface are much more complex. No isolated structures emerge; however, one can identify an "opening" $\boxed{9}$ on top of the underlying iodine atom, similar to the site $\boxed{4}$ of left panel of Figure A.1, from which two of its in-plane Cs neighbors and two I-neighbors are somehow shifted away. The sites ① through $\boxed{9}$ are referred to as CsX-s1 through CsX-s9 in the tables A.3, A.4, A.5 below.

Table A.2 gives the band gap values of the free relaxed slabs. They are compared to the band gap values of the respective orthorhombic phases which possess the same

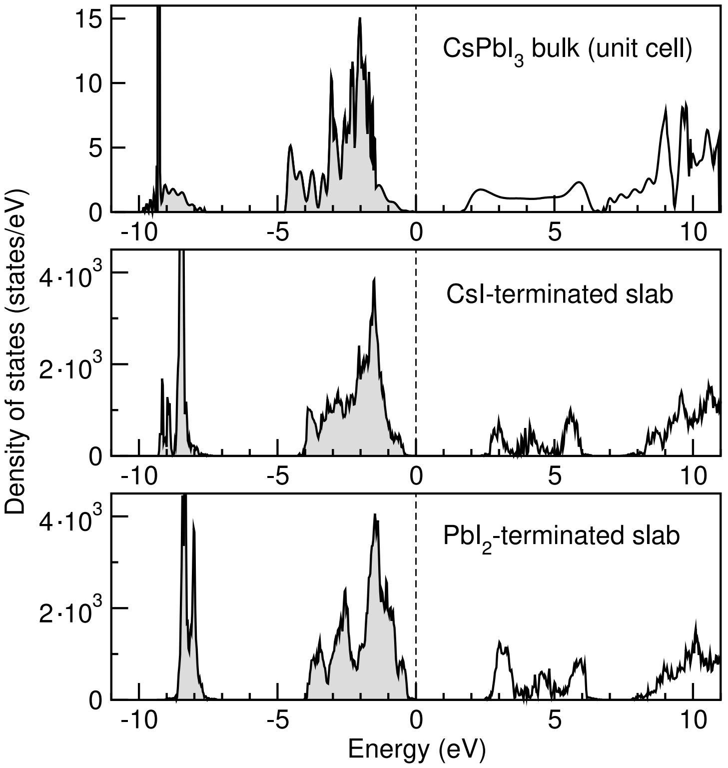

FIGURE A.2: Densities of states of bulk perovskite $CsPbI_3$ and of 11-layer slabs with different terminations.

TABLE A.3: Relaxed interatomic distances (in Å) and calculated adsorption energies (eV) in different adsorption sites of CO on CsX surfaces. The energies are not corrected for BSSE. The data follow the conventions of the Figure 4.4.

| X | | Cs–C | Cs–O | C–$X_0$ | O–$X_0$ | C–$X_{-1}$ | O–$X_{-1}$ | Cs–Cs | $X_0$–$X_0$ | $E_{\text{ads.}}$ |
|---|---|---|---|---|---|---|---|---|---|---|
| Cl, | CsCl-s1 | 3.47 | 3.69 | 3.24 | 3.63 | 5.23 | 5.81 | 5.30 | 4.95 | −0.22 |
| | CsCl-s2 | 3.48 | 3.34 | 3.31 | 3.62 | 3.18 | 3.60 | 6.67 | 6.92 | −0.28 |
| | CsCl-s3 | 3.50 | 3.64 | 3.19 | 3.60–3.63 | 5.19 | 5.68 | 5.37 | 4.96 | −0.22 |
| | CsCl-s4 | 3.41 | 3.30 | 3.24 | 3.62–3.83 | 3.40 | 3.86 | 6.41 | 6.38 | −0.26 |
| Br, | CsBr-s1 | 3.53 | 3.63 | 3.25 | 3.65 | 5.34 | 5.87 | 5.40 | 5.17 | −0.23 |
| | CsBr-s2 | 3.55 | 3.41 | 3.36 | 3.71–4.34 | 3.19 | 3.60 | 6.92 | 7.24 | −0.29 |
| | CsBr-s3 | 3.48 | 3.62 | 3.24 | 3.65 | 5.10 | 5.65 | 5.47 | 5.28 | −0.24 |
| | CsBr-s4 | 3.52 | 3.38 | 3.37 | 3.72 | 3.20 | 3.62 | 6.88 | 7.20 | −0.29 |
| I, | CsI-s5 | 3.43 | 3.34 | 3.34 | 3.79–3.80 | 4.77 | 5.20 | 5.94 | 6.09 | −0.33 |
| | CsI-s6 | 3.49 | 4.21 | 3.30 | 3.75–3.76 | 5.69 | 6.35 | 5.53 | 5.23 | −0.32 |
| | CsI-s7 | 3.43 | 3.67 | 3.42 | 3.81 | 5.45 | 6.13 | 5.36 | 5.67 | −0.28 |
| | CsI-s8 | 3.61 | 3.48 | 3.51 | 3.85 | 3.28 | 3.72 | 6.96 | 7.21 | −0.35 |
| | CsI-s9 | 3.43 | 3.33 | 3.32 | 3.77–3.79 | 4.70 | 5.10 | 6.00 | 6.13 | −0.32 |

symmetry. The obtained band gaps make a reasonably small fork (of ± 3%) around the corresponding bulk value. The appearing discrepancies are a manifestation of the slab non-stoichiometry and its insufficient thickness (or serve to estimate a possible error due to this latter deficiency). These perovskites have also a band gap at $R$, and one can imagine that a (sparse) $\mathbf{k}$-mesh used for slab calculation would just by chance skip the $\mathbf{k}$-point yielding the states which delimit the gap. However, with our choice of $6{\times}6$ mesh for $3{\times}3$ supercell, the $\overline{R}$ point is correctly represented in the sampling. Then the obtained spread of the band gap between differently terminated slabs are acceptable.

Figure A.2 depicts DOS of crystalline perovskite $CsPbI_3$ and of two (relaxed) slabs, corresponding to two different terminations.

## Interlayer relaxation in defective $CsPbX_3$ surfaces

Tables A.6 and A.7 show that interlayer distances after the inclusion of charged and neutral vacancies respectively. The method of calculating the interlayer distance is similar to the method used for perfect surface, with the Figure A.3 indicating the interlayer distance. Whatever the surface, the interlayer distance increases with the increasing lattice parameter from $CsPbCl_3$, $CsPbBr_3$ to $CsPbI_3$ due to steric effect which is also the reason for the perfect surface.

TABLE A.4: Similar to Table A.3 for adsorption of $CO_2$.

| X | | Cs–O | C–$X_{-1}$ | C–$X_0$ | Cs–Cs | $X_0$–$X_0$ | $E_{\text{ads.}}$ |
|---|---|---|---|---|---|---|---|
| Cl, | CsCl-s1 | 3.27–2.32 | 5.59 | 3.36 | 5.39 | 4.83 | −0.26 |
| | CsCl-s2 | 3.19–3.20 | 3.38 | 3.21 | 6.86 | 6.99 | −0.36 |
| | CsCl-s3 | 3.29–3.30 | 5.45 | 3.31 | 5.53 | 4.87 | −0.27 |
| | CsCl-s4 | 3.19 | 3.38 | 3.20 | 6.86 | 6.98 | −0.36 |
| Br, | CsBr-s1 | 3.29–3.30 | 5.42 | 3.40–3.46 | 5.58 | 5.21 | −0.30 |
| | CsBr-s2 | 3.19 | 3.38 | 3.38 | 7.04 | 7.21 | −0.40 |
| | CsBr-s3 | 3.26–3.28 | 5.07 | 3.45–3.50 | 6.05 | 5.74 | −0.30 |
| | CsBr-s4 | 3.20–3.21 | 3.38 | 3.39–4.44 | 7.10 | 7.27 | −0.33 |
| I, | CsI-s5 | 3.22–3.31 | 5.75 | 3.50–3.51 | 6.57 | 5.77 | −0.39 |
| | CsI-s6 | 3.27–3.34 | 5.41 | 3.49 | 5.93 | 5.80 | −0.37 |
| | CsI-s7 | 3.23–3.32 | 5.78 | 3.56 | 5.56 | 5.60 | −0.33 |
| | CsI-s8 | 3.27–3.28 | 3.37 | 3.77–3.84 | 7.60 | 7.33 | −0.54 |
| | CsI-s9 | 3.23–3.30 | 5.21 | 3.52–3.55 | 6.05 | 6.01 | −0.37 |

TABLE A.5: Similar to Table A.3 for adsorption of $O_2$.

| X | | Cs–O | O–$X_{-1}$ | O–$X_0$ | Cs–Cs | $X_0$–$X_0$ | $E_{\text{ads.}}$ |
|---|---|---|---|---|---|---|---|
| Cl, | CsCl-s1 | 3.63–3.73 | 5.81 | 3.64–3.68 | 5.20 | 5.02 | −0.07 |
| | CsCl-s2 | 3.51–3.54 | 3.70–3.73 | 3.97–3.99 | 6.61 | 6.97 | −0.10 |
| | CsCl-s3 | 3.55–4.05 | 5.72–5.93 | 3.62–3.77 | 5.27 | 5.02 | −0.06 |
| | CsCl-s4 | 3.53–3.57 | 4.62–4.63 | 3.68–3.85 | 6.02 | 6.15 | −0.08 |
| Br, | CsBr-s1 | 3.64–3.93 | 5.93–5.96 | 3.68–3.71 | 5.33 | 5.21 | −0.08 |
| | CsBr-s2 | 3.64–3.95 | 5.91–5.95 | 3.64–3.71 | 5.36 | 5.16 | −0.08 |
| | CsBr-s3 | 3.76 | 5.70–5.74 | 3.61–3.72 | 5.54 | 5.31 | −0.08 |
| | CsBr-s4 | 3.59–3.60 | 3.67–3.68 | 4.04–4.06 | 6.89 | 7.28 | −0.11 |
| I, | CsI-s5 | 3.51–3.52 | 5.70–6.05 | 3.62–3.98 | 5.30 | 5.84 | −0.15 |
| | CsI-s6 | 3.37–3.61 | 5.20–5.21 | 3.44–3.87 | 5.86 | 6.28 | −0.15 |
| | CsI-s7 | 3.41–3.55 | 5.77–6.05 | 3.65–3.95 | 5.17 | 5.84 | −0.14 |
| | CsI-s8 | 3.51–4.77 | 3.64–3.76 | 3.87–4.41 | 7.70 | 7.61 | −0.20 |
| | CsI-s9 | 3.57–3.76 | 5.74–5.90 | 3.52–3.90 | 5.40 | 5.73 | −0.15 |

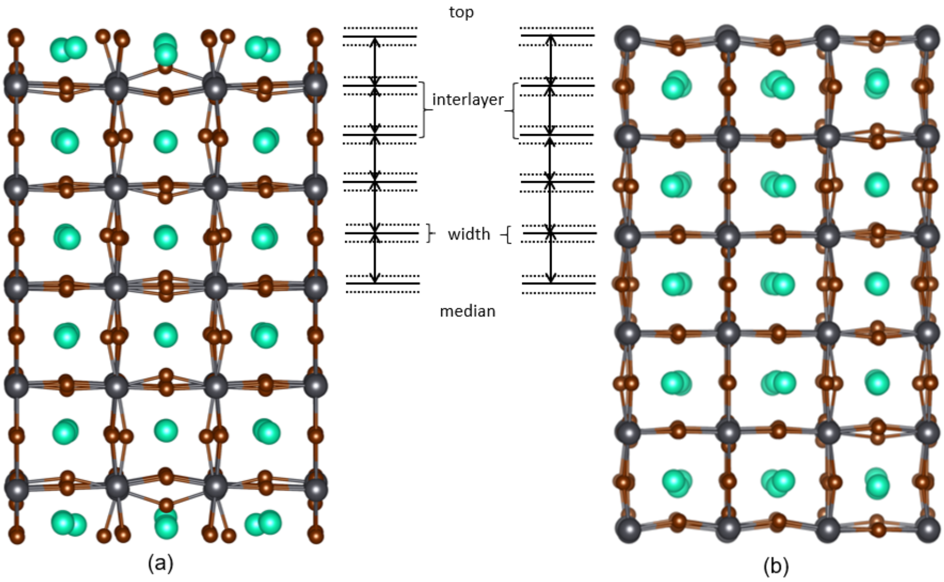

FIGURE A.3: Schematic view of the interlayer and the range of atomic relaxations around the interlayer (width), as defined in Table 3.4, for the CsX termination (a) and the $PbX_2$ termination (b).

The evolution of interlayer distances into the depth of a slab must eventually match the values corresponding to pure bulk. Whatever the compounds and termination of the surfaces, the perturbations of the interlayer distance (with respect to the perovskite structure, see Table A.6, A.7) are largest for the first layer (around 11%) which is smaller than in case of perfect surface, and the perturbations are further reduced towards the interior of the slab as the variation comes down to 0.3%. The inclusion of vacancies did not dramatically change the relaxation patterns.

## Detailed adsorption energies for the defective CsX-terminated surfaces

As discussed in the section of perfect $CsPbX_3$ surface, the CsX terminated structure undergoes surface reconstruction, in the course of which the possible adsorption sites are diversified by their symmetry and environment. Unlike for the perfect surface the number of sites for adsorption on $CsPbX_3$ (X=Cl, Br) and $CsPbI_3$ surfaces were different but for the creation of halide vacancies three potential sites were identified for all the three surfaces. In Figure A.4, in the left panel for X=Cl and Br, the center

TABLE A.6: Interlayer distances (inter in Å) and widths of (warped) atomic layers (width in Å) in relaxed slabs of $CsPbX_3$ for both CsX and $PbX_2$ terminations (see Figure A.3) with positively charged halide vacancies on top and bottom of the surface. For perovskite structure, the interlayer distance is half of the lattice parameter corresponding to 3.09, 2.94 and 2.82 Å for $CsPbI_3$, $CsPbBr_3$ and $CsPbCl_3$, respectively.

| | | $CsPbI_3$ | | $CsPbBr_3$ | | $CsPbCl_3$ | |
|---|---|---|---|---|---|---|---|
| | layer | width | inter | width | inter | width | inter |
| CsX termination | | | | | | | |
| (top) | CsX | 1.78 | | 0.86 | | 0.68 | |
| | | | 2.77 | | 2.63 | | 2.55 |
| | $PbX_2$ | 2.27 | | 2.02 | | 1.59 | |
| | | | 3.12 | | 3.13 | | 3.02 |
| | CsX | 0.55 | | 0.69 | | 0.33 | |
| | | | 3.02 | | 2.88 | | 2.79 |
| | $PbX_2$ | 2.06 | | 1.55 | | 1.49 | |
| | | | 3.06 | | 3.00 | | 2.85 |
| | CsX | 0.87 | | 0.66 | | 0.39 | |
| | | | 3.06 | | 2.91 | | 2.83 |
| (median) | $PbX_2$ | 2.10 | | 1.85 | | 1.33 | |
| $PbX_2$ termination | | | | | | | |
| (top) | $PbX_2$ | 1.80 | | 1.30 | | 0.77 | |
| | | | 2.62 | | 2.52 | | 2.44 |
| | CsX | 0.80 | | 0.68 | | 0.25 | |
| | | | 3.14 | | 2.99 | | 2.90 |
| | $PbX_2$ | 1.71 | | 1.05 | | 0.94 | |
| | | | 3.02 | | 2.88 | | 2.76 |
| | CsX | 0.87 | | 0.44 | | 0.11 | |
| | | | 3.12 | | 2.97 | | 2.84 |
| | $PbX_2$ | 1.92 | | 1.70 | | 1.18 | |
| | | | 3.07 | | 2.91 | | 2.82 |
| (median) | CsX | 0.79 | | 0.00 | | 0.00 | |

of the wheel is marked by V-CsX-s3, while V-CsX-s2, situated at the diagonal and V-CsX-s1 along the boundary of the wheel.

For the CsI surface, the right panel of the Figure A.4, V-CsI-s4 is at one of the corner of the star, V-CsI-s5 down south to the V-CsI-s4 and V-CsI-s6 along the (100) mirror plane.

In the above characterisation some of the potential sites were left out which poses almost the same situation as the above mentioned scenario. Further discussions in Chapter 3 regarding the vacancy formation energy and adsorption of molecules will

TABLE A.7: Interlayer distances (inter in Å) and widths of (warped) atomic layers (width in Å) in relaxed slabs of $CsPbX_3$ for both CsX and $PbX_2$ terminations (see Figure A.3) with neutral halide vacancy on the top surface. For perovskite structure, the interlayer distance is half of the lattice parameter corresponding to 3.09, 2.94 and 2.82 Å for $CsPbI_3$, $CsPbBr_3$ and $CsPbCl_3$, respectively.

| | | $CsPbI_3$ | | $CsPbBr_3$ | | $CsPbCl_3$ | |
|---|---|---|---|---|---|---|---|
| | layer | width | inter | width | inter | width | inter |
| CsX termination | | | | | | | |
| (top) | CsX | 1.47 | | 1.02 | | 0.85 | |
| | | | 2.64 | | 2.47 | | 2.39 |
| | $PbX_2$ | 2.82 | | 2.21 | | 2.01 | |
| | | | 3.15 | | 3.14 | | 3.04 |
| | CsX | 0.66 | | 0.66 | | 0.55 | |
| | | | 2.96 | | 2.82 | | 2.72 |
| | $PbX_2$ | 2.46 | | 1.34 | | 1.11 | |
| | | | 3.12 | | 2.91 | | 2.83 |
| | CsX | 1.05 | | 0.29 | | 0.36 | |
| | | | 3.01 | | 2.91 | | 2.80 |
| (median) | $PbX_2$ | 2.10 | | 1.63 | | 1.28 | |
| $PbX_2$ termination | | | | | | | |
| (top) | $PbX_2$ | 1.73 | | 1.07 | | 0.62 | |
| | | | 2.62 | | 2.55 | | 2.46 |
| | CsX | 1.26 | | 0.95 | | 0.48 | |
| | | | 3.26 | | 3.0 | | 2.92 |
| | $PbX_2$ | 1.75 | | 1.70 | | 0.89 | |
| | | | 2.99 | | 2.84 | | 2.72 |
| | CsX | 1.14 | | 0.52 | | 0.36 | |
| | | | 3.07 | | 2.94 | | 2.85 |
| | $PbX_2$ | 1.92 | | 1.50 | | 1.03 | |
| | | | 3.08 | | 2.89 | | 2.80 |
| (median) | CsX | 0.89 | | 0.74 | | 0.08 | |

justify that the left out site does not bring any difference to the final conclusion.

The vacancy formation energy is computed for the different sites for the case of charge and neutral vacancy. $E_{vac}$, vacancy formation energy for neutral and charged vacancies are calculated using the formula described in equations 3.4 and 3.5. Site ① and site ② (④ and ⑤ for I) show roughly the same energy in each of the two situations, charged and neutral vacancies. Of all the sites, site ③ (⑥ for I) shows the lowest vacancy formation energy.

$PbX_2$ terminated surfaces are more likely to form neutral vacancies whereas charged

TABLE A.8: Vacancy formation energy (in eV) for charge and neutral vacancies calculated for different sites with CsX and PbX$_2$ terminated structures for CsPbX$_3$ X=Cl, Br, I compounds.

| X | Charge vacancy | Neutral Vacancy |
|---|---|---|
| CsX termination | | |
| Cl, V-CsCl-s1 | 3.81 | −3.87 |
| V-CsCl-s2 | 3.83 | −3.90 |
| V-CsCl-s3 | 3.64 | −4.31 |
| Br, V-CsBr-s1 | 3.75 | −3.56 |
| V-CsBr-s2 | 3.76 | −3.59 |
| V-CsBr-s3 | 3.52 | −3.96 |
| I, V-CsI-s4 | 3.71 | −3.54 |
| V-CsI-s5 | 3.49 | −3.01 |
| V-CsI-s6 | 3.44 | −3.50 |
| PbI$_2$ termination | | |
| Cl, V-PbCl$_2$-s1 | 3.16 | −3.80 |
| Br, V-PbBr$_2$-s1 | 3.01 | −3.27 |
| I, V-PbI$_2$-s1 | 2.85 | −2.96 |

vacancies are more probable to be formed on CsX terminated surface. Further the adsorption energy of different molecules are listed in the following tables.

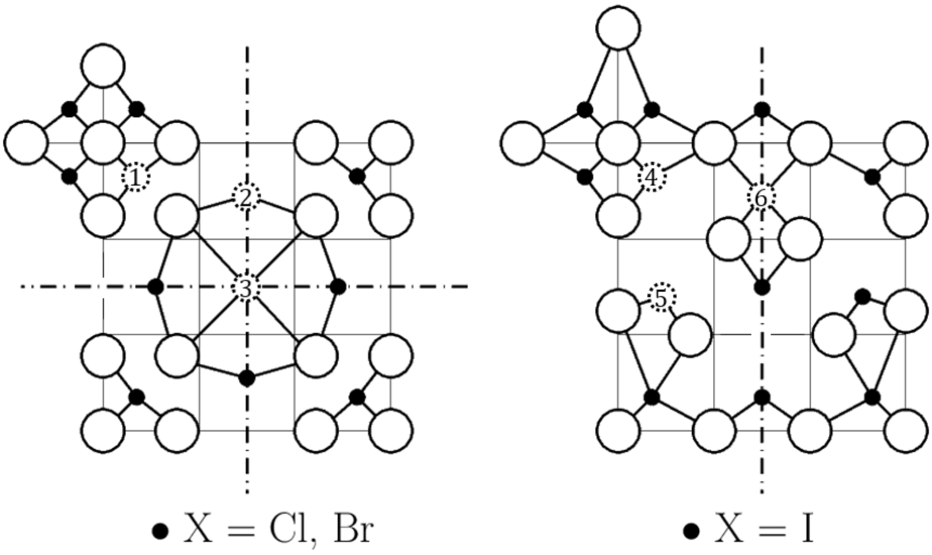

FIGURE A.4: Similar to Figure A.1, the numbering of sites shown for the reconstructed CsX surface with halide vacancies.

TABLE A.9: Relaxed interatomic distances (in Å) and adsorption energy (in eV) of $O_2$, calculated for different sites shown in Figure A.4. The data follow the conventions of the Figure 4.4

| | X | | Cs−O | O−$Pb_{-1}$ | O−$X_{-1}$ | Cs−Cs | $E_{\text{ads.}}$ |
|---|---|---|---|---|---|---|---|
| Charge Vacancy | Cl | V-CsCl-s1 | 3.64−3.84 | 3.49−4.08 | 3.75 | 5.85 | −0.09 |
| | | V-CsCl-s2 | 4.62−3.78 | 3.55−4.12 | 4.17 | 6.43 | −0.09 |
| | | V-CsCl-s3 | 4.23−4.51 | 4.30−4.87 | 5.34 | 5.57 | −0.06 |
| | Br | V-CsBr-s1 | 3.51−3.64 | 3.80−4.29 | 4.00 | 5.79 | −0.09 |
| | | V-CsBr-s2 | 3.74−4.01 | 3.77−4.07 | 3.69 | 6.49 | −0.10 |
| | | V-CsBr-s3 | 4.31−4.31 | 3.27−4.00 | 4.63 | 6.17 | −0.10 |
| | I | V-CsI-s4 | 3.49−3.56 | 3.38−3.97 | 3.71 | 7.52 | −0.21 |
| | | V-CsI-s5 | 4.34−5.19 | 3.68−4.26 | 3.92 | 7.25 | −0.17 |
| | | V-CsI-s6 | 3.41−3.52 | 3.63−3.96 | 3.48 | 7.38 | −0.19 |
| Neutral vacancy | Cl | V-CsCl-s1 | 3.18−3.20 | 2.42−3.21 | 3.56 | 5.29 | −2.19 |
| | | V-CsCl-s2 | 3.24−3.30 | 2.43−3.16 | 3.54 | 5.44 | −2.21 |
| | | V-CsCl-s3 | 3.24−3.31 | 2.43−2.44 | 3.54 | 5.44 | −2.53 |
| | Br | V-CsBr-s1 | 3.17 | 2.42−3.20 | 3.60 | 5.30 | −2.07 |
| | | V-CsBr-s2 | 3.16−3.26 | 2.42−3.18 | 3.57 | 5.67 | −2.09 |
| | | V-CsBr-s3 | 3.30−3.51 | 2.58−2.59 | 4.14 | 5.49 | −2.32 |
| | I | V-CsI-s4 | 3.09−3.10 | 2.47−3.23 | 4.44 | 5.41 | −2.08 |
| | | V-CsI-s5 | 3.09−3.14 | 2.44−3.25 | 3.68 | 5.39 | −2.14 |
| | | V-CsI-s6 | 3.09−3.14 | 2.44−3.24 | 3.68 | 5.39 | −2.43 |

TABLE A.10: Similar to Table -A.3 for adsorption of $CO_2$.

| | X | | Cs−O | C−$Pb_{-1}$ | O−$X_{-1}$ | Cs−Cs | $E_{\text{ads.}}$ |
|---|---|---|---|---|---|---|---|
| Charge vacancy | Cl | V-CsCl-s1 | 3.29−3.54 | 4.00 | 3.60 | 6.23 | −0.24 |
| | | V-CsCl-s2 | 3.28−3.60 | 4.02 | 3.39 | 6.48 | −0.24 |
| | | V-CsCl-s3 | 3.24−3.25 | 2.66 | 4.44 | 5.68 | −0.39 |
| | Br | V-CsBr-s1 | 3.28−3.44 | 4.30 | 3.63 | 6.78 | −0.27 |
| | | V-CsBr-s2 | 3.22 | 5.88 | 3.50 | 7.12 | −0.35 |
| | | V-CsBr-s3 | 3.10−3.16 | 4.31 | 3.87 | 8.07 | −0.38 |
| | I | V-CsI-s4 | 3.10−3.16 | 4.31 | 3.80 | 8.07 | −0.39 |
| | | V-CsI-s5 | 3.33−3.38 | 4.15 | 4.70 | 7.19 | −0.38 |
| | | V-CsI-s6 | 3.17−3.28 | 4.39 | 4.51 | 6.95 | −0.38 |
| Neutral Vacancy | Cl | V-CsCl-s1 | 3.15−3.31 | 2.65 | 3.80 | 5.29 | −0.95 |
| | | V-CsCl-s2 | 3.16−3.24 | 2.64 | 3.81 | 5.86 | −0.98 |
| | | V-CsCl-s3 | 3.12−3.4 | 2.70 | 3.77 | 5.88 | −0.88 |
| | Br | V-CsBr-s1 | 3.18−3.29 | 2.64 | 3.75 | 6.03 | −0.90 |
| | | V-CsBr-s2 | 3.18−3.26 | 2.64 | 3.74 | 6.00 | −0.89 |
| | | V-CsBr-s3 | 3.26−3.46 | 2.30 | 4.33 | 5.92 | −1.05 |
| | I | V-CsI-s4 | 3.36−3.37 | 3.77 | 3.70 | 7.23 | −0.43 |
| | | V-CsI-s5 | 3.24−3.39 | 2.64 | 4.05 | 5.65 | −0.90 |
| | | V-CsI-s6 | 3.18−3.76 | 3.32 | 3.71 | 7.15 | −0.55 |

TABLE A.11: Similar to Table -A.9 for adsorption of CO.

| | X | | Cs-C | Cs−O | C-Pb$_{-1}$ | O−Pb$_{-1}$ | O−X$_{-1}$ | Cs−Cs | $E_{\text{ads.}}$ |
|---|---|---|---|---|---|---|---|---|---|
| Charge vacancy | Cl | , V-CsCl-s1 | 3.50 | 3.71 | 3.84 | 3.78 | 3.25 | 6.35 | −0.21 |
| | | V-CsCl-s2 | 4.62 | 3.58 | 5.59 | 4.98 | 4.66 | 5.48 | −0.21 |
| | | V-CsCl-s3 | 4.56 | 3.69 | 3.34 | 3.95 | 3.58 | 6.88 | −0.25 |
| | Br | V-CsBr-s1 | 4.09 | 3.64 | 2.84 | 3.95 | 3.74 | 5.77 | −0.34 |
| | | V-CsBr-s2 | 4.25 | 3.59 | 2.84 | 3.96 | 3.77 | 5.72 | −0.30 |
| | | V-CsBr-s3 | 4.63 | 3.45 | 2.93 | 4.07 | 3.91 | 6.30 | −0.36 |
| | I | V-CsI-s4 | 4.62 | 3.36 | 2.92 | 4.07 | 3.91 | 7.69 | −0.35 |
| | | V-CsI-s5 | 4.89 | 5.03 | 2.77 | 3.92 | 3.98 | 7.15 | −0.33 |
| | | V-CsI-s6 | 4.40 | 3.36 | 2.95 | 4.07 | 3.97 | 7.68 | −0.33 |
| Neutral Vacancy | Cl | V-CsCl-s1 | 3.35 | 3.27 | 2.67 | 3.38 | 3.95 | 5.62 | −0.69 |
| | | V-CsCl-s2 | 3.35 | 3.33 | 2.67 | 3.38 | 4.02 | 5.83 | −0.66 |
| | | V-CsCl-s3 | 3.92 | 3.61 | 4.92 | 3.87 | 3.50 | 5.71 | −0.68 |
| | Br | V-CsBr-s1 | 4.10 | 3.28 | 2.65 | 3.40 | 3.72 | 5.34 | −0.65 |
| | | V-CsBr-s2 | 4.63 | 3.31 | 2.66 | 3.40 | 3.72 | 5.36 | −0.68 |
| | | V-CsBr-s3 | 3.57 | 3.49 | 2.44 | 3.61 | 4.19 | 5.68 | −0.65 |
| | I | V-CsI-s4 | 3.58 | 3.18 | 2.76 | 3.43 | 4.04 | 7.03 | −0.85 |
| | | V-CsI-s5 | 4.74 | 3.18 | 2.71 | 3.44 | 3.95 | 6.12 | −0.61 |
| | | V-CsI-s6 | 3.41 | 3.24 | 2.73 | 3.38 | 4.23 | 6.04 | −0.63 |

TABLE A.12: Similar to Table -A.9 for adsorption of $H_2O$.

| | | X | Cs−O | O−Pb$_{-1}$ | O−X$_{-1}$ | Cs−Cs | $E_{\text{ads.}}$ |
|---|---|---|---|---|---|---|---|
| Charge Vacancy | Cl | V-CsCl-s1 | 3.19−3.55 | 3.01 | 3.07 | 5.86 | −0.59 |
| | | V-CsCl-s2 | 3.50−4.25 | 2.78 | 3.69 | 5.43 | −0.59 |
| | | V-CsCl-s3 | 3.22−3.54 | 5.69 | 4.42 | 6.05 | −0.77 |
| | Br | V-CsBr-s1 | 3.41−4.46 | 2.83 | 3.78 | 5.44 | −0.58 |
| | | V-CsBr-s2 | 3.33−4.69 | 2.83 | 3.90 | 6.09 | −0.63 |
| | | V-CsBr-s3 | 3.45−4.45 | 2.70 | 3.72 | 5.82 | −0.80 |
| | I | V-CsI-s4 | 3.26−5.14 | 2.95 | 3.80 | 6.70 | −0.72 |
| | | V-CsI-s5 | 3.23−4.83 | 2.74 | 3.49 | 7.21 | −0.93 |
| | | V-CsI-s6 | 3.30−4.90 | 2.91 | 4.06 | 6.82 | −0.61 |
| Neutral Vacancy | Cl | V-CsCl-s1 | 3.24−4.63 | 3.58 | 4.41 | 5.36 | −0.77 |
| | | V-CsCl-s2 | 3.27−4.66 | 3.58 | 4.35 | 5.66 | −0.77 |
| | | V-CsCl-s3 | 3.33−3.44 | 3.73 | 3.96 | 6.02 | −0.94 |
| | Br | V-CsBr-s1 | 3.26−3.36 | 3.66 | 3.92 | 5.27 | −0.87 |
| | | V-CsBr-s2 | 3.25−3.35 | 3.66 | 3.92 | 5.28 | −0.87 |
| | | V-CsBr-s3 | 3.45−4.46 | 2.70 | 3.72 | 7.01 | −0.89 |
| | I | V-CsI-s4 | 3.07−4.60 | 3.77 | 4.06 | 7.37 | −1.28 |
| | | V-CsI-s5 | 3.19−3.62 | 3.63 | 3.49 | 6.60 | −1.02 |
| | | V-CsI-s6 | 3.63−3.64 | 3.46 | 4.09 | 5.44 | −1.28 |

# Résumé en français

## Introduction

Les pérovskites organiques/inorganiques halogénées gagnent en popularité dans le domaine du photovoltaïque (PV) en raison de leurs excellentes propriétés optoélectroniques telles qu'un band-gap optimal d'environ 1.7 eV [Tanaka et al., 2003], une bonne absorption solaire [Du et al., 2016], une longue durée de vie des porteurs [Stranks et al., 2013] et une bonne tolérance aux défauts [Brandt et al., 2015]. D'autres avantages non négligeables de ces matériaux sont leur faible coût de production et la possibilité de les synthétiser par des méthodes de chimie douce. Les cellules solaires à base de pérovskite ont été réalisées pour la première fois par Tsutomu Miyasaka en 2009 avec une efficacité de cette cellule d'environ 2.5% [Kojima et al., 2009]. Avec des techniques de traitement améliorées [Kajal et al., 2018], l'efficacité de conversion de puissance a atteint 25.2% [NRE] en 2020. Cette augmentation d'efficacité dans un court laps de temps a suscité l'intérêt de nombreux chercheurs. Cependant, le principal problème de ces matériaux est leur manque de stabilité à long terme caractérisée par une diminution dans leurs performances avec la température, en présence d'eau et sous UV. Celle-ci reste le frein à leur commercialisation à grande échelle. Beaucoup d'efforts ont été faits pour comprendre ce problème [Leguy et al., 2015; Juarez-Perez et al., 2016]. Il y a encore peu d'études théoriques ab initio sur l'impact de l'air et de l'eau sur les propriétés de ces matériaux. Ce travail porte donc sur l'étude ab initio de la dégradation des pérovskites organiques de type MAPI et inorganiques de type $CsPbX_3$ (avec X = Cl, Br et I) en présence de CO, $CO_2$, $O_2$ et $H_2O$.

TABLE $i$: Evolution en température (en K) des phases de différentes pérovskites organiques et inorganiques.

| Compound | hexagonal | orthorhombic | tetragonal | cubic |
|---|---|---|---|---|
| halide perovskites | | | | |
| $CsPbI_3$ | | $< 588^a$ | | $> 533^a$ |
| $CsPbBr_3$ | | $< 361^b$ | $361-403^b$ | $> 403^b$ |
| $CsPbCl_3$ | | | | $> 320^b$ |
| $MAPbI_3$ | | $< 162.2^c$ | $162.2-327.4^c$ | $> 327.4^c$ |
| $FAPbI_3$ | $< 438^d$ | $140-285^d$ | $> 285^d$ | |

[a] [Stoumpos et al., 2013a]; [b] [Stoumpos et al., 2013b]; [c] [Whitfield et al., 2016]; [d] [Ma et al., 2017]; [e]. [Scott et al., 2008]; [e]. [Wang and Gupta, 1973];

## Structure des pérovskites halogénées organiques et inorganiques

Les pérovskites ont une formule générique $ABX_3$ où X est un halogène (ici X = Cl, Br et I), et, A et B sont des cations. Les espèces A peuvent être organiques comme le méthylammonium (MA), $MA+=CH_3NH_3{}^+$, ou le formamidinium, $FA+ = CH(NH_2)_2{}^+$, mais aussi inorganiques comme $Cs^+$, $Rb^+$ ; tandis que B est un cation divalent comme $Pb^{2+}$ ou $Sn^{2+}$. L'ion B est entouré d'anions X formant les unités octaédriques de base $PbX_6$ de la pérovskite. Le cation organique/inorganique A est situé au centre de la cage formée par les unités $PbX_6$. Le prototype bien connu de ces matériaux est une de structure de phase cubique $Pm\bar{3}m$ ; cependant cette famille de composés possède une riche séquence de transitions de phase en pression et en température menant à des phases de symétrie inférieure à la phase cubique telles que tétragonale ou orthorhombique. Différentes phases des pérovskites étudiées sont données dans le tableau $i$. La phase cubique est la plus adaptée aux applications photovoltaïques en raison de sa bande interdite et de ses propriétés optiques [Quarti et al., 2016]. Dans ce travail, la structure considérée pour les pérovskites est cubique pour $CsPbX_3$ et pseudo-cubique pour MAPI et FAPI [Weller et al., 2015].

# Les approches ab initio et les fonctionnelles hybrides

Les modélisations ab initio réalisées dans ce travail sont basées sur les fonctionnelles hybrides. Celles-ci combinent un certain pourcentage de l'échange Hartree-Fock (HF) avec une fonctionnelle d'échange-corrélation développée dans le cadre de la Théorie de la Fonctionnelle de la Densité (DFT) afin d'obtenir une description qualitative et quantitative des propriétés structurales, électroniques et dynamiques d'une famille de matériaux. Dans ce travail, 16% et 20% d'échange HF ont été combinés aux fonctionnelles d'échange-corrélation de du type dit Perdew–Burke–Ernzerhof (PBE) afin d'obtenir des propriétés électroniques (comme le band gap) ou structurales en bon accord avec l'expérience des CsPbX$_3$, et, MAPI et FAPI, respectivement, comme l'illustre le tableau $ii$.

TABLE $ii$: Paramètres de réseau (a en Å) et band gap (Eg en eV) des CsPbX$_3$, MAPI et FAPI déterminés avec les fonctionnelles hybrides utilisées dans ce travail

| Compound | $a$ | | $E_g$ | |
|---|---|---|---|---|
| | Calc. | Exp. | Calc. | Exp. |
| CsPbI$_3$ | 6.196 | $6.198^a$, $6.289^b$, $6.177^c$, $6.189^d$ | 1.61 | $1.73^{c,d}$, $1.76^e$ |
| CsPbBr$_3$ | 5.884 | $5.883^a$, $5.870^b$, $5.874^{e,f}$ | 2.20 | $2.30^g$ |
| CsPbCl$_3$ | 5.659 | $5.660^a$, $5.605^e$ | 2.91 | $2.86^g$ |
| MAPbI$_3$ | 6.363 | $6.330^h$ | 1.62 | $1.60^i$ |
| FAPbI$_3$ | 6.428 | $6.362^j$ | 2.04 | $1.48^k$ |

[a] Moreira and Dias [2007]; [b] Stoumpos et al. [2013a] ; [c] Eperon et al. [2015]; [d] Swarnkar et al. [2016]; [d] Møller [1958]; [e] Lai et al. [2017] (nanowires); [f] Natarajan and Prakash [1971]. [g] Liu et al. [2013]. [h] Poglitsch and Weber [1987]. [i] Noh et al. [2013]. [j] Leblanc et al. [2019]. [k] Eperon et al. [2014].

# Propriétés vibrationnelles des cristaux

Les calculs de phonons ont été réalisés afin de comprendre la dynamique de réseau qui pourrait influencer les propriétés des surfaces. Ils révèlent que la structure cubique des pérovskites possède des instabilités au centre (MAPI ou FAPI) et en bordure de zone Brillouin de (CsPbX$_3$) caractérisées par l'existence de modes instables (fréquences imaginaires). L'analyse des vecteurs propres montre que, pour CsPb$X_3$, celles-ci sont liées à la rotation des octaèdres $PbX_6$ conduisant aux transitions de phase tétragonale et orthorhombique ; tandis que pour les MAPI et FAPI, ces instabilités combinent la rotation des octaèdres avec une réorientation ou réorganisation des molécules organiques MA et FA les unes par rapport aux autres menant à une phase orthorhombique de plus basse énergie. En effet, les molécules organiques possèdent des moments dipolaires qui, par interaction électrostatique, influencent l'orientation des autres entités voisines et donc les propriétés électroniques de ces matériaux [Carignano et al., 2016; Maheshwari et al., 2019].

## Propriétés des surfaces (001) des pérovskites

Pour étudier l'adsorption des molécules, les surfaces (001) des $CsPbX_3$ et MAPX, et (100), (010) et (001) des FAPX ont été considérées. Un modèle 2D de type couches minces a été utilisé afin de modéliser leurs propriétés. Chacune des surfaces possède deux types de terminaison : (Cs/FA/MA)X et $PbX_2$. Leur épaisseur a été optimisée afin d'obtenir une stabilisation en fonction de cette épaisseur de certaines propriétés comme l'énergie de formation des surfaces, les distances interatomiques au centre de la surfaces qui doivent correspondre à celles des cristaux, ou encore les données vibrationnelles. Cependant, pour les MAPI et FAPI, à cause de la réorganisation des molécules organiques entre elles, cette tâche n'est pas aisée : par exemple, pour les surfaces (010) et (001) de FAPI, les entités organiques se trouvent sur un plan de symétrie ce qui interdit toute rotation ; par contre, ce n'est pas le cas pour la surface (100) ce qui engendre une réorganisation des molécules à grande échelle au travers de la surface (la convergence n'est pas atteinte pour des systèmes qui font plusieurs nanomètres). Les propriétés vibrationnelles de ces surfaces ont été étudiées. Elles possèdent les mêmes caractéristiques que celles des cristaux : les surfaces à base $CsPbX_3$ possèdent toujours des fréquences imaginaires en bordure de zone de Brillouin décrivant les rotations des octaèdres des halogènes, et , celles à base de MAPI et FAPI les mêmes instabilités liées à la combinaison des rotations des octaèdres et la réorganisation des entités moléculaires les unes par rapport aux autres.

## Adsorption du $CO_2$, CO, $O_2$ et $H_2O$ sur les différentes pérovskites

Afin d'étudier l'adsorption des molécules, les supercellules suffisamment grandes one été utilisées pour exclure, ou au moins minimiser, l'interactions entre les répliques des molécules translatées pas entre eux. La principale difficulté de ce type de simulation réside dans l'existence des transitions de phase qui peuvent engendrer des relaxations atomiques liées aux modes instables et non pas à la présence de l'adsorbat. Ainsi pour chaque supercellule, les modes instables ont été déterminés ; ensuite, seules les modes de plus basses symétries ont été considérés afin d'optimiser les structures atomiques de chaque supercellule avec un maximum de degrés de liberté. Les surfaces obtenues, dites reconstruites, ont été choisies pour modéliser les différentes adsorptions (voir Fig. $i$)

Pour les pérovskites inorganiques, deux types de surface ont été considérés sans et avec défaut. Le défaut considéré est un centre F soit une lacune anionique, le plus stable et plus probable à la surface de ces matériaux [Eames et al., 2015]. A cause des différents transferts de charges liés soit à l'illumination ou aux réactions chimiques aux interfaces, ces défauts peuvent être neutres ou chargés. Ceux-ci ont été considérés afin d'évaluer leurs effets sur l'adsorption des molécules. Pour la MAPI et FAPI, uniquement les surfaces sans défaut ont été considérées pour évaluer l'impact des entités moléculaires sur la réactivité des surfaces. Pour chaque surface et chaque terminaison de chaque composé, les CO, $CO_2$, $O_2$ et $H_2O$ ont été adsorbés sur différents sites du sommet des couches. Pour les différentes réactions, les énergies d'adsorption ont été systématiquement déterminées et interprétés en termes de structures atomiques et électroniques, et, de répartition de charge de Mulliken des molécules adsorbées sur les différents substrats. Quelque soit la pérovskite, CO et $CO_2$ physisorbent sur les différentes surfaces tandis que $H_2O$ et $O_2$ peuvent se chimisorber sur les pérovskites organiques : $H_2O$ peut se dissocier sur les pérovskites inorganiques, ou, peut former, ainsi que $O_2$, des oxydes avec les molécules organiques des MAPI. Pour les pérovskites inorganiques, excepté pour $H_2O$,– CO, $CO_2$ et $O_2$ physisorbent sur les

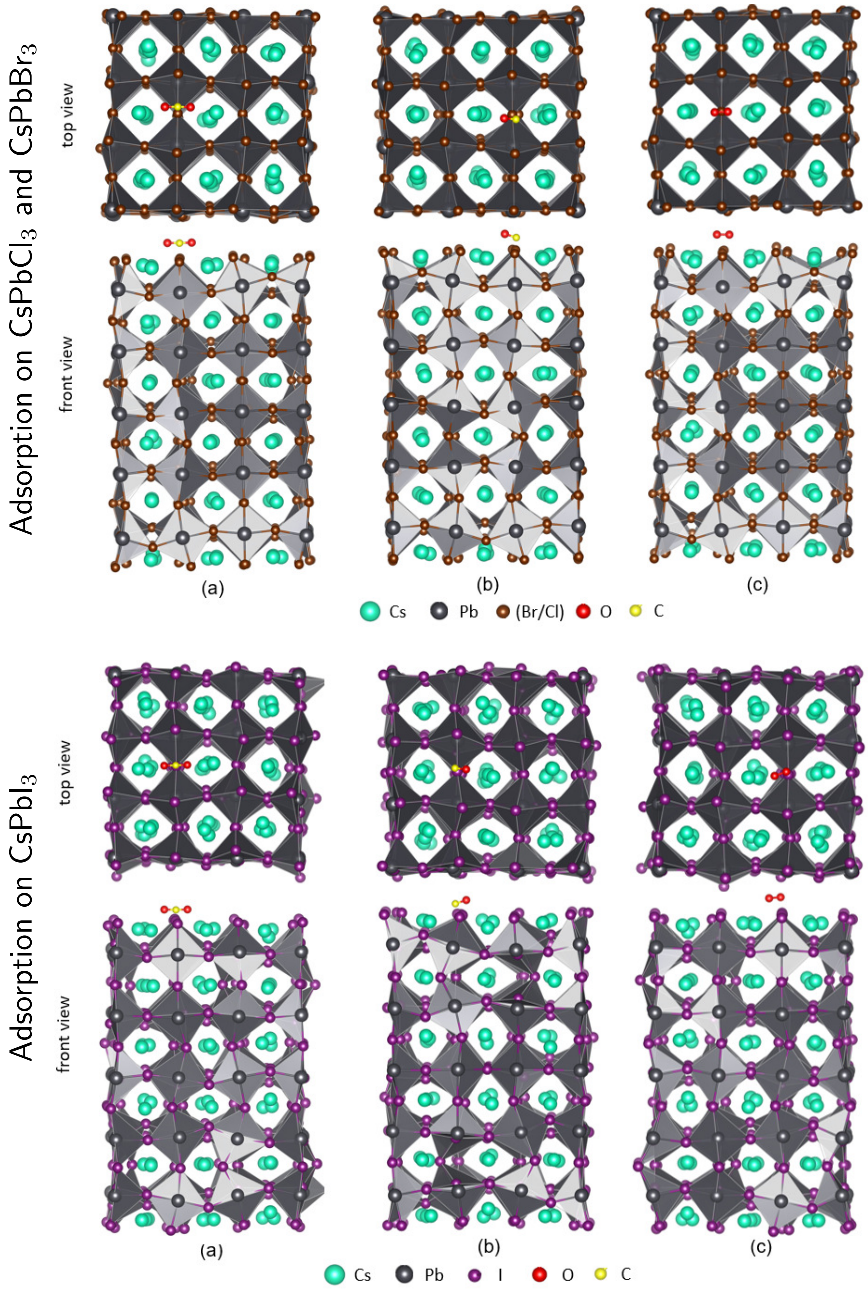

FIGURE *i*: $CO_2$ (a), CO (b) et $O_2$ (c) adsorbés sur les surfaces (001) terminées par CsX des $CsPbX_3$ (X = Cl, Br et I).

surfaces. Par contre, la présence de centre F (chargé ou neutre) catalyse les réactions de ces molécules avec ces surfaces : $CO_2$, $O_2$ et $H_2O$ chimisorbent sur ces surfaces ; notamment, $O_2$ peut former des superoxydes et $H_2O$ peut se dissocier sur ces surfaces. Ces réactions sont notamment caractérisées par un accroissement drastique des énergies d'adsorption (voir Tableau *iii*).

TABLE *iii*: Energies d'adsorption des $CO_2$, CO et $O_2$ sur les surfaces (001) des $CsPbX_3$ (X = Cl, Br et I) sans ou avec une lacune d'halogène (centre-F).

| | Perovskite | molecule | Perfect surface | Surface with Vacancy | |
|---|---|---|---|---|---|
| | | | | Charge | Neutral |
| CsX termination | $CsPbCl_3$ | $CO_2$ | −0.36 | −0.39 | −0.98 |
| | | CO | −0.28 | −0.25 | −0.69 |
| | | $O_2$ | −0.10 | −0.09 | −2.53 |
| | $CsPbBr_3$ | $CO_2$ | −0.40 | −0.68 | −0.90 |
| | | CO | −0.29 | −0.81 | −0.68 |
| | | $O_2$ | −0.11 | −0.10 | −2.32 |
| | $CsPbI_3$ | $CO_2$ | −0.54 | −0.39 | −0.90 |
| | | CO | −0.35 | −0.35 | −0.85 |
| | | $O_2$ | −0.20 | −0.21 | −2.43 |
| $PbX_2$ termination | $CsPbCl_3$ | $CO_2$ | −0.18 | −0.24 | −0.68 |
| | | CO | −0.12 | −0.21 | −0.51 |
| | | $O_2$ | −0.03 | −0.11 | −2.16 |
| | $CsPbBr_3$ | $CO_2$ | −0.15 | −0.27 | −0.46 |
| | | CO | −0.17 | −0.34 | −0.62 |
| | | $O_2$ | −0.05 | −0.12 | −1.96 |
| | $CsPbI_3$ | $CO_2$ | −0.11 | −0.38 | −0.51 |
| | | CO | −0.16 | −0.35 | −0.40 |
| | | $O_2$ | −0.02 | −0.17 | −2.55 |

Concernant l'adsorption de l'eau et de l'oxygène sur les surfaces (001) de la MAPI, deux phases ont été considérés : une phase de physisorption, pour laquelle les molécules ne sont pas dissociées, et une phase de chimisorption (voir Fig. *ii*), pour laquelle les

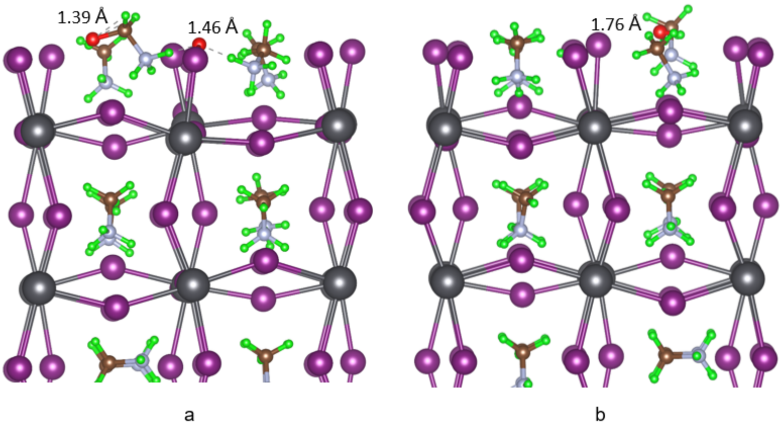

FIGURE *ii*: Final configurations de $O_2$ (a) dissocié et $H_2O$ (b) sur la surface MAPI (001) avec terminaison (MA)I.

molécules ont été dissociées pour former différentes formes d'oxydes. Pour la physisorption, l'eau possède une plus grande énergie d'adsorption que l'oxygène notamment sur les surfaces avec la terminaison en $PbI_2$. Par contre pour la chimisorption, $O_2$ peuvent former différents types d'oxydes ou hydroxydes avec les entités organiques avec des énergies réactions très favorables d'à peu près 2 eV.

## Conclusions

Dans cette thèse, une étude théorique systématique de l'adsorption du $CO_2$, CO, $O_2$ et $H_2O$ sur les surfaces complexes de pérovskites organiques et inorganiques a été réalisée au niveau ab initio afin de comprendre les mécanismes précurseurs de la dégradation des performances de ces pérovskites dans le cadre de leurs applications pour le photovoltaïque. Les principales pérovskites considérées dans cette thèse ont été : les $CsPbX_3$ (X = Cl, Br et I) et la $CH_3NH_3PbI_3$. Les calculs ab initio réalisés dans cette thèse utilisent des fonctionnelles hybrides spécialement optimisées pour reproduire quantitativement et qualitativement les propriétés structurales, électroniques et dynamiques de ces pérovskites. Elles combinent un certain pourcentage d'échange Hartree-Fock avec les fonctionnelles d'échange-corrélation PBE et PBEsol développées dans le cadre de la théorie de la fonctionnelle de la densité (DFT). L'étude de l'adsorption des molécules sur les différents substrats combinent une représentation 2D de type couches minces des surfaces et une approche supercellule. Les pérovskites étudiées dans ce travail possèdent une riche séquence de transitions de phase liée à l'existence de modes vibrationnels instables qui peut influencer la structure des surfaces. Ainsi, les propriétés vibrationnelles des surfaces ont été étudiées afin de déterminer qu'elles sont les relaxations atomiques associées aux transitions de phase afin de ne pas intégrer leur contribution dans les perturbations induites par l'adsorption des molécules. Pour les pérovskites inorganiques, deux types de surface ont été considérés : sans et avec la présence de centre F, c'est-à-dire, en présence de lacunes d'halogènes chargées ou neutres. Pour les surfaces sans défaut, quelque soit le matériau, $CO_2$, CO et $O_2$ physisorbent sur les surfaces. Par contre, la présence de défaut accroit la réactivité de ces molécules avec ces surfaces : leurs énergies d'adsorption s'accroissent drastiquement ; pour les défauts neutres, l'oxygène, peut notamment former des superoxydes. Le cas de l'eau a aussi été étudié : c'est l'espèce la plus réactive qui peut notamment se dissocier sur ces surfaces. $CO_2$ et CO physisorbent sur les surfaces à base de MAPI. Par contre, les entités moléculaires MA sont très réactives avec l'oxygène et l'eau : les énergies d'adsorption sont de plusieurs eV, ces deux molécules peuvent former des oxydes et hydroxydes complexes à la surface de ce matériau quelque soit la terminaison de la surface.

Pratiquement de cette considération, les molécules (CO, $CO_2$ et $O_2$) ne sont susceptibles d'apporter aucun effet dommageable à la surface des pérovskites ($CsPbX_3$). Cependant, pour la surface avec une lacune neutre, $O_2$ et $CO_2$ sont plus susceptibles d'attaquer. Dans le cas de MAPI, $H_2O$ et $O_2$ ont une plus grande affinité pour attaquer à l'état dissocié qu'à l'état non dissocié. Les études ultérieures doivent se tourner vers l'exploration de l'action combinée des molécules et de la température.

# Scientific Communications

## Poster Presentation

- First-principles investigation of the adsorption of carbon dioxide, carbon monooxide and oxygen on $CsPbX_3$ (X= Cl, Br, I) surfaces.

  A. Mishra, Ph. Baranek and A. Postnikov

  MSS-2018 Ab-initio modelling in solid state chemistry held in Imperial college at London, UK.

- First-principles investigation of $CO_2$, CO and $O_2$ adsorption on perfect and defective $CsPbX_3$ (X= Cl, Br, I) surfaces.

  A. Mishra, Ph. Baranek and A. Postnikov

  i) 2nd international conference on interface properties in organic and hybrid electronics (IPOE-2019) held in Cergy, France.

  ii) Data science summer school (DS3-2019), held in Ecole Polytechnique, Palaiseau, France.

- First-principles investigation of the adsorption of carbon dioxide, carbon monoxide and oxygen on $CsPbX_3$ (X= Cl, Br, I) surfaces.

  A. Mishra, Ph. Baranek and A. Postnikov

  5th international conference on perovskite solar cells and optoelectronics (PsCO2019) held in EPFL, Lausanne, Switzerland.

## Oral Presentation

- First-principles investigation of the adsorption of carbon dioxide, carbon monoxide and oxygen on CsPbX3 (X= Cl, Br, I) surfaces.

  A. Mishra, Ph. Baranek and A. Postnikov

  nanoGE-2019 fall meeting, Symposium: Halide perovskites: when theory meets experiment from fundamentals to devices, held in Berlin Germany.

## Publications

- First-principles investigation of $CO_2$, CO, and $O_2$ adsorptions on the (001)-reconstructed surfaces of $CsPbX_3$ (X = Cl, Br, and I) perovskites.

  A. Mishra, Ph. Baranek and A. Postnikov

  *Surfaces and Interfaces Volume 25, August 2021, 101264*

  https://doi.org/10.1016/j.surfin.2021.101264

- Detrimental effects of ion migration in the perovskite and hole transport layers on the efficiency of inverted perovskite solar cells.

  Y. Huang, P. Lopez-Varo, B. Geffroy, H. Lee, J.E. Bourée, A. Mishra, Ph. Baranek, A. Rolland, L. Pedesseau, J.M. Jancu, J. Even, J.B. Puel, M. Gueunier-Farret

  *J. of Photonics for Energy, 10(2), 024502 (2020)*

  https://doi.org/10.1117/1.JPE.10.024502